

Optical and Radio Variability of the Blazar S4 0954+658

V.V. Vlasyuk,^{1*} Yu.V. Sotnikova,^{1,2} A.E. Volvach,³ O.I. Spiridonova,¹ V.A. Stolyarov,^{1,4}
 A.G. Mikhailov,¹ Yu.A. Kovalev,⁵ Y.Y. Kovalev,^{6,5,7} M.L. Khabibullina,¹ M.A. Kharinov,⁸
 L. Yang,⁹ M.G. Mingaliev,^{1,2,8} T.A. Semenova,¹ P.G. Zhekanis,¹ T.V. Mufakharov,^{1,2}
 R.Yu. Udovitskiy,¹ A.A. Kudryashova,¹ L.N. Volvach,³ A.K. Erkenov,¹ A.S. Moskvitin,¹
 E.V. Emelianov,¹ T.A. Fatkhullin,¹ P.G. Tsybulev,¹ N.A. Nizhelsky,¹ G.V. Zhekanis,¹ E. V. Kravchenko^{7,5}

¹ *Special Astrophysical Observatory of RAS, Nizhny Arkhyz, 369167, Russia*

² *Kazan (Volga Region) Federal University, Kazan 420008, Russia*

³ *Crimean Astrophysical Observatory, Russian Academy of Sciences, Nauchny, 298409, Russia*

⁴ *Astrophysics Group, Cavendish Laboratory, University of Cambridge, Cambridge, CB3 0HE, UK*

⁵ *Astro Space Center, Lebedev Physical Institute, Russian Academy of Sciences, Moscow, 117997, Russia*

⁶ *Max-Planck-Institut für Radioastronomie, Auf dem Hügel 69, Bonn, 53121, Germany*

⁷ *Moscow Institute of Physics and Technology, Institutsky per. 9, Dolgoprudny, 141700, Russia*

⁸ *Institute of Applied Astronomy, Russian Academy of Sciences, Kutuzova Embankment 10, St. Petersburg, 191187, Russia*

⁹ *Department of Physics and Astronomy, Sun Yat-sen University, No 2 Daxue Road, Zhuhai, 519082, China*

Accepted 9 October 2023. Received 8 August 2023

Published in Astrophysical Bulletin Vol.78, N4 (2023)

ABSTRACT

We present an optical-to-radio study of the BL Lac object S4 0954+658 observations during 1998–2023. The measurements were obtained with the SAO RAS Zeiss-1000 1-m and AS-500/2 0.5-m telescopes in 2003–2023, with the RATAN-600 radio telescope at 1.25 (0.96, 1.1), 2.3, 4.7 (3.7, 3.9), 8.2 (7.7), 11.2, 22.3 (21.7) GHz in 1998–2023, with the IAA RAS RT-32 Zelenchukskaya and Badary telescopes at 5.05 and 8.63 GHz in 2020–2023, and with the RT-22 single-dish telescope of CrAO RAS at 36.8 GHz in 2009–2023. In this period the blazar had been showing extremely high broadband activity with the variability amplitude of flux densities up to 70–100% both in the optical and radio domains. In the period of 2014–2023 the blazar had been showing the historically highest activity in the radio wavelengths, and we detected multiple radio flares of varying amplitude and duration. The large flares last on average from 0.3 to 1 year at 22–36.8 GHz and slightly longer at 5–11.2 GHz. The optical flares are shorter and last 7–50 days. In the most active epoch of 2018–2023 the characteristic time scale τ of variation at 5–22 GHz is about 100 days and about 1000 days for the state with lower activity in 2009–2014. We found a general correlation between the optical, radio, and γ -ray flux variations, which suggests that we observe the same photon population from different emission regions. We estimated linear size of this region as 0.5–2 pc for different epochs. A broadband two components radio spectrum of S4 0954+658 jet was modelled by using both electrons and protons as emitting particles. It is shown that the synchrotron radio waves in this AGN may be generated by relativistic protons.

Key words: galaxies: active – galaxies: BL Lacertae objects – quasars: general – radio continuum: galaxies

1 INTRODUCTION

Blazars are a specific type of active galactic nuclei (AGNs) known for emitting relativistic jets that align with the observer’s line of sight (Urry & Padovani 1995). Blazars encompass two categories: BL Lacertae objects (BL Lacs) and flat spectrum radio quasars (FSRQs). When their optical/UV spectra are examined, BL Lacs display a continuous, featureless emission or weak narrow emission lines with an equivalent width (EW) of $\leq 5\text{\AA}$ (e.g., (Stickel et al. 1991; Marcha et al. 1996)), while FSRQs exhibit prominent broad emission

lines. The flux, polarization, and spectra of blazars are highly variable across the electromagnetic spectrum from radio to γ -rays (e.g., (Gupta et al. 2017) and references therein). Blazars demonstrate variability on different timescales, ranging from minutes to several decades (Miller et al. 1989; Gopal-Krishna et al. 1993; Wagner & Witzel 1995; Gupta et al. 2004).

The emission of blazars, spanning the entire electromagnetic spectrum, is primarily dominated by nonthermal radiation originating from their relativistic jets. This broad-spectrum emission offers a valuable opportunity for investigating their spectral energy distribution (SED), which is commonly characterized by a distinctive double-hump structure (von Montigny et al. 1995; Fossati et al. 1998). In

* E-mail: vvlas@sao.ru

the frequency range from radio to soft X-rays, synchrotron emission serves as the dominant mechanism, while at higher energies such as hard X-rays and γ -rays, inverse Compton (IC) scattering is believed to be the primary process (Ulrich et al. 1997; Böttcher 2007). A classification system based on the peak synchrotron frequency ν_{peak} has categorized blazars into three subclasses: LSP, low synchrotron peaks with $\nu_{\text{peak}} \leq 10^{14}$ Hz; ISP, intermediate synchrotron peaks with 10^{14} Hz $< \nu_{\text{peak}} < 10^{15}$ Hz; and HSP, high synchrotron peaks with $\nu_{\text{peak}} \geq 10^{15}$ Hz (Abdo et al. 2010).

When compared to the other ranges of the electromagnetic spectrum, the optical band appears relatively narrow. Nonetheless, it plays a crucial role in providing valuable information about nonthermal synchrotron emission and potential thermal emission from accretion discs. Typically, on short-term and long-term variability timescales, distinct spectral trends are observed. BL Lacertae objects exhibit a bluer-when-brighter (BWB) trend (Massaro et al. 1998; Villata et al. 2002; Vagnetti et al. 2003; Gu & Ai 2011; Gaur et al. 2012), while flat spectrum radio quasars tend to show a redder-when-brighter (RWB) trend (Ramírez et al. 2004; Gu et al. 2006; Osterman Meyer et al. 2008, 2009). However, it is worth noting that in some cases opposite trends have also been detected in certain blazars (Gu et al. 2006; Gaur et al. 2012; Isler et al. 2017). Recent studies have extensively investigated the optical variability of blazars across various timescales, utilizing observations from both space-based and ground-based telescopes. The findings reveal that long-term variability is primarily characterized by significant flux changes, occasionally accompanied by sudden flares and quasi-periodic oscillations (Bhatta et al. 2023).

The variable fluxes of blazars in the optical band exhibit a log-normal distribution on long timescales (Bhatta 2021) and a normal distribution on shorter timescales with most of the flux histograms following bimodal distribution, as have been reported in (Pininti et al. 2023) based on numerous light curves of blazars from the TESS (Transiting Exoplanet Survey Satellite) survey.

In order to find a possible link between the emission of blazars in different spectral ranges, Liodakis et al. (2018) studied radio, optical, and γ -ray light curves of 145 bright blazars, spanning up to 8 yr, to probe the flaring activity and interband correlations. Of these, 26 objects showed a $> 3\sigma$ correlation for at least one wavelength pair, as measured by the discrete correlation function. As it has been proved, the most common and strongest correlations are found between the optical and γ -ray bands, with fluctuations simultaneous within 30-day data resolution. The radio response is usually substantially delayed with respect to the other wavelengths with median time lags of about 100–160 days.

The BL Lac-type blazar S4 0964+658 is one of the intriguing members of the blazar family, characterized by its unique emission properties and complex behavior which has sparked debates about its classification (Stickel et al. 1991; Hervet et al. 2016). It displays significant flux and polarization variability on both intraday and longer timescales (Hagen-Thorn et al. 2015; Morozova et al. 2016; Volvach et al. 2016; Liu et al. 2018). The time delay observed between flares in the optical and radio bands may find an explanation in the dynamic interplay of active processes originating from various regions in the central parts of the host galaxy. Moreover, the jet structure adds to the blazar enigmatic nature. Recent

studies (Morozova et al. 2014; Jorstad et al. 2017; Wang et al. 2023) have provided additional insights, including the identification of jet components exhibiting superluminal motion, further elucidating the geometry and behavior of this blazar. Despite the ongoing debate, S4 0954+658 continues to captivate researchers, offering a unique window into the complex and dynamic phenomena occurring in active galactic nuclei and blazars.

In this paper we present the quasi-simultaneous observations of the blazar S4 0954+658 in the R band from the 1-meter Zeiss-1000 and 0.5-meter AS-500/2 optical reflectors of the Special Astrophysical Observatory of the Russian Academy of Sciences (SAO RAS) together with the radio observations at 1–22 GHz from RATAN-600, at 5.05 and 8.63 GHz from the RT-32 (IAA RAS¹), and at 36.8 GHz from the RT-22 (CrAO RAS²). This collaboration’s primary objective was to achieve dense sampling to identify potential correlations between the emissions in the two different bands. Such a vast database for this specific source provides an opportunity to investigate emission characteristics on both long and short time scales.

The paper is structured as follows. In Section 2 the results from the previous studies of the blazar are given, in Section 3 we describe the radio catalogues which were used as additional radio data. The photometric study with the optical telescopes of SAO RAS are presented in Section 4. Section 5 describes the radio observations with the RATAN-600, RT-32, and RT-22 instruments. We discuss the broad-band radio spectra and variability characteristics in Section 6. The flare characteristics in the optical and radio domains are presented in Section 7. In Section 8 we compute the structure functions for chosen observing epochs. The correlations between different bands are discussed in Section 9. In Section 10 we summarize the results and draw final conclusions.

2 THE BLAZAR S4 0954+658

The object S4 0954+658 at $z = 0.368$ (Lawrence et al. 1986), also known as QSO B0954+65, was identified as a radio source during the Jodrell-Bank 996 MHz Survey, and its optical counterpart was found by Cohen et al. (1977). Walsh et al. (1984) classified S4 0954+658 as a BL Lac object from the analysis of its spectrum, showing a smooth continuum with no detectable emission or absorption features. However, its classification remains ambiguous to this day. This source shows a one-sided radio jet with a polarized hotspot, and the polarization of the inner part of the jet indicates a longitudinal magnetic field (Kollgaard et al. 1992). Ghisellini et al. (2011) assigned this entity to the category of LBLs (low energy peaked BL Lacs, same as LSPs) based on its SED. But Hervet et al. (2016) classified S4 0954+658 as a flat spectrum radio quasar (FSRQ) due to the kinematic features of its radio jet. Nevertheless, in the literature it is mostly classified as a BL Lac object because of the small equivalent width of its emission lines in the spectrum (Stickel et al. 1991).

S4 0954+658 has been extensively studied due to its intricate variability as a blazar. The object was also studied in the

¹ Institute of Applied Astronomy, Russian Academy of Sciences

² Crimean Astrophysical Observatory, Russian Academy of Sciences

X-ray band (Perlman et al. 2006; Resconi et al. 2009), and it was one of the first detected extragalactic γ -ray sources (Thompson et al. 1995; Acero et al. 2015).

According to the Very Large Array (VLA) images, a curved jet is observed, extending south on arcsec scales (Perley 1982; Kollgaard et al. 1992). Very Long Baseline Interferometry (VLBI) maps revealed a core and jet components with remarkably strong polarization ($\sim 11\%$) and unusually high superluminal motion ($\beta_{\text{app}}h = 7.4 \pm 0.7$ and 4.4 ± 0.7 for the K2 and K3 jet components respectively, (Gabuzda et al. 1992, 1994)), whose polarization is well aligned with the VLBI-structure axis, as is commonly seen in the BL Lacertae objects, indicating that the milliarcsecond jet is also curved (see Gabuzda & Cawthorne (1996) and references therein).

The multi-color photometric and polarization observations of S4 0954+658 carried out mainly in the Astronomical Institute of St. Petersburg State University and the Central Astronomical Observatory of the Russian Academy of Sciences in 2008–2012 were analyzed in Hagen-Thorn et al. (2015). The authors proved that there exist distinct individual variable components responsible for the activity; the power-law spectrum and high degree of polarization confirm that the emission is generated by synchrotron radiation. Modeling the observed dependencies between polarization and intensity were used to derive the parameters of both constant and variable components of the emission.

During an unprecedented bright optical flare in early 2015, a new bright polarized superluminal knot ejected from the VLBI core at 43 GHz during the peak of the flare was discovered by Morozova et al. (2016). This outburst was accompanied by very-high-energy (VHE > 150 GeV) and variable gamma-ray emission (Mirzoyan 2015; MAGIC Collaboration et al. 2018). A comprehensive analysis of observations from γ -rays to centimeter radio waves along with harmonic and structure analyses in Volvach et al. (2016) allowed the authors to derive the orbital ($T_{\text{orb}} \approx 870$ yrs) and precessional ($T_{\text{pr}} \approx 8700$ yrs) periods in the source rest frame for a model in which a binary super-massive black hole is present in this active galactic nucleus.

The blazar S4 0954+658 has a relatively small angular size the major and minor axes are 7.0×4.4 mas (Cassaro et al. 2002). Gabuzda et al. (2000) revealed a bent jet on both parsec and kiloparsec scales. Their study also unveiled significant intranight polarization variability (30–40%) of the radio core at 5 GHz. Furthermore, Kudryavtseva et al. (2010) made noteworthy observations of several moving components in the jet at 22 GHz with a mean velocity of $4.9 \pm 0.4 c$.

During an analysis of the VLBA 43 GHz data spanning from May 2017 to May 2021, Wang et al. (2023) successfully identified three prominent jet components. Among these, two components exhibited clear superluminal motion, while one remained stationary in close proximity to the core. The angles between the moving jet components and the line of sight were measured as 5.5° and 6.9° with corresponding opening angles of 1.8° and 2.4° . Notably, the trajectories of all jet components predominantly align along two distinct paths, corroborating the findings of a previous study conducted by Morozova et al. (2014).

Jorstad et al. (2017) estimated a curvature of the parsec-scale jet of this BL Lac object: about of 0.5 mas from the core, where the moving knots seem to decelerate.

Usually, the analysis of data acquired in different wave-

bands over a long time period encounters limitations of good data sampling (Raiteri et al. 1999), which is an exception for S4 0954+658 due to its violent behaviour and intensive observing programs.

In a recent study conducted in 2021, Becerra González et al. (2021) identified a MgII emission line in S4 0954+658 at $z = 0.3694 \pm 0.0011$ with an equivalent width close to 5\AA , which is often considered as the limit for classifying blazars as FSRQs. Therefore, it appears more reasonable to regard this γ -ray emitter as a transitional object.

3 LITERATURE DATA IN THE RADIO BAND

Additionally we used the radio data taken from the astrophysical CATalogs support System (CATS database,³ Verkhodanov et al. 2005, 2009) to construct the broadband radio spectrum over the historical period of blazar observations. The data cover a time period of up to 40 years at the most representative frequency of ~ 5 GHz, including the latest measurements presented in this paper.

The vast majority of the measurements is provided by several tens of radio catalogues that are summarized in Table 1, where we include the epochs, frequencies of observations, and corresponding literature references. The main data are represented by the NRAO VLA Sky Survey (NVSS, Condon et al. 1998), Faint Images of the Radio Sky at Twenty-cm Survey (FIRST, Becker et al. 1994), Westerbork Northern Sky Survey (WENSS, Rengelink et al. 1997), Green Bank 6-cm Survey (GB6, Gregory et al. 1996), Australia Telescope 20 GHz Survey (ATCA20, Murphy et al. 2010), Giant Metrewave Radio Telescope Sky Survey (TGSS) at 150 MHz (2015; Intema et al. 2017), VLA measurements (Healey et al. 2007), and others. The time period begins in 1974 with the Texas Survey of Radio Sources, covering $-35^\circ.5 < \delta < 71^\circ.5$ at 365 MHz (TXS, Douglas et al. 1996, Gregory et al. 1996). A significant contribution in the measurements was provided by the Multiyear Monitoring Program of Compact Radio Sources at 2.5 and 8.2 GHz (Lazio et al. 2001) and by the low-frequency GaLactic and Extragalactic All-sky Murchison Widefield Array (GLEAM) at 72–231 MHz (Hurley-Walker et al. 2017). The multi-frequency quasi-simultaneous observations with the RATAN-600 radio telescope are presented by the six-frequencies catalog from Mingaliev et al. (2017). The RATAN-600 measurements of the blazar are available in the electronic on-line catalog BLcat⁴ (Mingaliev et al. 2014; Sotnikova et al. 2022a).

4 PHOTOMETRIC STUDY OF THE SOURCE WITH THE SAO RAS OPTICAL TELESCOPES

4.1 Optical observations

The optical study (mainly in the R band with episodic use of the BVI bands) was provided using the 1-meter (2003–June 2023) and 0.5-meter (2021–June 2023) optical reflectors of the Special Astrophysical Observatory of RAS. Below we

³ <https://www.sao.ru/cats>

⁴ <https://www.sao.ru/blcat>

Table 1. The list of catalogues with the radio measurements. The references in the last column are: [1] — Aller et al. (1985), [2] — Pauliny-Toth et al. (1978), [3] — Douglas et al. (1996), [4] — Hales et al. (1990), [5] — Owen et al. (1978), [6] — Lazio et al. (2001), [7] — Seielstad et al. (1983); Richards et al. (2011), [8] — Ulvestad et al. (1981), [9] — Johnston et al. (1995), [10] — Perley (1982), [11] — Riley et al. (1999), [12] — Zhang et al. (1997), [13] — Gregory et al. (1996), [14] — Gregory & Condon (1991), [15] — Becker et al. (1991), [16] — Reuter et al. (1997), Steppe et al. (1993), [17] — Teraesranta et al. (1998), [18] — Rengelink et al. (1997), [19] — Laurent-Muehleisen et al. (1997), [20] — Condon et al. (1998), Condon & Yin (2001), [21] — Wrobel et al. (1998), [22] — Robson et al. (2001), Jenness et al. (2010), [23] — Mingaliev et al. (2017), [24] — Angelakis et al. (2019), [25] — Massardi et al. (2011, 2008), [26] — Planck Collaboration et al. (2016), [27] — Intema et al. (2017), [28] — Hurley-Walker et al. (2017), [29] — Lacy et al. (2020).

Catalog/Telescope	Epoch	Frequency, GHz	Reference
UMRAO	1965–1984	4.8, 8, 14.5	[1]
S4	1972, 1974	2.7, 10.7, 4.9	[2]
TXS	1974–1983	0.365	[3]
6CIII	1976	0.151	[4]
OPM78	1977	1.379, 4.585, 15.064, 22.185, 90	[5]
GBIMO	1979–1996	2.5, 8.2	[6]
OVRO	1979–1982, 2008–2009	10.8, 15	[7]
SRCU1	1979	1.48, 4.9	[8]
RRF95	1979–1994	2.3, 8.4	[9]
VLA4	1980–1981	4.885, 1.465	[10]
7CJR	1984–1987	0.038, 0.151	[11]
MIYUN	1985–1993	0.232	[12]
GB6	1986–1987	4.85	[13]
87GB	1987	4.85	[14]
6CMN	1987	4.85	[15]
Mo30m	1990–1994	90, 150, 142, 230	[16]
SRCT	1990–2000	22, 37, 87	[17]
WENSS	1991	0.325, 0.609	[18]
RGB1	1992, 1994, 1995	5	[19]
NVSS	1993–1996	1.4	[20]
JVAS	1995–1997	8.4	[21]
JCMT	1997–2005	353	[22]
RATAN-600	2005–2014	1.1, 2.3, 4.8, 7.7, 11.2, 21.7	[23]
Effelsberg	2006–2015	2.64–43	[24]
ATCA	2007	20	[25]
PCCS2	2009–2013	30, 44, 70, 100, 143, 217, 353, 545, 8 57	[26]
GMRT (TGSS)	2010–2012	0.15	[27]
GLEAM	2013–2015	0.072–0.231	[28]
VLA55	2016–2019	2–4	[29]

analyze mainly the data collected in the R passband during the mentioned periods.

The optical telescope Zeiss-1000 coupled with the CCD photometer in the Cassegrain focus provides a field of view of about $7'$ with the $0''.22/\text{pixel}$ data sampling. The CCD camera was designed and manufactured in SAO RAS in 2002 based on the 2048×2048 back-illuminated E2V chip CCD 42-40 (Markelov et al. 2000). The pixel size of this popular chip is 13.5 microns.

This instrumental configuration has been almost unchangeable since the start of the observations: the CCD camera has demonstrated very stable operation with only few insignificant failures. The system readout noise is about $4 e^-$, the gain is $2 e^-/\text{ADU}$, and the dark current is about 0.01 ADU per second.

Regular observations of AGNs with a 0.5-meter Ritchey–Chretien telescope (further AS-500/2) manufactured by Astrosib (Novosibirsk, Russian Federation) started in January of 2021, while the observations aimed at search for exoplanets had started with a similar instrument at SAO RAS 1 year before. This instrument with a hyperbolic primary mirror is installed on a fast-tracking “10 Micron GM 4000” high-

precision equatorial mount. Data acquisition is performed using a front-illuminated FLI Proline PL16801 $4K \times 4K$ camera with 9-micron pixels. The FLI CCD camera with Peltier cooling (operation temperature about -40°) coupled with an Atlas focuser and a five-position motorized 50-mm filter wheel are controlled by an industrial PC, which supports all the functions of remote control and data acquisition under a Linux operating system (Valyavin et al. 2022).

The data for the blazar S4 0954+658 have been collected with the AS-500/2 in two instrumental configurations: from January 2021 to April 2022 the FLI camera had been installed in the primary focus (field of view of $1.5^\circ \times 1.5^\circ$ with the $1''.35/\text{pixel}$ sampling), and then in the Cassegrain focus (field of view of $31' \times 31'$ with $0''.46/\text{pixel}$) since April 2022.

The latter variant provided a scale of $0''.92/\text{pixel}$ with the 2×2 data binning, which is in good agreement with our typical $1''.5\text{--}2''$ seeing.

The readout noise and the gain were about $15 e^-$ and $7 e^-/\text{ADU}$ respectively. The dark current for the FLI camera was about 1 ADU per second and was subtracted before other reduction steps.

Both CCD photometers are equipped by similar sets of

filters, which are close to the standard broadband Johnson–Cousins filters given the sensitivity of both CCDs.

The typical integration time for the blazar observations was 300^s for Zeiss-1000 and 120^s for the AS-500/2 respectively.

During the period of object high activity, the integration time was less: up to 60^s for higher time cadence.

4.2 Data reduction

The standard reduction and photometrical techniques were applied to extract the magnitudes of the blazar and nearby reference stars: dark current subtraction, image flat-fielding, integration of the individual object signal within rings of increasing size, etc. The main details of data reduction were described earlier (Vlasyuk 1993).

Bias and dark frames were taken before and after an observing run each night along with twilight-sky flat-field images for preliminary data processing.

The stars from Raiteri et al. (1999) denoted from N2 to N9 were used for calibration of blazar magnitudes.

A comparison with the data obtained on the same nights with different telescopes showed general agreement; in the cases where variations have been detected, they are consistent with the usual variations of the source.

The typical photometrical accuracy of our data is better than $0^m.01$ and between $0^m.01$ and $0^m.02$ for individual frames from the Zeiss-1000 and AS-500/2 telescopes respectively. Under mediocre weather conditions, these values may be 2–3 times worse, as well as when the object is in the low brightness state (R magnitude fainter 16^m).

In order to provide a joint analysis of the optical and radio data, we averaged our measurements over individual nights and transformed the resulting values into fluxes according to the constant from Mead et al. (1990).

4.3 Long-term brightness curve

The long-term brightness curve of S4 0954+658 is shown in Fig.1 for a total of 670 nights over 20 yrs from February 2003 to June 2023. These data include 423 nights from the Zeiss-1000 and 306 nights from the AS-500/2 (January 2021–June 2023). For 60 nights data have been collected from both telescopes and we show the averaged values.

The average observing epochs (MJD and yyyy.mm.dd), number of observations for each night N_{obs} , and obtained fluxes R with their errors σ_R expressed in mJy are presented in Table A1. Below in this paper we use the fluxes in the R band, not corrected for the galactic extinction. The first few rows of this table are presented here in Table 2.

A detailed inspection of the data from Table A1 revealed the presence of some epochs with high σ_R , above 0.1 mJy. Sometimes σ_R may exceed 1 mJy and even reaches a value as high as ~ 2.6 mJy for the epoch MJD = 59711. In combination with a significant amount of flux estimates, it can be a reliable indicator of an intraday variability event in the blazar. The more detailed analysis of these events are now in preparation. Let us just note that our total database of photometric observations in the R band includes about 2120 and 5200 individual images for the Zeiss-1000 and AS-500/2 telescopes respectively.

Our total set of observations can be divided into three time intervals for the following analysis.

Table 2. Averaged R-band measurements of S4 0954+658 in February 2003 – June 2023. Columns are as follows: (1) and (2) - observing epochs —MJD and date in yyyy.mm.dd format respectively, (3) - the number of observations N_{obs} , (4) — the flux densities in the R band and their errors in mJy. A short fragment is presented; the full version is available in attachment.

MJD epoch 1	yyyy.mm.dd 2	N_{obs} 3	R_{flux} and σ_R , mJy 4
52678	2003.02.07	1	1.24 ± 0.02
52679	2003.02.08	3	1.39 ± 0.03
52699	2003.02.28	2	1.12 ± 0.01
52701	2003.03.02	4	1.56 ± 0.09
52702	2003.03.03	8	1.31 ± 0.03
52705	2003.03.06	10	2.02 ± 0.06

The first interval covers the period from February 2003 to December 2014 (MJD from 52600 to 57000), during which the blazar had been in a low state in the optics. According to our data, its flux did not exceed a level of 2 mJy. One should note the presence of seasonal gaps in our data, mainly caused by the location of the object at a high zenith distance during short summer nights. An analysis of the literature data showed that we have actually lost only one optical outburst of S4 0954+658 with a maximum flux of about 4.5 mJy in March–April 2011, which was detected and studied in (Morozova et al. 2014).

The second cycle spans the period of December 2014–June 2018 (MJD from 57000 to 58300), when S4 0954+658 underwent an outburst with $R \sim 14.4$ mJy in February 2015 (Morozova et al. 2016; Volvach et al. 2016) and less intensive post-outbursts with $R \sim 4.2$ mJy (MJD = 57187), 5.5 mJy (MJD = 57368), 3.1 mJy (MJD = 57830), and 5.4 mJy (MJD = 58227). During this interval the faintest R band flux was 0.44 mJy on MJD = 57844.

The third interval covers the observations between July 2018 and June 2023. The flux of S4 0954+658 ranged between 0.48 mJy (MJD = 59955) and 16.4 mJy (MJD = 59713) during this period. A careful analysis of the data from this cycle reveals a complex structure of the light curve, which may be approximated as a superposition of two processes.

The first one demonstrates quite slow flux variation with a characteristic time of about 50 days: one can count 5 episodes of blazar brightening over last 1000 days.

The second process presents by much faster flares. All these episodes with different intensity, being separated by short intervals of fainter flux, also consist of groups of faster events: between 5 and 9 occasions with a typical repeating time of about 7–20 days. One episode at MJD = 59670–59750, which includes the brightest optical state in our data at MJD = 59711, is shown in the top panel of Fig.2 with a grey strip.

Just to illustrate the fastest flux variation over our monitoring campaign, we present in Fig.2 (bottom) the S4 0954+658 flux variation during the night MJD = 59711. The data were taken using the AS-500/2 telescope with a 90^s cadence during a 4^h time interval. The brightness of the blazar changed from 10.5 to 16 mJy in 100 min and from 16 mJy to 13 mJy in 70 min. The steepest fragments of the light curve at epochs 0.81–0.83 and 0.84–0.88 demonstrated a curve slope of ~ 6

and ~ 4 mJy/hour respectively. The following decline stage have a slope of ~ 2 mJy/hour.

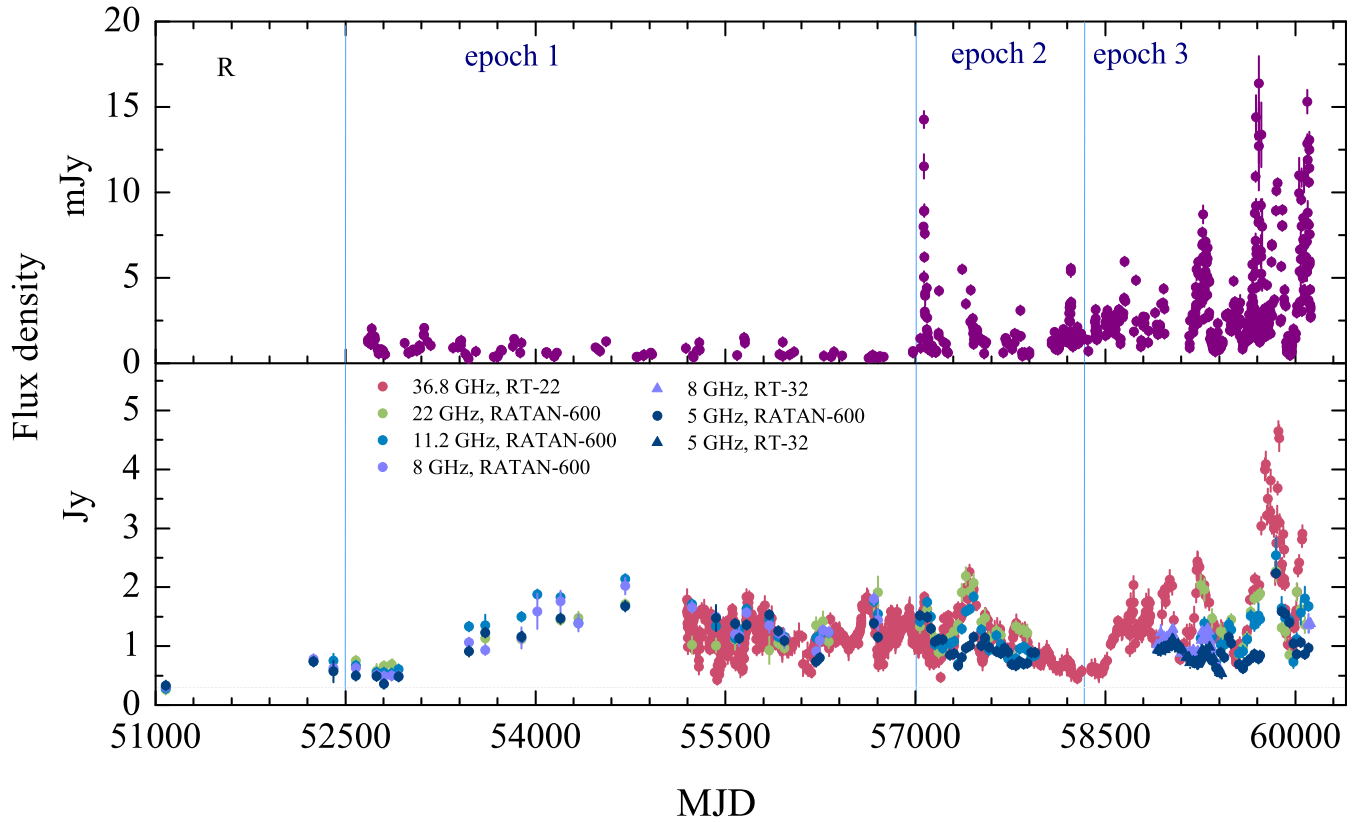


Figure 1. Top: optical light curve of S4 0954+658 over the time interval from Feb 2003 to Jun 2023. Bottom: the RATAN-600 (1998–2023) and RT-32 (2021–2023) flux densities at 5 (dark blue), 8 (lilac), 11 (turquoise), and 22 (green) GHz; the RT-22 36.8 GHz measurements in 2009–2023 (red). The blue lines indicate the observing epochs (1, 2, and 3) discussed in this paper, with different states in the optical band. The grey line indicates the lower level of radio flux densities of about 0.3 Jy at 5–22 GHz in 1998.

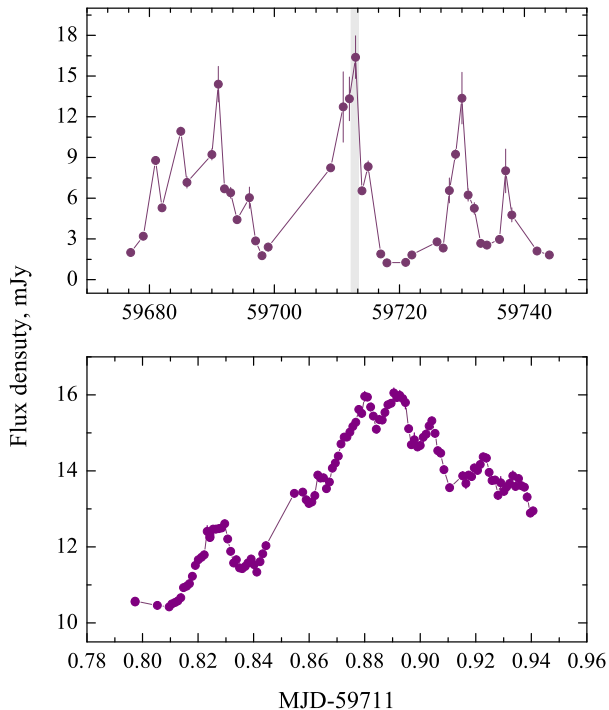


Figure 2. Top: a fragment of the optical light curve of S4 0954+658 over the time interval from Apr 2022 to Jun 2022 with the most prominent outbursts. The gray strip indicates the night of the strongest outburst. Bottom: an example of an intraday variability event (the outburst on the night of May 12/13, 2022). The cadence of the data is about 90^s , the total time interval is about 4^h .

5 RADIO OBSERVATIONS

5.1 RATAN-600

The radio flux densities were measured with the RATAN-600 telescope with a 600-m circular multi-element antenna operating in the transit mode (Parijskij (1993)). The observations provide measurements of 1–22 GHz broadband spectra simultaneously within 3–5 minutes when a source moves along the focal line where the receivers are located. The angular resolution (measured by the full width at half maximum parameter, FWHM) in this mode depends on the antenna elevation angle, and the resolution along declination FWHM_{Dec} is three to five times worse than that along right ascension FWHM_{RA} . The angular resolution along RA and Dec calculated for the average angles is presented in Table 4 for the 6 observing frequencies. The detection limit for a RATAN-600 single sector is approximately 5 mJy at 4.7 GHz (integration time is about 3^s) under good conditions and at the average antenna elevation angle (Dec $\sim 0^\circ$).

The observations were carried out in 1998–2023 at the South sector and at “South+Flat” regime with two radiometric complexes at six frequencies: 0.96/1.25/1.1, 2.25, 3.95/4.7, 7.7/8.2, 11.2 and 21.7/22.3 GHz. The blazar was observed from 3 to 7 times for each epoch to improve the signal-to-noise (S/N) ratio. The measurements were processed using the automated data reduction system (Kovalev et al. 1999; Tsybulev 2011; Udovitskiy et al. 2016; Tsybulev et al. 2018) and the Flexible Astronomical Data Processing System (FADPS) standard package modules (Verkhodanov 1997) for

the broadband RATAN-600 continuum radiometers. We used the following seven flux density secondary calibrators: 3C 48, 3C 147, 3C 286, NGC 7027, DR 21, 3C 295 and 3C 309.1. The flux density scales were calculated based on Baars et al. (1977) and Perley & Butler (2013, 2017). The measurements of the calibrators were corrected for the angular size and linear polarization according to the data from Ott et al. (1994) and Tabara & Inoue (1980).

The obtained flux densities with their errors σ , observing epochs averaged over N_{obs} days (MJD and yyyy.mm.dd), and number of observations N_{obs} are presented in Table A2. The fragment of this table is presented in Table 3. Since the observing frequencies of the RT-32 (5.05, 8.63 GHz), RT-22 (22.2 GHz), and RATAN-600 (4.7, 8.2, and 22.3 GHz) are very close, we further use the rounded values of the frequencies: 22, 8, 5, and 1 GHz for the ease of description and analysis.

The total flux density error includes the uncertainty of the RATAN-600 calibration curve, and the error of the antenna temperature measurement (Udovitskiy et al. 2016) is calculated by the equation:

$$\left(\frac{\sigma_S}{S_\nu}\right)^2 = \left(\frac{\sigma_c}{g_\nu(h)}\right)^2 + \left(\frac{\sigma_m}{T_{\text{ant},\nu}}\right)^2, \quad (1)$$

where σ_S is the total flux density standard error; S_ν , the flux density at a frequency ν ; σ_c , the standard calibration curve error, which is about 1–2% and 2–5% at 4.7 and 8.2 GHz respectively; $g_\nu(h)$, the elevation angle calibration function; σ_m , the standard error of the antenna temperature measurement; and $T_{\text{ant},\nu}$ is an antenna temperature. The systematic uncertainty of the absolute flux density scale (3–10% at 1–22 GHz) is not included in the total flux error. For S4 0954+658 the average flux density errors at 22, 11, 8, 5, 2, and 1 GHz are 10, 7, 7, 5, 17, and 22% respectively.

The RATAN-600 measurements during 1997–2023 at 22, 11, 8, and 5 GHz show continuous flux densities variations by a factor of five, from 0.5 up to 2.5 Jy.

5.2 RT-32

A weekly monitoring of radio flux densities of S4 0954+658 were carried out with two RT-32 radio telescopes of IAA RAS at the Zelenchukskaya and Badary observatories in the single-dish mode from 1 March 2020 to 24 July 2021. Alongside, in June–July 2023 several additional observations were made. All the measurements were performed at 5.05 and 8.63 GHz with a bandwidth of 900 MHz for both and with cooled receivers.

The observations were conducted in the drift scan mode. One scan lasted ~ 1 minute at 8.63 GHz and ~ 1.5 minutes at 5.05 GHz with 1 second registration time. To accumulate the signal, the scanning cycle was repeated a required number of times, forming a continuous observing set. About 30 to 50 scans were carried out for one object observation.

3C 48, 3C 147, 3C 295 and 3C 309.1 were used as reference sources. The flux density scales were calculated similarly to the RATAN-600 observations (Baars et al. 1977; Perley & Butler 2013).

The observed data were processed with the original program package CV (Kharinov & Yablokova 2012) and the Database of Radiometric Observations. The drift scans were

Table 3. RATAN-600 measurements in 1998–2023 and the RT-32 data in 2020–2023: observing MJD epoch (Col. 1), date in yyyy.mm.dd format (Col. 2), the number of observations N_{obs} (Col. 3), the flux densities at 21.7/22.3, 11.2, 7.7/8.2/8.6 GHz, 4.7/5.1, 2.3, and 0.96/1.1/1.2 GHz and their errors in Jy (Cols. 4–9), the name of the telescope (Col. 10). The number of observations N_{obs} is indicated if information is available; for the RT-32 the number of observations is given for two frequencies. A short fragment is given here; the full version of Table is available in attachment.

MJD epoch	yyyy.mm.dd	N_{obs}	S_{22}, σ	$S_{11.2}, \sigma$	S_8, σ	S_5, σ	$S_{2.3}, \sigma$	S_1, σ	Telescope
1	2	3	4	5	6	7	8	9	10
57795	2017.02.10	5	1.33 ± 0.10	0.79 ± 0.07	–	0.67 ± 0.03	–	–	RATAN-600
57823	2017.03.10	6	1.28 ± 0.10	0.95 ± 0.03	–	0.74 ± 0.04	–	–	RATAN-600
57854	2017.04.10	5	1.27 ± 0.10	0.99 ± 0.06	–	0.70 ± 0.04	–	–	RATAN-600
58909	2020.03.01	43	–	–	1.02 ± 0.06	–	–	–	RT-32
58916	2020.03.08	62/42	–	–	0.95 ± 0.04	0.93 ± 0.08	–	–	RT-32
58923	2020.03.15	88	–	–	–	0.93 ± 0.04	–	–	RT-32
58937	2020.03.29	67/86	–	–	1.22 ± 0.14	0.92 ± 0.03	–	–	RT-32

Table 4. RATAN-600 continuum radiometer parameters: the central frequency f_0 , the bandwidth Δf_0 , the detection limit for point sources per transit ΔF . $\text{FWHM}_{\text{RA} \times \text{Dec}}$ is the angular resolution along RA and Dec calculated for the average angles.

f_0	Δf_0	ΔF	$\text{FWHM}_{\text{RA} \times \text{Dec}}$
GHz	GHz	mJy/beam	
22.3	2.5	50	$0'17 \times 1'6$
11.2	1.4	15	$0'34 \times 3'2$
8.2	1.0	10	$0'47 \times 4'4$
4.7	0.6	8	$0'81 \times 7'6$
2.25	0.08	40	$1'71 \times 15'8$
1.25	0.08	200	$3'07 \times 27'2$

filtered, rejected if spoiled considerably by weather or industrial noise, averaged and fitted with a Gaussian curve. Before averaging, the zero level of each scan was approximated by a parabola. The correction for pointing offsets was applied to the scans by the peak values of the Gaussian fits. The antenna temperature and its error were estimated from the Gaussian analysis of the averaged scan. The reference signal error of the noise generator is less than 1% and is also included into the result. The average flux density errors for the target source at 8.63 GHz and 5.05 GHz amount to 4% both.

The obtained RT-32 flux densities with their errors σ , average observing epochs (MJD and yyyy.mm.dd), and number of observations N_{obs} are presented in Table A2 (the fragment is in Table 3).

5.3 RT-22

The observations at 36.8 GHz were carried out with the radio telescope RT-22 (CrAO, Simeiz) using modulation radiometers in the beam pattern modulation mode (Vol’vach et al. 2008). Before measuring an antenna temperature, the coordinates were refined by scanning in right ascension and declination. The antenna temperature of the source was determined as the difference between the responses of the radiometer at the two mentioned antenna positions, averaged over 30 seconds. Depending on the signal-to-noise ratio of the radiometer response, a series of 30–60 measurements was carried out, after which the average value of the signal and its root-mean-square error were estimated. The absorption of radiation in the Earth’s atmosphere was taken into account

Table 5. A fragment of Table A3: the RT-22 measurements in 2009–2023: MJD epoch (Col. 1), yyyy.mm.dd (Col. 2), the flux densities at 36.8 GHz and their errors in Jy (Col. 3).

MJD epoch	yyyy.mm.dd	$S_{36.8}, \sigma$
1	2	3
55196	2009.12.30	1.79 ± 0.18
55198	2010.01.01	1.59 ± 0.22
55199	2010.01.02	1.54 ± 0.23
55200	2010.01.03	1.39 ± 0.21
55202	2010.01.05	1.33 ± 0.12
55204	2010.01.07	0.99 ± 0.13

by the “atmospheric cuts” method, in which the differences in antenna temperatures at fixed elevation angles were registered. The antenna temperatures corrected for the absorption of the radiation in the Earth’s atmosphere were recalculated into spectral flux density according to observations of the calibration sources (Volvach et al. 2016; Sotnikova et al. 2023).

The median value of the flux density errors at 36.8 GHz is 10%. The obtained flux densities and their errors are presented in Table A3. The first few rows of this table is presented in Table 5.

6 RADIO PROPERTIES

6.1 Light curves

The light curves of the blazar at radio frequencies show continuous flux density variations from 1998 to 2023 (Fig. 1). The lower state of the source was observed in 1998, at that epoch the flux densities varied from 0.59 to 0.26 mJy at 22–0.96 GHz (Fig. 3). In the time period of 2003–2023, for which the optical measurements are available, we separate three epochs (1, 2, and 3) with different states of the blazar in the optical and radio bands (blue lines in Fig. 1). During epoch 1 (February 2003 – December 2014), the blazar showed flux density variations from 0.55 to 2.1 Jy at 11.2 GHz. The second epoch (epoch 2, December 2014 – July 2018) revealed a radio flare with a flux maximum of 1.99 Jy at 36.8 GHz in January 2016, which started later at 5–11 GHz (March 2016). During the rest of the time of epoch 2, the radio flux density was slowly decreasing. During epoch 3 (July 2018 – June 2023), five large radio flares were observed with differ-

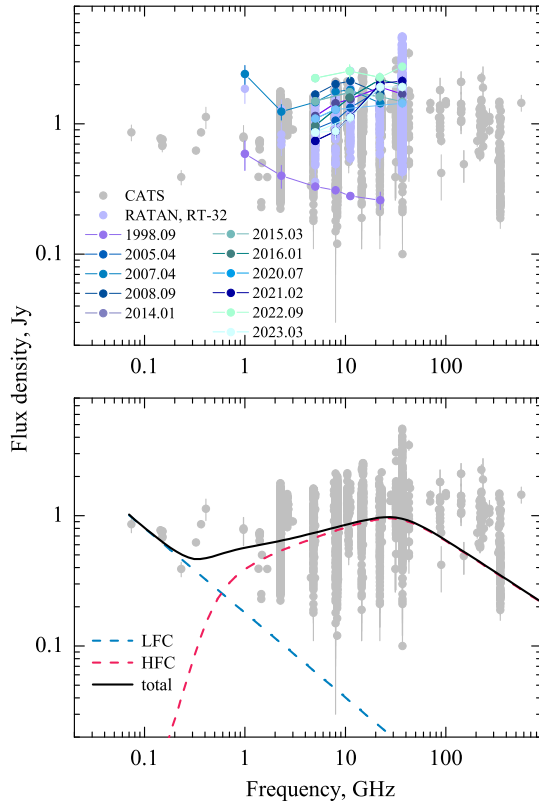


Figure 3. The broadband radio spectra of S4 0954+658. Top: the literature data from CATS are shown with the grey circles. The new RATAN-600, RT-32, and RT-22 data at 1–36.8 GHz are marked by lilac color. The spectra during the several flare epochs are shown by the same colors as in Fig. 1. The lower radio spectrum (blue circles) corresponds to the quietest state of the blazar in 1998. Bottom: the results of simulating the average “total” spectrum via two model spectra components (LFC and HFC), similar to that for the blazar 1502+10 in [Sotnikova et al. \(2022b\)](#).

ent amplitudes (up to 4.65 Jy at 36.8 GHz) and duration. We have stopped the observing run of epoch 3 at the beginning of the next (sixth) flare, while in the optical band the flux is almost down.

6.2 Broadband radio spectra

S4 0954+658 is an extremely variable AGN. Its broadband radio spectra (Figure 3) show a wide variety of shapes: from steep ($\alpha < -0.5$) to rising ($\alpha > 0$). During the 25 years of the RATAN-600 observations, the spectral index α_{11-22} was less than -0.5 only during three epochs: Feb 2010, Oct 2011, and Jan 2023. We defined the spectral index from the power-law $S_\nu \sim \nu^\alpha$ (S_ν is a flux density at the frequency ν , and α is a spectral index). The average spectrum of S4 0954+658 has a peak at mm-waves in the observer’s frame of reference.

According to the Hedgehog jet model ([Kovalev et al. 2000](#)), suggested by N. S. Kardashev in 1969, the longitudinal magnetic field B of the radio jet depends on the distance r as $B = B_0 (r/r_0)^{-2}$. In Figure 3 the fitting of the two components in this model to the observations is shown. The blue dotted line represents the fitting of the low frequency component (LFC) to the optically thin model synchrotron emission of nearly constant extended structures of the object up to kpc

Table 6. Main physical parameters of the jet determined from fitting the flux densities in Figure 3 using equations (2)–(4) for two sorts of emitting particles: jet magnetic field B , brightness temperature T_b , angular diameter Θ , and the relation of the magnetic energy density $W_H = B^2/8\pi$ to the energy density W_E of emitting particles.

Particles	B Gauss	T_b K	Θ mas	W_H/W_E
electrons	20	$5 \cdot 10^{10}$	0.08	$W_H \gg W_E$
protons	$4 \cdot 10^4$	$9 \cdot 10^{13}$	0.002	$W_H \gg W_E$

scales. The red dotted line represents the average spectrum of the model jet as the second component, the high frequency component (HFC). The black line (marked as “total”) is the sum of the red and blue dotted lines. Such average model spectra could be observed if the continuous flux $dN(t)/dt$ of the emitted particles across the base of the jet is constant for a long time (about 10-20 years). The variability of $dN(t)/dt$ is converted in the model to the variability of the HFC and the total spectrum.

We obtained the following fitted physical parameters of the jet: the angle to the observer’s line of sight $\vartheta \sim 1.5^\circ$, the flux S_m and the frequency ν_m of the jet spectrum maximum $S_m \sim 0.70$ Jy and $\nu_m \sim 60$ GHz, $\gamma \sim 2.0$, and supposed $\gamma_E \sim 300$.

The following physical parameters of the jet, neglecting the redshift, can be estimated using the fitted parameters ([Sotnikova et al. 2022b](#)):

$$B_\perp/M_{2e} \sim 0.82 \cdot 10^{-6} \cdot \nu_m \cdot \gamma_E^{-2}, \quad (2)$$

$$T_b/M_{2e} \sim 1.5 \cdot 10^8 \cdot \gamma_E, \quad (3)$$

$$\Theta \sim \lambda_m \left(\frac{2S_m}{\pi k_B T_b} \right)^{1/2}. \quad (4)$$

Here ν_m (Hz), λ_m (m), and S_m (Watt/(m²Hz)) are the frequency, wavelength, and flux density of the spectrum maximum; the gamma-factor $\gamma_E = E/(Mc^2)$ of emitted particles is supposed to have the same value for electrons and protons; $B_\perp = B \sin \vartheta$, $M_{2e} = 1$ for electrons, and $M_{2e} = 1836$ for protons. Θ (rad), k_B and T_b (K) are the angular diameter of the emitting jet in the picture plane, the Boltzman constant, and the brightness temperature. The estimated parameters are shown in Table 6.

6.3 Variability estimates

In order to characterise the variability of the flux density, we have computed the variability and modulation indices and the fractional variability. The first and third characteristics take into account measurement uncertainties, while the modulation index and the fractional variability are less sensitive to outliers. The variability V_S index was calculated using the formula from [Aller et al. \(1992\)](#):

$$V_S = \frac{(S_{\max} - \sigma_{S_{\max}}) - (S_{\min} + \sigma_{S_{\min}})}{(S_{\max} - \sigma_{S_{\max}}) + (S_{\min} + \sigma_{S_{\min}})} \quad (5)$$

where S_{\max} and S_{\min} are the maximum and minimum flux densities over all epochs of observations; $\sigma_{S_{\max}}$ and $\sigma_{S_{\min}}$ are

their errors. This formula prevents one from overestimating the variability when there are observations with large uncertainties in the data. We obtain a negative value of V_S in the case where the flux error is greater than the observed scatter in the data.

The modulation index, defined as the standard deviation of flux density σ_S divided by the mean flux density \bar{S} , was calculated as in Kraus et al. (2003):

$$M = \frac{\sigma_S}{\bar{S}}. \quad (6)$$

The fractional variability F_S is defined as in Vaughan et al. (2003):

$$F_S = \sqrt{\frac{V^2 - \sigma_{\text{err}}^2}{\bar{S}^2}} \quad (7)$$

where V^2 is the variance or dispersion of the process, \bar{S} is the mean flux density, and σ_{err} is the root mean square error. The uncertainty of F_S is determined as:

$$\Delta F_S = \sqrt{\left(\sqrt{\frac{1}{2N}} \frac{\sigma_{\text{err}}}{F_S * \bar{S}^2}\right)^2 + \left(\sqrt{\frac{\sigma_{\text{err}}^2}{N}} \frac{1}{\bar{S}^2}\right)^2} \quad (8)$$

The values of V_S , M , and F_S in the optical band and at four radio frequencies are given in Table 7. The number of observing epochs N_{obs} and the timescale t play a key role in searching for AGN variability. It is known that variability increases with the number of observations, which can be explained by the fact that peaks of variability are easily missed when sampling is very sparse (Tornikoski et al. 2000).

6.4 The contribution of refractive interstellar scintillation

The observed flux density variability could be caused by either intrinsic (related to the source's properties) or extrinsic factors. The extrinsic ones are caused by the interaction of source radio emission with an inhomogeneous propagation medium. The flickers caused by scattering on the inhomogeneities of the interplanetary medium have a characteristic timescale of the order of a second or less (Morgan et al. 2018), so they are smoothed out in RATAN-600 observations due to the relatively long scan time of 3–5 minutes during the source's transit. Similarly, for measurements at other radio telescopes, interplanetary flickering is also insignificant due to the typical continuum flux density measurement time being obviously longer than one second.

The scintillations caused by the propagation of radio waves in the interstellar medium can be diffractive and refractive. The diffractive scintillation typically requires an extremely compact source to be detected, and observations must be made in a narrow frequency band to resolve the fine-scale structures responsible for the diffractive scintillation (Narayan 1992). This is because the scintillation pattern can be highly frequency-dependent. The continuum radio measurements are carried out in a wide band (from hundreds of MHz to several GHz); therefore, this type of flickering can not be detected in the RATAN-600 and RT-32 data.

Let's estimate the possible contribution of refractive interstellar scintillations (RISS) to the variability at the RATAN-600 frequencies (1.2, 2.3, 4.7, 8.2, 11.2, and 22.3 GHz) for S4 0954+658. This source lies about 43° from

the galactic plane. According to Walker (1998), the transition frequency defining the boundary between the modes of strong and weak scattering is approximately 8 GHz for the blazar. We will adopt this value of the transition frequency to estimate the modulation level of the flux density and its timescale.

We estimated the angular size as $\theta_s = 5 \times \theta_{\text{min}}$, where $\theta_{\text{min}} = 0.6\sqrt{S}/\nu$ is the minimum angular size for the stationary source of synchrotron radiation (Kellermann & Owen 1988), S is the flux density (in Jy) at the observer's frequency (in GHz). We adopted $S = 1$ Jy, taking into account the shape of the S4 0954+658 average radio spectrum.

We followed the formulas from Walker (1998) to calculate the modulations of the flux density m and their typical timescales, the results are presented in Table 8. We conclude that the modulation level is about 1%, which is significantly less than the average values of the obtained variability level. Therefore, the contribution of refractive scintillations to the total variability is insignificant.

7 CHARACTERISTICS OF THE FLARES

7.1 Optical flares

A detailed inspection of the brightness curve in the R band shows the presence of many flares with different temporal characteristics. Primarily, it is true for our data obtained during epochs 2 and 3.

The observed brightness curve for epoch 3 may be approximated as a combination of slow and fast flares. The first ones have typical variation time of about 250 days and amplitudes between 1 and 3 mJy. The MJD epochs of the maxima of slow flares are: 59250, 59510, 59710, 59870, and 60070. Their characteristic time scales are close to 50^d .

The criterion of flare detection, flux exceeding the neighboring level 4–5 times, allowed us to identify 44 faster flares within the Jan 2021–Jun 2023 time interval. They have typical variation time between 7 and 20 days (Fig. 4) with timescales in the range of 2–5 days and amplitudes between 2 mJy (faintest slow flare with the maximum on MJD = 59510) and 20 mJy (most powerful flare with the maximum on MJD = 59710).

7.2 Radio flares

The radio light curve at 36.8 GHz demonstrates about 20 flares in 2009–2023 with the flux density maximum higher than 1.5 Jy. It is the best-sampled radio light curve, which allows us to investigate the behaviour of radio flares. The light curve ends in April 2023 by a sharp increasing of the flux density and, apparently, corresponds to the last optical flare which started in February 2023.

The total flux density variations in AGNs $\Delta S(t)$ can be well modeled by a superposition of flare components at high radio frequencies, more than 10 GHz (Valtaoja et al. 1999; Hovatta et al. 2009). The increase, decrease, and decay of each flare are modeled by the following relations:

$$\Delta S(t) = \begin{cases} \Delta S_{\text{max}} \cdot e^{(t-t_{\text{max}})/\tau_1}, & t < t_{\text{max}} \\ \Delta S_{\text{max}} \cdot e^{(t_{\text{max}}-t)/\tau_2}, & t > t_{\text{max}} \end{cases}$$

where ΔS_{max} is the maximum amplitude of a radio flare (Jy),

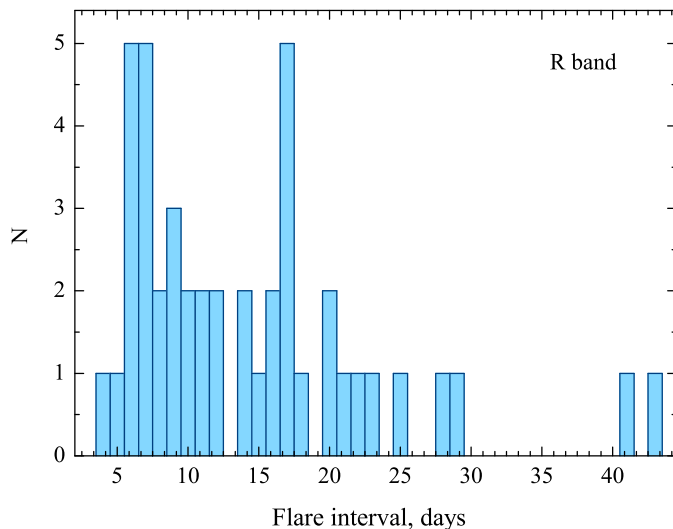
Table 7. The values of V_S , M , and F_S in the optical band and at radio frequencies of 5, 8, 11.2, 22, and 36.8 GHz.

Frequency (GHz)	V_S	M	F_S	V_S	M	F_S	V_S %	M	F_S	V_S	M	F_S
	all			epoch1			epoch2			epoch3		
5	73.1	30.5	29.8	61.4	36.8	35.1	35.0	23.4	22.5	58.1	28.2	27.6
8	70.1	30.6	29.1	53.5	35.7	33.4	–	–	–	35.9	20.5	19.0
11	77.1	33.0	31.9	56.0	33.6	32.6	40.7	28.0	26.8	46.9	30.2	27.6
22	74.9	31.8	30.1	40.2	31.3	28.2	37.4	28.1	26.2	37.5	27.0	24.8
36.8	80.6	38.3	37.0	56.2	21.3	18.6	64.0	33.9	32.0	73.3	49.1	48.2
optical band	96.4	93.2	92.7	76.8	50.0	49.7	93.7	101.6	101.0	93.6	78.5	77.9

Table 8. RISS modulation of the flux density m and its typical timescale estimates t for the RATAN-600 frequencies at a transitional frequency of 8 GHz.

Frequency (GHz)	Source's size (mas)	m (%)	t days
1.2	2.50	2.4	52.1
2.3	1.30	1.4	27.2
4.7	0.64	0.8	13.3
8.2	0.37	0.5	7.6
11.2	0.27	0.4	5.6
22.3	0.13	0.2	2.8

2002). The agreement between the appearance of VLBA components and the time period of radio flares is quite good. Indeed, the VLBA 43 GHz data⁵ show the emergence of a new compact and highly polarized (polarization degree $p > 15\%$) structure in April 2015, August 2019, August 2020, and August 2022.

**Figure 4.** The distribution of time intervals between subsequent flares for epoch 3 in the R band.

t_{\max} is the epoch of the flare maximum; τ_1 and τ_2 are the time of flare rising and falling (in days). We used the actual values of both τ_1 and τ_2 calculated from the light curves (Table 9), while in the original work (Valtaoja et al. 1999) the authors used $\tau_2 = 1.3\tau_1$. We revealed and modelled six stronger flares with amplitudes of about 2 Jy in the light curve at 36.8 GHz (Fig. 5). Their characteristics are presented in Table 9. It is also known that individual exponential flares correspond to the appearance of new VLBA components, which indicates that the flares obtained from the fits are related to actual jet physics (Lähteenmäki & Valtaoja 1999; Savolainen et al.

⁵ https://www.bu.edu/blazars/VLBA_GLAST/0954.html

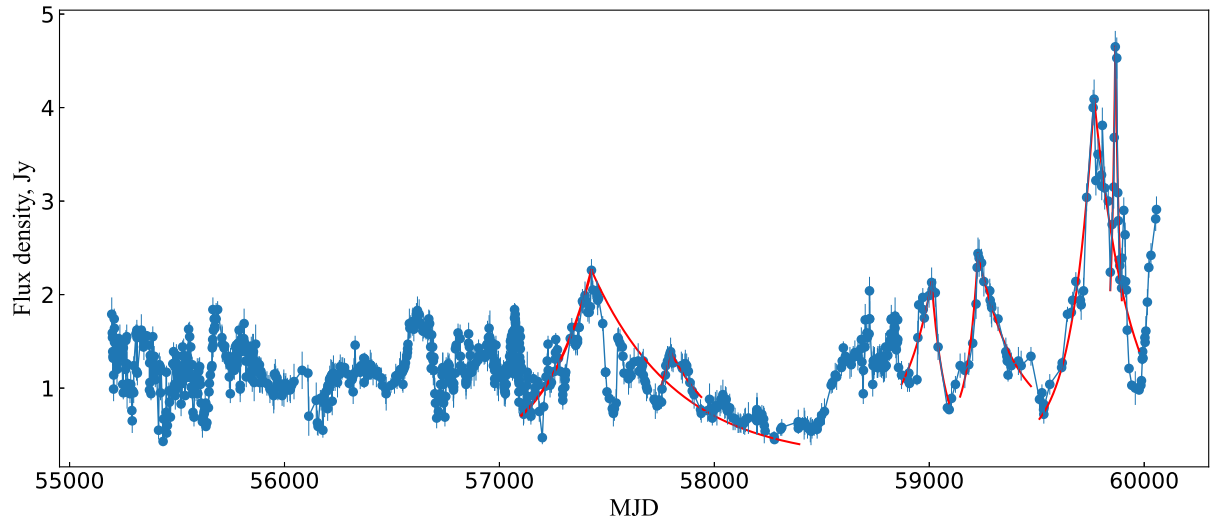


Figure 5. The light curve at 36.8 GHz approximated by the most bright six radio flares, with $S_{\max} > 2$ Jy, depicted by red lines.

Table 9. Main parameters of the large exponential flares at 36.8 GHz data.

t_{\max} MJD	ΔS_{\max} Jy	τ_1 days	τ_2 days	τ_2/τ_1
57428.19	2.035	227 ± 10	394 ± 18	1.7
57796.4*	1.025	96 ± 10	223 ± 25	2.3
59010.87	1.745	143 ± 17	60 ± 9	0.4
59226.65	1.87	49 ± 7	173 ± 10	3.5
59766.85	3.73	102 ± 5	164 ± 13	1.6
59865.4	3.615	18 ± 2	22 ± 2	1.2

We have obtained different flare characteristics such as flare duration τ_1, τ_2 and τ_2/τ_1 relation (Table 9). It is an expected result because the light curve at 36.8 GHz has complex character with a great number of small flares. For example, we see a small flare at a decrease of a large flare with $t_{\max} = 57428.19$ MJD (it is denoted by asterisk in the Table 9). The large flare with $t_{\max} = 59865.4$ MJD happened during the decrease of the strongest flare ($t_{\max} = 59766.85$ MJD). These flares have approximately equal ΔS_{\max} of about 3.7 Jy, but their timescales differ by 5–8 times. Thus the light curve at the high frequency of 36.8 GHz reflects the features of non-stationary processes with timescales from weeks to months.

8 STRUCTURE FUNCTION ANALYSIS

The structure function (SF) is a method of searching for typical time scales and periodicities in non-stationary processes (Simonetti et al. 1985; Hughes et al. 1992). The SF analysis provides a method of quantifying time variability and gives information on the nature of the process that caused the variations. A characteristic time scale in a light curve, defined as the time interval between a maximum and an adjacent minimum or vice versa, is indicated by a maximum of the structure function, whereas periodicity in the light curve causes a minimum (Heidt & Wagner (1996)).

The structure function of the first order normalized to the variance of the signal σ^2 is usually determined as:

$$D_1(\tau) = \langle \{[f(t) - f(t + \tau)]\}^2 \rangle, \quad (9)$$

where $f(t)$ is the signal at a time t , and τ is the lag. The slope of the power part of the curve is estimated as:

$$b = d \log D_1 / d \log \tau. \quad (10)$$

An ideal SF consists of two plateaus and a straight line with slope b between them. The X -axis is the logarithm of the time lag, τ , and Y -axis shows the logarithm of $D(\tau)$. One of the important characteristics of the structure function is the point where the SF reaches its higher plateau with an amplitude equal to $2\sigma^2$. This timescale gives the maximum timescale T_{\max} of correlated signals or, equivalently, the minimum time scale of uncorrelated behavior. The slope between two plateaus determines the nature of the variable process. The light curve can be modelled as a combination of white (flicker) and red (shot) noises, and in this case the slope is between 0 and 1 (Hughes et al. 1992). For a single dominating outburst in the light curve, the slope is usually steeper than 1. If the slope $b \sim 2$, then there is a strong linear trend or a strong periodic oscillation (Hufnagel & Bregman 1992).

Table 10. Parameters of the SF for the R band and at 5, 11.2, 22, and 36.8 GHz.

Frequency, GHz	b	$\log(\tau)$, days	b	$\log(\tau)$, days	b	$\log(\tau)$, days
epoch 1		epoch 2		epoch 3		
5	2.2	3.0	1.8	2.3	2.7	2.2
11.2	2.3	3.0	–	–	2.0	2.1
22	3.3	2.7	1.7	2.2	2.9	2.0
36.8	1.3	1.9	–	–	1.1	2.3
R band	1.1	2.5	0.8	2.0	0.6	2.0

In this work, for the non-uniform and finite data series $f(i)$ with $i = 1, 2, \dots, N$, obtained from the original temporally non-uniform observed data series by partitioning into intervals with the values averaged over the interval, the first-order structure function is calculated as:

$$D_1(k) = \frac{1}{N_1(k)} \sum_{i=1}^N w(i)w(i+k)[f(i+k) - f(i)]^2, \quad (11)$$

where $N_1(k) = \sum w(i)w(i+k)$ and the weight factor $w(i)$ is equal to 1 if the observations exist in the interval i and is 0 if there are no observations. For $k = 1, 2, \dots, L$, we construct our own set of intervals. The initial time interval $k = 1$ is chosen in such a way that it is equal to or slightly larger than the average time interval between observations (ignoring very long gaps in them). For radio frequencies an interval of about 60 days was taken as the initial time interval, at a frequency of 36.8 GHz it was 2 days, and 4 days for the optical data. The final interval $k = L$ is calculated based on the length of the time scale of the original sequence so that all values of the original series are divided into two intervals.

The error of the structure function is calculated from the error percentage of the original function in the interval:

$$\sigma\% = \frac{1}{N - n - 1} \sqrt{\left(\frac{\sigma_t}{f(t)}\right)^2 + \left(\frac{\sigma_{t+\tau}}{f(t+\tau)}\right)^2}. \quad (12)$$

We have computed the SF for the three epochs (1, 2, and 3) in the radio and optical bands (Fig. 6). To measure the slope b , we used all data points between the lower and upper plateaus. The SF parameters, b and $\log(\tau_s)$, are given in Table 10. Due to the small number of data points, we could not construct the SF at 8 GHz. We also cannot determine the second plateau for epoch 2 at 11.2 GHz (large scattering of data points) and for epoch 2 at 36.8 GHz (it does not reach the value of the signal variance σ^2). We obtained $b \approx 2-3$ for 5–22 GHz for the three epochs and $b \approx 1.0$ for 36.8 GHz and the R band. The characteristic time scale τ is about 100 days for epochs 2 and 3. For epoch 1, $\log(\tau)=3$, which corresponds to 1000 days at 5–22 GHz and the R band, and $\log(\tau)=2$, or τ is 100 days at 36.8 GHz.

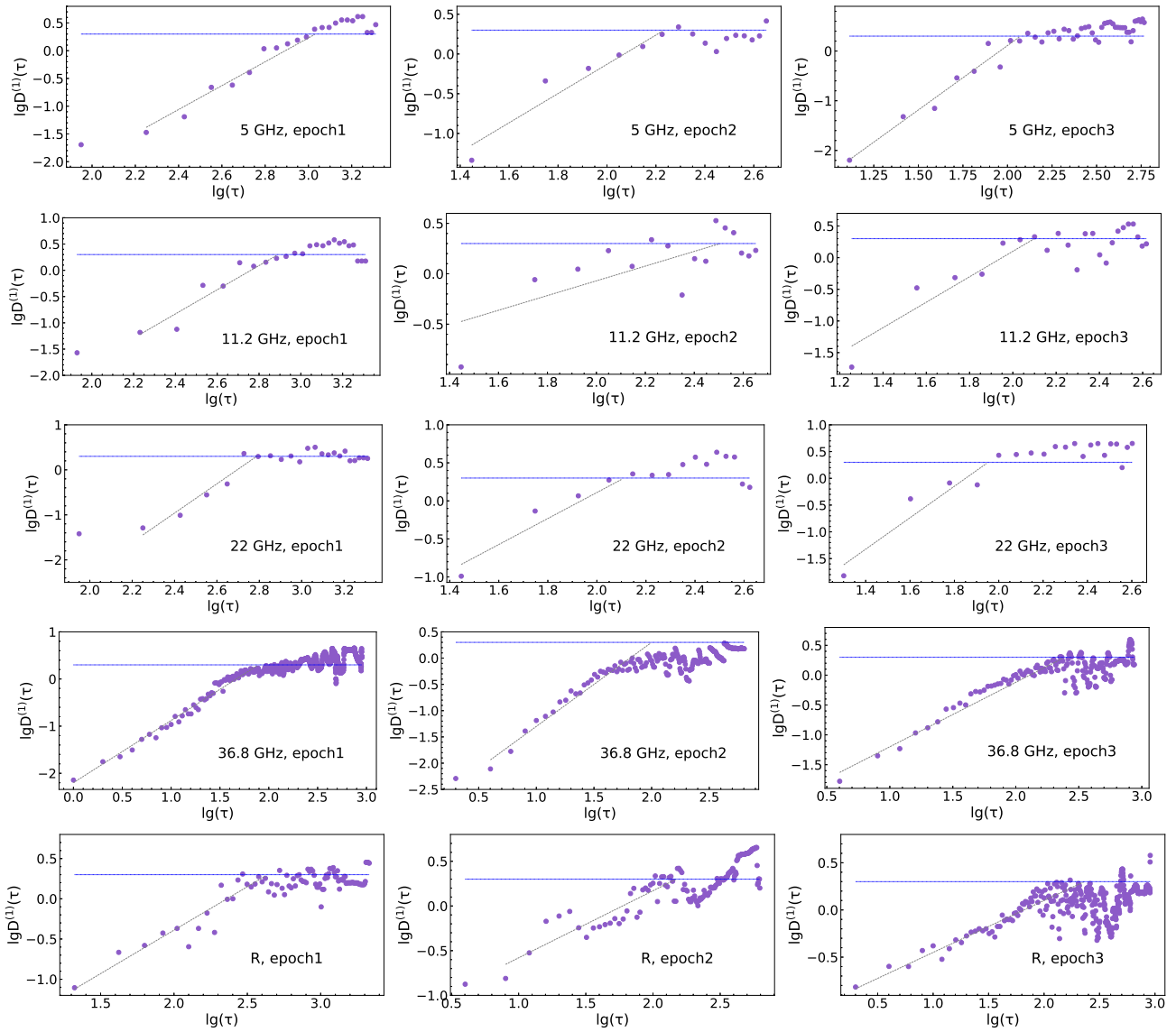


Figure 6. The SF for the total flux variations in the optical and radio bands for the three epochs.

9 RADIO-OPTICAL CORRELATION

We used the cross-correlation method to analyze time lags in the light curves at different frequencies. (Edelson & Krolik 1988). To calculate a discrete correlation function (DCF) of irregularly sampled time series, the software package described in Robertson et al. (2015) was used, and to find out the confidence levels of the cross-correlation function the Monte Carlo simulations were applied (Emmanoulopoulos et al. 2013).

9.1 Cross correlation function of irregularly sampled time series

Cross-correlation function (CCF) analysis is a common method to analyse multi-frequency light curves observed over the same period of time. The observations in most cases lead to irregularly sampled light curves. In order to determine time lags between frequencies, a discrete correlation function (DCF) for irregularly sampled time series is used (Edelson & Krolik 1988):

$$R_{12}(\tau) = \frac{1}{M} \sum_{ij} \frac{[f_1(i) - \mu_1][f_2(j) - \mu_2]}{\sqrt{(\sigma_1^2 - e_1^2)(\sigma_2^2 - e_2^2)}}, \quad (13)$$

where τ is a transform time (lag), $f_1(i)$ and $f_2(j)$ are the values of the original data series, for which $\Delta t_{ij} = t_j - t_i$ satisfy the condition $\tau - \Delta\tau/2 \leq \Delta t_{ij} < \tau + \Delta\tau/2$, M is a number of data pairs that fall within the particular interval $\Delta\tau$, μ_1 and μ_2 are the averages for two different data samples, σ_1 and σ_2 are their standard deviations, e_1 and e_2 are the uncertainties of the measurements.

The lag bin width $\Delta\tau$ is basically served as a resolution of the DCF. Its choice is a trade-off between the resolution itself and the stability of DCF calculation. For strongly irregular time series with big gaps that we have in the case of blazar observations, the optimal bin width is around 30 days.

To calculate the DCF of irregularly sampled data we used the software package *pydcf*⁶ (Robertson et al. 2015). The package was converted into a *Python 3* module, and was used in a *Jupyter Notebook* script to calculate the DCFs for an ensemble of simulated light curve pairs (see 9.2).

9.2 A confidence level calculation for the cross correlation function

In the CCF/DCF analysis an estimation of the confidence levels is usually done by the Monte-Carlo simulations. In this process a large number of the artificial light curve pairs is generated, having the same statistical properties (power spectrum density, probability density function) as in the observed data sets. Finding the cross correlation functions for the ensemble of the paired artificial light curves shows the probability of getting a given CCF value purely by coincidence.

In this paper we used the software tool *DELIGHTcurveSimulation*⁷ (Emmanoulopoulos et al. 2013) to model the artificial light curves. Our data for all frequency bands including RATAN-600 and third-party data were pre-processed in advance, which included the

interpolation of the irregularly sampled light curves with a step of one day using the Steffen spline interpolation (Steffen 1990). A *Jupyter Notebook* script was written for the artificial light curve modelling, and for the DCF calculation only the observed dates were chosen. Simulation of 5000–10000 light curves containing up to 10000 samples for each frequency band can be done relatively fast using a personal computer.

9.3 Cross-correlation analysis of the S4 J0954+658 light curves

In order to find the time lags between the optical and radio light curves, cross-correlation functions were calculated using the approach described in the sections above for the full time interval 2003–2023 and for the chosen epochs 1, 2, and 3. The cross-correlation functions between the mean-subtracted light curves at different frequencies (optical, 5 GHz, and 36.8 GHz) for epochs 1 to 3 and for the entire observing period 2003–2023 are shown in Figs 7–10. The resulting time lags with the maximum DCF values for epochs 1 to 3 are listed in Table 11. We consider the case of a significance level of 2σ and greater.

Comparison of different light curves is not quite easy due to different data sampling in the radio and optical ranges and the presence of gaps in the measurements. Therefore we used 30-day time lag intervals for the analysis of the light curves over the entire period under study as well as for epochs 1–3 at 5 GHz, while for the optical and 36.8 GHz data over epochs 1–3, 10-day time lag intervals were more acceptable, as these epochs have better cadence, up to 3–5 days.

Analysis of the cross-correlation over the total time interval allow us to make some preliminary conclusions. The most evident result is obtained for the cross-correlation between the radio light curves (top panel in Fig. 7). As we can see, the maximum peak with a significance of about 1.75σ is located at a time lag of $60^d \pm 5^d$. The cross-correlation over individual epochs (Fig. 8) gives peaks close to the same position (of course, we should exclude the highest peak at a lag of -400^d for epoch 2 as non-physical). For epoch 3 with the best data sampling, the significance of the peak is about 3σ . Thus, we can conclude that there exists a delay of about 60 days between the 5 GHz and 36.8 GHz light curves, and an increase of the flux density at higher frequencies precedes that at the lower ones.

Analysis of the cross-correlation between the radio and optical data is more complex due to the presence of many fast optical flares, as it was noted earlier in 7.1. Here we take into consideration only preceding optical flares, therefore only the right parts of the CCFs with positive lags are analyzed. Evidently, the local maxima at $\sim -200^d$ and $\sim -230^d$ (the center and bottom panels in Fig. 7, 5 GHz, and 36.8 GHz) correspond to correlation of radio flares with much earlier optical flares not related to their true counterparts. Thus, the real correlations between the radio and optical events estimated from the total ranges may be presented by wide humps in the range between 0^d and 200^d with CCF values of about 0.4 for both ranges: 5 GHz and 36.8 GHz.

We can expect that the correlation between the optical and radio light curves should be more evident for the second and third epochs, where our data are presented with the best cadence and in the absence of serious gaps. These reasons

⁶ <https://github.com/astronomerdamo/pydcf>

⁷ <https://github.com/samconnolly/DELIGHTcurveSimulation/>

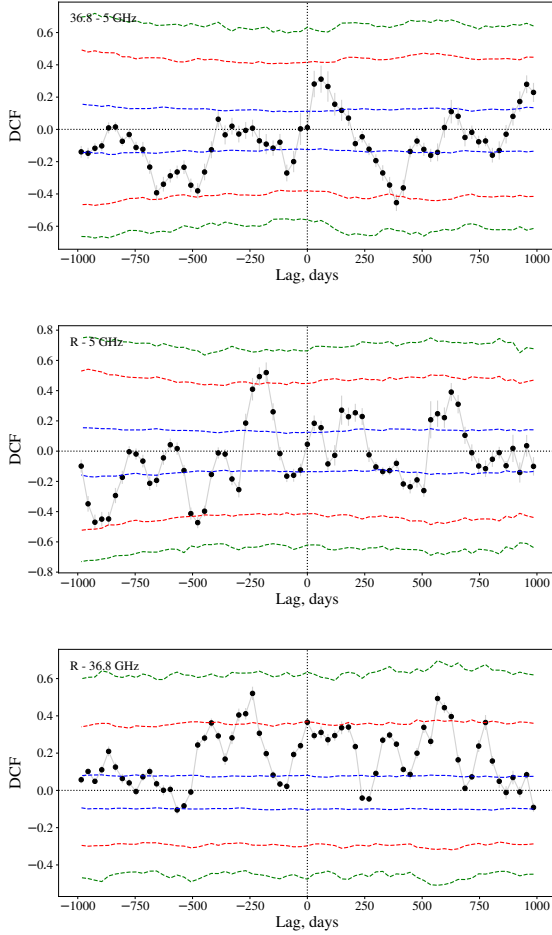


Figure 7. Cross-correlation functions over the entire observing period with a time lag resolution of 30 days. Top panel: between the 36.8 GHz and 5 GHz light curves, center panel: between the optical-range and 5 GHz data, bottom panel: between the optical-range and 36.8 GHz data. The confidence intervals of 1, 2, and 3σ are shown with the dashed lines (blue, red and green respectively).

allowed us to increase the signal-to-noise ratio in the resulting CCF (confidence exceeds 2σ at CCF values of about 0.5 and higher, see Fig.9 and Fig.10), but the inter-range delay may still be varying from 0 to 200 days.

Due to the confusion between neighboring fast flares, it is difficult to localize the matching flares in different spectral ranges. Rather, we can identify slow flares in the radio range with groups of fast optical flares with a total duration of about 200^d , as it was noted in 7.1.

We suggest that the data for epoch 1 show a time lag between the optical and radio 36.8 GHz ranges of about 70^d , and the data for epoch 2 give local maxima at delays of 5^d , 200^d , and 400^d . Epoch 3, which includes many powerful short flares in the R band, produces two wide humps: the first one is around the zero time lag with CCF values of about 0.5 (the mean position is 30 ± 20^d), and the second one is located at a lag of about 160 ± 30^d .

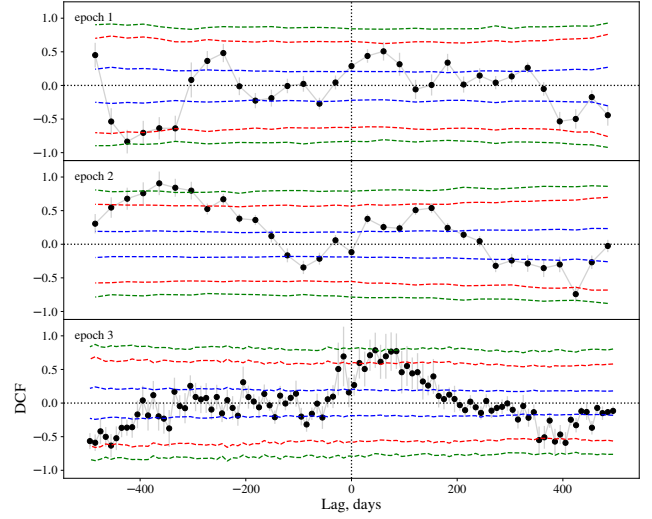


Figure 8. Cross-correlation functions between the 36.8 GHz and 5 GHz light curves with a time lag resolution of 30 days for epochs 1 (top) and 2 (middle) and 10 days for epoch 3 (bottom). The confidence intervals of 1, 2, and 3σ are shown with the dashed lines, as on Fig.7.

9.4 Correlation of optical flares with γ photons

In this subsection we will try to find some connection between the set of optical flares and the γ -ray flux in range 0.1-100 GeV of S4 0954+658 over the last 1000 days (period MJD=59150 – 60150). The data from the Fermi satellite Large Area Telescope (LAT) (Atwood et al. (2009)) with the shortest 3-day binning can be taken from the Fermi LAT Light Curve Repository (Abdollahi et al. (2023)). The binning of the Fermi light curve is well suited to the typical interval in our night-averaged optical data.

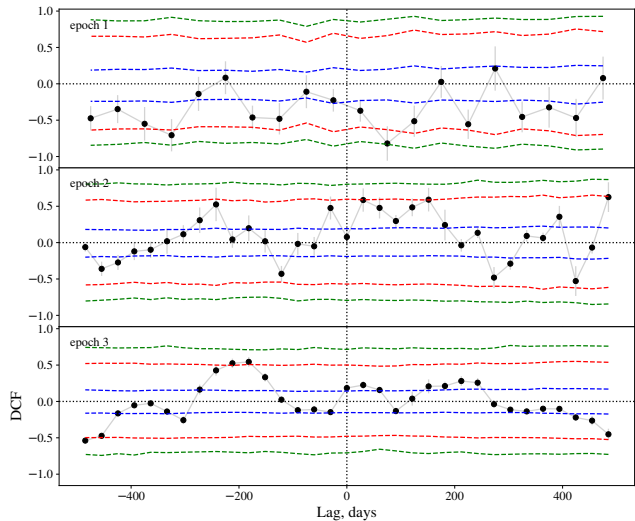
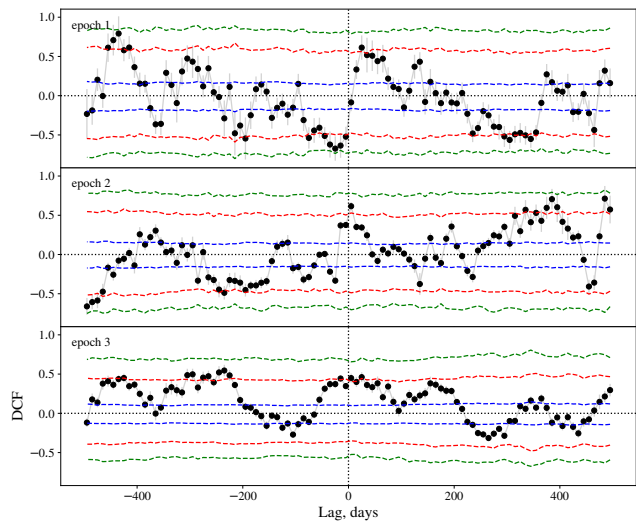
For clarity, we plotted both light curves for the R band and γ -flux in one graph (Fig.11). The original Fermi data, expressed in photons per second per square centimeter, were multiplied by a factor of 30000. Even visual inspection of the optical and γ -ray fluxes shows generally good agreement with the exception of only a few fast optical flares on MJD \sim 59200–59260, 59500–59550, 59650–59680 and during a quite long interval between MJD = 59800–59900. Within these epochs γ -emission was in the quiescent state or demonstrated faint events (below 1 in an adopted units or $3\text{--}5 \cdot 10^{-8}$ photons per second per square centimeter).

The inverse situation is not true: we could not find any γ -ray flare without an optical counterpart within a 1–2 day interval.

We studied the gamma–optical correlation with the DCF calculated in the manner as described above. The result is shown in Fig. 12, where the optical and γ -ray data have preliminary been averaged over 5^d intervals and the DCF calculated over the same bins within the MJD range between 59150 and 60150. The main peak with $r \sim 0.68$ indicates a fairly strong correlation at an almost zero-time delay (the peak position is 2.5 ± 2^d). This is in good agreement with

Table 11. Time lags with the maximum DCF values for the light curve pairs 36.8 GHz–5 GHz, R band–5 GHz, and R band–36.8 GHz.

Frequency pair	τ , days	DCF level	τ , days	DCF level	τ , days	DCF level
epoch 1			epoch 2		epoch 3	
R-band - 5 GHz	275 ± 25	0.21	250 ± 30	0.60	210 ± 20	0.25
36.8 GHz - 5 GHz	60 ± 15	0.51	130 ± 20	0.50	55 ± 10	0.79
R band - 36.8 GHz	45 ± 5	0.79	380 ± 10	0.70	25 ± 5	0.55

**Figure 9.** Cross-correlation functions between the R band and 5 GHz light curves with a time lag resolution of 50 days for epoch 1 (top) and 30 days for epochs 2 and 3 (bottom). The confidence intervals of 1, 2, and 3σ are shown with the dashed lines, as on Fig.7.**Figure 10.** Cross-correlation functions between the R band and 36.8 GHz light curves with a time lag resolution of 10 days for the epochs from 1 (top) to 3 (bottom). The confidence intervals of 1, 2, and 3σ are shown with the dashed lines, as on Fig.7.

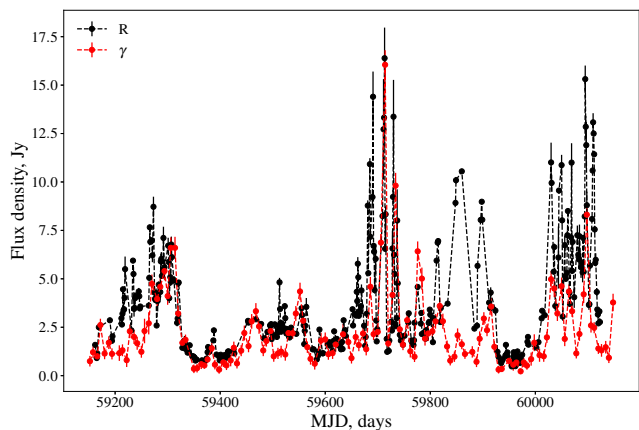
the hypothesis about the common origin of optical photons and hard γ -rays.

10 SUMMARY AND DISCUSSION

During a long time period of 2003–2023, S4 0954+658 has been showing extremely high broadband activity with amplitude of flux density variation up to 70–100% in the optical and radio domains. The high optical activity is accompanied by a series of bright radio flares, the amplitude and frequency of which have strongly increased in 2022–2023. During the high radio state period in S4 0954+658, we detect multiple radio flares of various amplitude and duration. The large radio flares last on average from 0.3 to 1 year at 22–36.7 GHz and slightly longer at 5–11.2 GHz. The optical flares consist of 2 types: the slower low-amplitude ones with characteristic time of about 50 days and the faster ones which are shorter and last 7–20 days.

The time structure of non-stationary emission shows that the characteristic time scale τ of the variable process at 5–22 GHz is about 100 days for epochs 2 and 3 and about 1000 days for the relatively low-active state during epoch 1.

The optical and radio 36.8 GHz variations correlate at de-

**Figure 11.** Optical and γ fluxes of S4 0965+658 over period MJD=59150–60150.

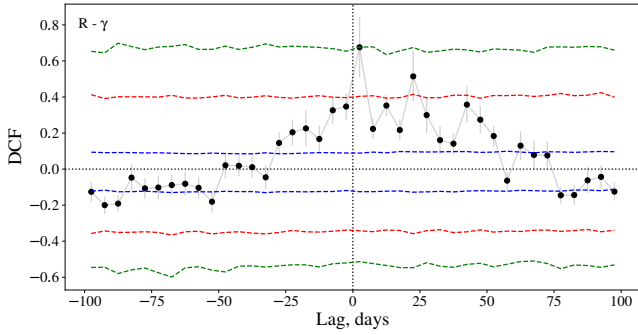


Figure 12. Cross-correlation between optical (R band) and γ fluxes of S4 0965+658 over period MJD=59150–60150. All data were binned with 5^d window.

lays in the interval of 25–200 days. This indicates co-spatiality of the radio and optical emission region, we can observe the same photon population from different emission area (Larionov et al. 2020). The linear size of this region can be estimated as

$$R < c \cdot t_{\text{obs}} \cdot \delta / (1 + z), \quad (14)$$

where c is the speed of light, t_{obs} is the time delay, δ is the Doppler factor, which lies in the range of $6.1 < \delta < 35$ (Kishore et al. 2023) for the source. The upper limit of the linear size for $t_{\text{obs}} = 100$ is 0.4 pc, the lower limit is 2 pc.

The DCF between the γ -ray and optical (R band) light curves over the entire period shows a main peak compatible with a zero-time lag ($2^d.5$).

Since the detection of ultra-high energy neutrino events (IceCube Collaboration et al. 2018), AGNs have become intriguing candidates for high-energy neutrino sources and effective proton accelerators (Kovalev et al. 2020b, 2022). The sources of these neutrinos are still unknown, but it turned out that the sky areas where the ultra-high-energy neutrinos come from are statistically associated with VLBI-bright quasar positions, and the time of their arrival coincide with powerful flares of synchrotron emission in the compact jets of these objects (Plavin et al. 2020, 2021). We have considered the broadband radio spectra of S4 0954+658 using both electrons and protons as emitting particles and showed that the spectra can be well explained by each particle type. The estimated parameters B_{\perp} and Θ are in good agreement with those which are generally accepted in the current theories. The estimated brightness temperature T_b for S4 0954+658 does not exceed the known limit of $\sim 10^{12}$ K for relativistic electrons (Kellermann & Pauliny-Toth 1969; Readhead 1994) and $\sim 10^{15}$ K for relativistic protons (Kardashev 2000; Kovalev et al. 2022). The discovered excess of the 10^{12} K limit in the RadioAstron space experiment (Kovalev et al. 2020a) for many AGNs could be explained both by the Doppler boosting through the bulk motion of emitting plasma (for a part of such objects) and by relativistic proton emission (for all such sources).

ACKNOWLEDGEMENTS

The reported study was funded by the Ministry of Science and Higher Education of the Russian Federation under contract No. 075-15-2022-1227. YYK was supported by the M2FINDERS project, which has received funding from the European Research Council (ERC) under the European Union’s Horizon 2020 Research and Innovation Programme (grant agreement No. 101018682). LY is supported by the National Natural Science Foundation of China (NSFC) grants No. 12205388. The observations were carried out with the RATAN-600 scientific facility, the Zeiss-1000 and AS-500/2 optical reflectors of SAO RAS, and the RT-22 of CrAO RAS. VAE and VLN are grateful to the staff of the Radio Astronomy Department of CrAO RAS for their participation in the observations. VVV and SOI would like to thank [N. S. Kardashev] and V. S. Bychkova for their involvement into blazar studies and valuable discussions on the topic of blazar variability. The observations at 5.05 and 8.63 GHz was performed with the Badary and Zelenchukskaya radio RT-32 telescopes operated by the Shared Research Facility Center for the Quasar VLBI Network of IAA RAS (<https://iaaras.ru/cu-center/>). This research has made use of the NASA/IPAC Extragalactic Database (NED), which is operated by the Jet Propulsion Laboratory, California Institute of Technology, under contract with the National Aeronautics and Space Administration; the CATS database, available on the Special Astrophysical Observatory website; the SIMBAD database, operated at CDS, Strasbourg, France. This research has made use of the Vizier catalogue access tool, CDS, Strasbourg, France. The development of the Fermi LAT Light Curve Repository has been funded in part through the Fermi Guest Investigator Program (NASA Research Announcements NNH19ZDA001N and NNH20ZDA001N). This study makes use of the VLBA data from the VLBA-BU Blazar Monitoring Program (BEAM-ME and VLBA-BU-BLAZAR; <http://www.bu.edu/blazars/BEAM-ME.html>), funded by NASA through the Fermi Guest Investigator Program. The VLBA is an instrument of the National Radio Astronomy Observatory. The National Radio Astronomy Observatory is a facility of the National Science Foundation operated by Associated Universities, Inc.

REFERENCES

- Abdo A. A., Ackermann M., Agudo I., Ajello M., Aller H. D., Aller M. F., Angelakis E., Arkharov A. A., 2010, *ApJ*, **716**, 30
 Abdollahi S., et al., 2023, *ApJS*, **265**, 31
 Acero F., et al., 2015, *ApJS*, **218**, 23
 Aller H. D., Aller M. F., Latimer G. E., Hodge P. E., 1985, *ApJS*, **59**, 513
 Aller M. F., Aller H. D., Hughes P. A., 1992, *ApJ*, **399**, 16
 Angelakis E., et al., 2019, *A&A*, **626**, A60
 Atwood W. B., et al., 2009, *ApJ*, **697**, 1071
 Baars J. W. M., Genzel R., Pauliny-Toth I. I. K., Witzel A., 1977, *A&A*, **61**, 99
 Becerra González J., Acosta-Pulido J. A., Boschin W., Clavero R., Otero-Santos J., Carballo-Bello J. A., Domínguez-Palmero L., 2021, *MNRAS*, **504**, 5258
 Becker R. H., White R. L., Edwards A. L., 1991, *ApJS*, **75**, 1
 Becker R. H., White R. L., Helfand D. J., 1994, in Crabtree D. R., Hanisch R. J., Barnes J., eds, *Astronomical Society of the Pa-*

- cific Conference Series Vol. 61, *Astronomical Data Analysis Software and Systems III*. p. 165
- Bhatta G., 2021, *ApJ*, **923**, 7
- Bhatta G., et al., 2023, *MNRAS*, **520**, 2633
- Böttcher M., 2007, *Ap&SS*, **309**, 95
- Cassaro P., Stanghellini C., Dallacasa D., Bondi M., Zappalà R. A., 2002, *A&A*, **381**, 378
- Cohen A. M., Porcas R. W., Browne I. W. A., Daintree E. J., Walsh D., 1977, *Mem. RAS*, **84**, 1
- Condon J. J., Yin Q. F., 2001, *PASP*, **113**, 362
- Condon J. J., Cotton W. D., Greisen E. W., Yin Q. F., Perley R. A., Taylor G. B., Broderick J. J., 1998, *AJ*, **115**, 1693
- Douglas J. N., Bash F. N., Bozyan F. A., Torrence G. W., Wolfe C., 1996, *AJ*, **111**, 1945
- Edelson R. A., Krolik J. H., 1988, *ApJ*, **333**, 646
- Emmanoulopoulos D., McHardy I. M., Papadakis I. E., 2013, *MNRAS*, **433**, 907
- Fossati G., Maraschi L., Celotti A., Comastri A., Ghisellini G., 1998, *MNRAS*, **299**, 433
- Gabuzda D. C., Cawthorne T. V., 1996, *MNRAS*, **283**, 759
- Gabuzda D. C., Cawthorne T. V., Roberts D. H., Wardle J. F. C., 1992, *ApJ*, **388**, 40
- Gabuzda D. C., Mullan C. M., Cawthorne T. V., Wardle J. F. C., Roberts D. H., 1994, *ApJ*, **435**, 140
- Gabuzda D. C., Kochenov P. Y., Kollgaard R. I., Cawthorne T. V., 2000, *MNRAS*, **315**, 229
- Gaur H., et al., 2012, *MNRAS*, **425**, 3002
- Ghisellini G., Tavecchio F., Foschini L., Ghirlanda G., 2011, *MNRAS*, **414**, 2674
- Gopal-Krishna Sagar R., Wiita P. J., 1993, *MNRAS*, **262**, 963
- Gregory P. C., Condon J. J., 1991, *ApJS*, **75**, 1011
- Gregory P. C., Scott W. K., Douglas K., Condon J. J., 1996, *ApJS*, **103**, 427
- Gu M., Ai Y. L., 2011, *Journal of Astrophysics and Astronomy*, **32**, 87
- Gu M. F., Lee C. U., Pak S., Yim H. S., Fletcher A. B., 2006, *A&A*, **450**, 39
- Gupta A. C., Banerjee D. P. K., Ashok N. M., Joshi U. C., 2004, *A&A*, **422**, 505
- Gupta A. C., et al., 2017, *MNRAS*, **472**, 788
- Hagen-Thorn V. A., et al., 2015, *Astronomy Reports*, **59**, 551
- Hales S. E. G., Masson C. R., Warner P. J., Baldwin J. E., 1990, *MNRAS*, **246**, 256
- Healey S. E., Romani R. W., Taylor G. B., Sadler E. M., Ricci R., Murphy T., Ulvestad J. S., Winn J. N., 2007, *ApJS*, **171**, 61
- Heidt J., Wagner S. J., 1996, *A&A*, **305**, 42
- Hervet O., Boisson C., Sol H., 2016, *A&A*, **592**, A22
- Hovatta T., Valtaoja E., Tornikoski M., Lähteenmäki A., 2009, *A&A*, **494**, 527
- Hufnagel B. R., Bregman J. N., 1992, *ApJ*, **386**, 473
- Hughes P. A., Aller H. D., Aller M. F., 1992, *ApJ*, **396**, 469
- Hurley-Walker N., et al., 2017, *MNRAS*, **464**, 1146
- IceCube Collaboration et al., 2018, *Science*, **361**, eaat1378
- Intema H. T., Jagannathan P., Mooley K. P., Frail D. A., 2017, *A&A*, **598**, A78
- Isler J. C., Urry C. M., Coppi P., Bailyn C., Brady M., MacPherson E., Buxton M., Hasan I., 2017, *ApJ*, **844**, 107
- Jenness T., Robson E. I., Stevens J. A., 2010, *MNRAS*, **401**, 1240
- Johnston K. J., et al., 1995, *AJ*, **110**, 880
- Jorstad S. G., et al., 2017, *ApJ*, **846**, 98
- Kardashev N. S., 2000, *Astronomy Reports*, **44**, 719
- Kellermann K. I., Owen F. N., 1988, in Kellermann K. I., Verschuur G. L., eds., *Galactic and Extragalactic Radio Astronomy*. pp 563–602
- Kellermann K. I., Pauliny-Toth I. I. K., 1969, *ApJ*, **155**, L71
- Kharinov M. A., Yablokova A. E., 2012, *Tr. IPA RAN*, pp 342–347
- Kishore S., Gupta A. C., Wiita P. J., 2023, *ApJ*, **943**, 53
- Kollgaard R. I., Wardle J. F. C., Roberts D. H., Gabuzda D. C., 1992, *AJ*, **104**, 1687
- Kovalev Y. Y., Nizhelsky N. A., Kovalev Y. A., Berlin A. B., Zhekanis G. V., Mingaliev M. G., Bogdantsov A. V., 1999, *A&AS*, **139**, 545
- Kovalev Y. A., Kovalev Y. Y., Nizhelsky N. A., 2000, *PASJ*, **52**, 1027
- Kovalev Y. Y., et al., 2020a, *Advances in Space Research*, **65**, 705
- Kovalev Y. A., et al., 2020b, *Advances in Space Research*, **65**, 745
- Kovalev Y. A., et al., 2022, in *The Multifaceted Universe: Theory and Observations - 2022*. p. 27
- Kraus A., et al., 2003, *A&A*, **401**, 161
- Kudryavtseva N., Gabuzda D., Mahmud M., O'Sullivan S., 2010, in *10th European VLBI Network Symposium and EVN Users Meeting: VLBI and the New Generation of Radio Arrays*. p. 45, doi:10.22323/1.125.0045
- Lacy M., et al., 2020, *PASP*, **132**, 035001
- Lähteenmäki A., Valtaoja E., 1999, *ApJ*, **521**, 493
- Larionov V. M., et al., 2020, *MNRAS*, **492**, 3829
- Laurent-Muehleisen S. A., Kollgaard R. I., Ryan P. J., Feigelson E. D., Brinkmann W., Siebert J., 1997, *A&AS*, **122**, 235
- Lawrence C. R., Pearson T. J., Readhead A. C. S., Unwin S. C., 1986, *AJ*, **91**, 494
- Lazio T. J. W., Waltman E. B., Ghigo F. D., Fiedler R. L., Foster R. S., Johnston K. J., 2001, *ApJS*, **136**, 265
- Liodakis I., Romani R. W., Filippenko A. V., Kiehlmann S., Max-Moerbeck W., Readhead A. C. S., Zheng W., 2018, *MNRAS*, **480**, 5517
- Liu J., et al., 2018, *Galaxies*, **6**, 49
- MAGIC Collaboration et al., 2018, *A&A*, **617**, A30
- Marcha M. J. M., Browne I. W. A., Impey C. D., Smith P. S., 1996, *MNRAS*, **281**, 425
- Markelov S. V., Murzin V. A., Borisenko A. N., Ivaschenko N. G., Afanasieva I. V., Ardilanov V. I., 2000, *Astronomical and Astrophysical Transactions*, **19**, 579
- Massardi M., et al., 2008, *MNRAS*, **384**, 775
- Massardi M., Bonaldi A., Bonavera L., López-Caniego M., de Zotti G., Ekers R. D., 2011, *MNRAS*, **415**, 1597
- Massaro E., Nesci R., Maesano M., Montagni F., D'Alessio F., 1998, *MNRAS*, **299**, 47
- Mead A. R. G., Ballard K. R., Brand P. W. J. L., Hough J. H., Brindle C., Bailey J. A., 1990, *A&AS*, **83**, 183
- Miller H. R., Carini M. T., Goodrich B. D., 1989, *Nature*, **337**, 627
- Mingaliev M. G., Sotnikova Y. V., Udovitskiy R. Y., Mufakharov T. V., Nieppola E., Erkenov A. K., 2014, *A&A*, **572**, A59
- Mingaliev M., et al., 2017, *Astronomische Nachrichten*, **338**, 700
- Mirzoyan R., 2015, *The Astronomer's Telegram*, **7080**, 1
- Morgan J. S., et al., 2018, *MNRAS*, **473**, 2965
- Morozova D. A., et al., 2014, *AJ*, **148**, 42
- Morozova D., et al., 2016, *Galaxies*, **4**, 24
- Murphy T., et al., 2010, *MNRAS*, **402**, 2403
- Narayan R., 1992, *Philosophical Transactions of the Royal Society of London Series A*, **341**, 151
- Osterman Meyer A., et al., 2008, *AJ*, **136**, 1398
- Osterman Meyer A., Miller H. R., Marshall K., Ryle W. T., Aller H., Aller M., Balonek T., 2009, *AJ*, **138**, 1902
- Ott M., Witzel A., Quirrenbach A., Krichbaum T. P., Standke K. J., Schalinski C. J., Hummel C. A., 1994, *A&A*, **284**, 331
- Owen F. N., Porcas R. W., Mufson S. L., Moffett T. J., 1978, *AJ*, **83**, 685
- Parijskij Y. N., 1993, *IEEE Antennas and Propagation Magazine*, **35**, 7
- Pauliny-Toth I. I. K., Witzel A., Preuss E., Kuehr H., Fomalont E. B., Davis M. M., Kellermann K. I., 1978, *AJ*, **83**, 451
- Perley R. A., 1982, *AJ*, **87**, 859
- Perley R. A., Butler B. J., 2013, *ApJS*, **204**, 19
- Perley R. A., Butler B. J., 2017, *ApJS*, **230**, 7
- Perlman E. S., et al., 2006, in Miller H. R., Marshall K., Webb

- J. R., Aller M. F., eds, *Astronomical Society of the Pacific Conference Series* Vol. 350, *Blazar Variability Workshop II: Entering the GLAST Era*. p. 191
- Pininti V. R., Bhatta G., Paul S., Kumar A., Rajgor A., Barnwal R., Gharat S., 2023, *MNRAS*, **518**, 1459
- Planck Collaboration et al., 2016, *A&A*, **594**, A26
- Plavin A., Kovalev Y. Y., Kovalev Y. A., Troitsky S., 2020, *ApJ*, **894**, 101
- Plavin A. V., Kovalev Y. Y., Kovalev Y. A., Troitsky S. V., 2021, *ApJ*, **908**, 157
- Raiteri C. M., et al., 1999, *A&A*, **352**, 19
- Ramírez A., de Diego J. A., Dultzin-Hacyan D., González-Pérez J. N., 2004, *A&A*, **421**, 83
- Readhead A. C. S., 1994, *ApJ*, **426**, 51
- Rengelink R. B., Tang Y., de Bruyn A. G., Miley G. K., Bremer M. N., Roettgering H. J. A., Bremer M. A. R., 1997, *A&AS*, **124**, 259
- Resconi E., Franco D., Gross A., Costamante L., Flaccomio E., 2009, *A&A*, **502**, 499
- Reuter H. P., et al., 1997, *A&AS*, **122**, 271
- Richards J. L., et al., 2011, *ApJS*, **194**, 29
- Riley J. M. W., Waldrum E. M., Riley J. M., 1999, *MNRAS*, **306**, 31
- Robertson D. R. S., Gallo L. C., Zoghbi A., Fabian A. C., 2015, *MNRAS*, **453**, 3455
- Robson E. I., Stevens J. A., Jenness T., 2001, *MNRAS*, **327**, 751
- Savolainen T., Wiik K., Valtaoja E., Jorstad S. G., Marscher A. P., 2002, *A&A*, **394**, 851
- Seielstad G. A., Pearson T. J., Readhead A. C. S., 1983, *PASP*, **95**, 842
- Simonetti J. H., Cordes J. M., Heeschen D. S., 1985, *ApJ*, **296**, 46
- Sotnikova Y. V., et al., 2022a, *Astrophysical Bulletin*, **77**, 246
- Sotnikova Y., Kovalev Y. A., Kovalev Y. Y., Erkenov A. K., Plavin A. V., 2022b, in *European VLBI Network Mini-Symposium and Users' Meeting 2021*. p. 9, doi:10.22323/1.399.0009
- Sotnikova Y. V., Kovalev Y. A., Ermakov A. N., Volvach L. N., Volvach A. E., 2023, *Astrophysical Bulletin*, **78**, 105
- Steffen M., 1990, *A&A*, **239**, 443
- Steppe H., et al., 1993, *A&AS*, **102**, 611
- Stickel M., Padovani P., Urry C. M., Fried J. W., Kuehr H., 1991, *ApJ*, **374**, 431
- Tabara H., Inoue M., 1980, *A&AS*, **39**, 379
- Teraesranta H., et al., 1998, *A&AS*, **132**, 305
- Thompson D. J., et al., 1995, *ApJS*, **101**, 259
- Tornikoski M., Lainela M., Valtaoja E., 2000, *AJ*, **120**, 2278
- Tsybulev P. G., 2011, *Astrophysical Bulletin*, **66**, 109
- Tsybulev P. G., Nizhelskii N. A., Dugin M. V., Borisov A. N., Kratov D. V., Udovitskii R. Y., 2018, *Astrophysical Bulletin*, **73**, 494
- Udovitskiy R. Y., Sotnikova Y. V., Mingaliev M. G., Tsybulev P. G., Zhekanis G. V., Nizhelskij N. A., 2016, *Astrophysical Bulletin*, **71**, 496
- Ulrich M., Maraschi L., Urry C. M., 1997, *ARA&A*, **35**, 445
- Ulvestad J., Johnston K., Perley R., Fomalont E., 1981, *AJ*, **86**, 1010
- Urry C. M., Padovani P., 1995, *PASP*, **107**, 803
- Vagnetti F., Trevese D., Nesci R., 2003, *ApJ*, **590**, 123
- Valtaoja E., Lähteenmäki A., Teräsraanta H., Lainela M., 1999, *ApJS*, **120**, 95
- Valyavin G., et al., 2022, *Astrophysical Bulletin*, **77**, 551
- Vaughan S., Edelson R., Warwick R. S., Uttley P., 2003, *MNRAS*, **345**, 1271
- Verkhodanov O. V., 1997, *Astronomical Data Analysis Software and Systems VI*, A.S.P. Conference Series, **125**, 46
- Verkhodanov O. V., Trushkin S. A., Andernach H., Chernenkov V. N., 2005, *Bulletin of the Special Astrophysics Observatory*, **58**, 118
- Verkhodanov O. V., Trushkin S. A., Andernach H., Chernenkov V. N., 2009, *Data Science Journal*, **8**, 34
- Villata M., et al., 2002, *A&A*, **390**, 407
- Vlasyuk V. V., 1993, *Bulletin of Special Astrophysical Observatory*, **36**, 107
- Vol'vach A. E., Vol'vach L. N., Kardashev N. S., Larionov M. G., 2008, *Astronomy Reports*, **52**, 429
- Volvach A. E., et al., 2016, *Astronomy Reports*, **60**, 1035
- Wagner S. J., Witzel A., 1995, *ARA&A*, **33**, 163
- Walker M. A., 1998, *MNRAS*, **294**, 307
- Walsh D., Beckers J. M., Carswell R. F., Weymann R. J., 1984, *MNRAS*, **211**, 105
- Wang G., Lu R.-s., Shen Z.-q., Jiang W., Huang L., Zhao S.-s., Yan X., Yuan C., 2023, *Progress in Astronomy*, **41**, 257
- Wrobel J. M., Patnaik A. R., Browne I. W. A., Wilkinson P. N., 1998, in *American Astronomical Society Meeting Abstracts*. p. 40.04
- Zhang X., Zheng Y., Chen H., Wang S., Cao A., Peng B., Nan R., 1997, *A&AS*, **121**, 59
- von Montigny C., et al., 1995, *ApJ*, **440**, 525

APPENDIX A: OPTICAL AND RADIO MEASUREMENTS

Table A1: The R-band measurements of S4 0954+658 in 2003–2023: epoch MJD (Col. 1), epoch yyyy.mm.dd (Col. 2), number of observations N_{obs} (Col. 3), the flux densities in R filter and their errors, mJy (Col. 4).

MJD epoch 1	yyyy.mm.dd 2	N_{obs} 3	R_{flux} , mJy, σ_R , mJy 4
52678	2003.02.07	1	1.24 ± 0.02
52679	2003.02.08	3	1.39 ± 0.03
52699	2003.02.28	2	1.12 ± 0.01
52701	2003.03.02	4	1.56 ± 0.09
52702	2003.03.03	8	1.31 ± 0.03
52705	2003.03.06	10	2.02 ± 0.06
52727	2003.03.28	2	1.45 ± 0.01
52730	2003.03.31	1	1.58 ± 0.05
52731	2003.04.01	3	1.41 ± 0.02
52753	2003.04.23	2	0.86 ± 0.01
52758	2003.04.28	3	0.79 ± 0.01
52761	2003.05.01	11	0.68 ± 0.03
52762	2003.05.02	10	0.58 ± 0.01
52763	2003.05.03	5	0.60 ± 0.01
52782	2003.05.22	4	0.72 ± 0.03
52783	2003.05.23	4	0.78 ± 0.02
52785	2003.05.25	3	0.81 ± 0.01
52796	2003.06.05	12	0.75 ± 0.04
52812	2003.06.26	1	0.53 ± 0.03
52968	2003.11.24	3	1.19 ± 0.01
52996	2003.12.22	3	0.61 ± 0.01
53002	2003.12.28	3	0.66 ± 0.01
53003	2003.12.29	4	0.63 ± 0.01
53032	2004.01.27	3	0.72 ± 0.01
53034	2004.01.29	3	0.81 ± 0.01
53062	2004.02.26	3	0.75 ± 0.01
53083	2004.03.18	4	1.03 ± 0.01
53089	2004.03.24	3	0.86 ± 0.01
53117	2004.04.21	1	1.69 ± 0.04
53118	2004.04.22	3	1.64 ± 0.01
53122	2004.04.26	3	2.07 ± 0.01
53146	2004.05.20	3	1.27 ± 0.01
53174	2004.06.17	3	1.05 ± 0.02
53348	2004.12.08	6	0.91 ± 0.02
53387	2005.01.16	2	0.96 ± 0.01
53388	2005.01.17	3	0.99 ± 0.01
53404	2005.02.02	2	1.28 ± 0.01
53406	2005.02.04	3	1.18 ± 0.01
53407	2005.02.05	3	1.00 ± 0.01
53411	2005.02.09	3	1.06 ± 0.01
53412	2005.02.10	3	1.34 ± 0.01
53444	2005.03.14	3	0.55 ± 0.01
53466	2005.04.05	3	0.37 ± 0.01
53471	2005.04.10	2	0.26 ± 0.01
53529	2005.06.07	3	0.70 ± 0.01
53670	2005.10.26	3	0.37 ± 0.02
53698	2005.11.23	3	0.38 ± 0.01
53705	2005.11.30	3	0.51 ± 0.01
53730	2005.12.25	5	0.78 ± 0.01
53735	2005.12.30	8	0.75 ± 0.01
53822	2006.03.27	5	1.00 ± 0.01
53830	2006.04.04	5	1.42 ± 0.01
53881	2006.05.25	4	0.63 ± 0.01
53888	2006.06.01	3	1.20 ± 0.01
54086	2006.12.16	5	0.64 ± 0.01
54087	2006.12.16	5	0.64 ± 0.01
54088	2006.12.17	5	0.59 ± 0.01
54145	2007.02.13	6	0.40 ± 0.01
54150	2007.02.19	5	0.41 ± 0.01
54170	2007.03.10	5	0.62 ± 0.01
54473	2008.01.07	5	0.93 ± 0.01
54500	2008.02.04	6	0.79 ± 0.01

Table A1: continued.

MJD epoch 1	yyyy.mm.dd 2	N_{obs} 3	R_{flux} , mJy, σ_R , mJy 4
54509	2008.02.12	3	0.72 ± 0.01
54557	2008.03.31	3	1.28 ± 0.01
54798	2008.11.26	5	0.38 ± 0.01
54805	2008.12.03	5	0.37 ± 0.01
54853	2009.01.21	8	0.45 ± 0.01
54857	2009.01.24	4	0.51 ± 0.01
54912	2009.03.21	17	0.62 ± 0.01
54920	2009.03.29	5	0.53 ± 0.01
55189	2009.12.23	3	0.89 ± 0.01
55241	2010.02.13	5	0.46 ± 0.01
55247	2010.02.19	5	0.36 ± 0.01
55274	2010.03.18	3	0.73 ± 0.01
55293	2010.04.06	5	1.22 ± 0.01
55297	2010.04.10	5	0.78 ± 0.01
55592	2011.01.30	4	0.47 ± 0.01
55646	2011.03.30	2	1.50 ± 0.02
55652	2011.03.31	5	1.39 ± 0.01
55655	2011.04.03	5	1.20 ± 0.01
55925	2011.12.28	5	0.53 ± 0.01
55951	2012.01.24	5	1.25 ± 0.02
55953	2012.01.26	6	0.42 ± 0.01
56006	2012.03.19	3	0.51 ± 0.01
56043	2012.04.25	3	0.67 ± 0.01
56278	2012.12.16	3	0.44 ± 0.01
56335	2013.02.11	3	0.39 ± 0.01
56338	2013.02.14	16	0.44 ± 0.01
56358	2013.03.06	8	0.67 ± 0.01
56423	2013.05.10	9	0.45 ± 0.01
56631	2013.12.04	3	0.32 ± 0.01
56652	2013.12.25	3	0.35 ± 0.01
56659	2014.01.01	12	0.45 ± 0.01
56662	2014.01.04	3	0.48 ± 0.01
56691	2014.02.02	3	0.34 ± 0.01
56692	2014.02.03	3	0.35 ± 0.01
56713	2014.02.24	5	0.38 ± 0.01
56717	2014.02.28	3	0.40 ± 0.01
56722	2014.03.05	3	0.40 ± 0.01
56748	2014.03.31	6	0.38 ± 0.01
56981	2014.11.19	3	0.71 ± 0.01
56982	2014.11.20	4	0.63 ± 0.01
57038	2015.01.15	3	1.46 ± 0.01
57043	2015.01.20	3	0.90 ± 0.01
57064	2015.02.10	2	7.99 ± 0.02
57066	2015.02.12	4	14.26 ± 0.50
57067	2015.02.13	7	11.52 ± 0.72
57068	2015.02.14	12	5.04 ± 0.33
57069	2015.02.15	3	8.90 ± 0.31
57071	2015.02.17	10	8.94 ± 0.38
57072	2015.02.18	9	6.21 ± 0.25
57073	2015.02.19	1	7.59 ± 0.01
57075	2015.02.21	7	3.03 ± 0.25
57076	2015.02.22	9	2.82 ± 0.20
57077	2015.02.23	10	3.95 ± 0.56
57078	2015.02.24	26	4.10 ± 0.23
57089	2015.03.07	18	4.40 ± 0.18
57090	2015.03.08	21	1.98 ± 0.04
57091	2015.03.09	3	1.59 ± 0.02
57092	2015.03.10	9	1.61 ± 0.02
57093	2015.03.11	7	2.66 ± 0.05
57095	2015.03.13	3	1.31 ± 0.01
57096	2015.03.14	3	1.78 ± 0.03
57097	2015.03.15	11	1.10 ± 0.02
57100	2015.03.18	3	0.84 ± 0.01
57101	2015.03.19	2	0.83 ± 0.01

Table A1: continued.

MJD epoch 1	yyyy.mm.dd 2	N_{obs} 3	R_{flux} , mJy, σ_R , mJy 4
57103	2015.03.21	5	1.43 ± 0.06
57104	2015.03.22	4	0.89 ± 0.03
57105	2015.03.23	2	0.94 ± 0.01
57106	2015.03.24	13	0.90 ± 0.03
57127	2015.04.14	2	1.04 ± 0.02
57129	2015.04.16	9	0.77 ± 0.01
57133	2015.04.20	2	0.66 ± 0.01
57135	2015.04.22	1	0.96 ± 0.01
57136	2015.04.23	1	0.88 ± 0.01
57149	2015.05.06	1	0.71 ± 0.01
57158	2015.05.15	3	0.70 ± 0.01
57160	2015.05.17	3	0.74 ± 0.01
57161	2015.05.18	3	0.65 ± 0.01
57162	2015.05.18	1	0.77 ± 0.01
57163	2015.05.20	2	0.70 ± 0.01
57182	2015.06.08	2	1.62 ± 0.01
57183	2015.06.09	3	1.77 ± 0.02
57187	2015.06.13	3	4.24 ± 0.03
57223	2015.07.19	2	1.25 ± 0.04
57242	2015.08.07	2	1.15 ± 0.01
57245	2015.08.10	2	0.72 ± 0.01
57250	2015.08.15	2	0.65 ± 0.01
57251	2015.08.16	2	0.66 ± 0.01
57258	2015.08.23	2	0.62 ± 0.01
57368	2015.12.11	3	5.50 ± 0.05
57399	2016.01.11	9	3.47 ± 0.13
57434	2016.02.15	20	2.44 ± 0.13
57437	2016.02.18	17	4.28 ± 0.18
57452	2016.03.04	15	2.63 ± 0.06
57454	2016.03.06	7	2.17 ± 0.18
57455	2016.03.07	3	1.74 ± 0.03
57459	2016.03.11	3	1.96 ± 0.05
57460	2016.03.12	4	1.12 ± 0.02
57464	2016.03.16	2	1.41 ± 0.03
57483	2016.03.17	1	1.45 ± 0.01
57484	2016.04.05	3	1.98 ± 0.01
57490	2016.04.11	3	1.87 ± 0.01
57491	2016.04.12	3	1.59 ± 0.01
57525	2016.05.16	3	1.28 ± 0.01
57526	2016.05.17	4	1.36 ± 0.01
57528	2016.05.19	3	1.38 ± 0.02
57543	2016.06.03	3	0.56 ± 0.01
57550	2016.06.10	3	1.11 ± 0.02
57558	2016.06.18	2	1.25 ± 0.01
57695	2016.11.02	2	0.63 ± 0.02
57710	2016.11.17	2	1.44 ± 0.01
57712	2016.11.19	3	1.43 ± 0.01
57713	2016.11.20	3	1.47 ± 0.01
57719	2016.11.26	2	1.28 ± 0.02
57720	2016.11.27	2	1.20 ± 0.01
57749	2016.12.26	3	1.06 ± 0.01
57764	2017.01.10	3	0.83 ± 0.01
57784	2017.01.30	3	1.74 ± 0.02
57785	2017.01.31	2	1.22 ± 0.01
57811	2017.02.26	3	1.64 ± 0.03
57813	2017.02.28	2	1.61 ± 0.01
57830	2017.03.17	4	3.09 ± 0.02
57833	2017.03.20	1	1.59 ± 0.01
57843	2017.03.30	3	0.63 ± 0.01
57844	2017.03.31	3	0.44 ± 0.01
57860	2017.04.16	3	0.54 ± 0.01
57861	2017.04.17	3	0.63 ± 0.01
57862	2017.04.18	3	0.57 ± 0.01
57886	2017.05.12	3	0.51 ± 0.01

Table A1: continued.

MJD epoch 1	yyyy.mm.dd 2	N_{obs} 3	R_{flux} , mJy, σ_R , mJy 4
57899	2017.05.25	1	0.67 ± 0.01
57900	2017.05.26	2	0.52 ± 0.01
57901	2017.05.27	2	0.52 ± 0.01
58075	2017.11.17	2	1.11 ± 0.01
58077	2017.11.19	2	1.30 ± 0.01
58079	2017.11.20	2	1.15 ± 0.02
58096	2017.12.08	2	1.12 ± 0.02
58100	2017.12.12	2	1.83 ± 0.01
58107	2017.12.19	2	0.84 ± 0.01
58116	2017.12.28	2	1.13 ± 0.01
58121	2018.01.02	4	1.33 ± 0.04
58124	2018.01.05	2	0.99 ± 0.01
58125	2018.01.06	2	0.79 ± 0.01
58134	2018.01.15	1	0.89 ± 0.01
58155	2018.02.05	2	1.72 ± 0.01
58156	2018.02.06	2	1.36 ± 0.01
58163	2018.02.13	3	1.24 ± 0.02
58169	2018.02.19	2	1.99 ± 0.01
58177	2018.02.27	2	1.57 ± 0.01
58183	2018.03.05	2	1.79 ± 0.01
58190	2018.03.12	2	1.29 ± 0.01
58194	2018.03.16	2	1.29 ± 0.01
58199	2018.03.21	1	1.48 ± 0.01
58203	2018.03.25	2	1.60 ± 0.03
58212	2018.04.03	2	1.19 ± 0.03
58213	2018.04.04	2	1.23 ± 0.01
58214	2018.04.05	2	1.74 ± 0.01
58215	2018.04.06	2	2.51 ± 0.04
58216	2018.04.07	2	2.93 ± 0.01
58217	2018.04.08	2	3.27 ± 0.02
58220	2018.04.11	2	2.45 ± 0.01
58221	2018.04.12	13	3.48 ± 0.36
58222	2018.04.13	2	3.36 ± 0.08
58224	2018.04.15	1	2.90 ± 0.01
58225	2018.04.16	1	1.89 ± 0.01
58226	2018.04.17	1	5.55 ± 0.01
58227	2018.04.18	2	5.37 ± 0.32
58230	2018.04.21	1	3.34 ± 0.01
58231	2018.04.22	1	3.58 ± 0.01
58238	2018.04.29	2	1.66 ± 0.01
58240	2018.05.01	2	1.33 ± 0.01
58243	2018.05.04	2	0.97 ± 0.01
58255	2018.05.15	1	1.08 ± 0.01
58256	2018.05.17	2	1.42 ± 0.02
58278	2018.06.08	2	2.11 ± 0.06
58283	2018.06.13	2	1.28 ± 0.01
58288	2018.06.18	3	1.16 ± 0.01
58308	2018.07.08	3	1.72 ± 0.01
58309	2018.07.09	1	1.75 ± 0.01
58310	2018.07.10	3	1.37 ± 0.01
58335	2018.08.04	4	1.43 ± 0.02
58360	2018.08.29	2	1.37 ± 0.01
58366	2018.09.04	2	0.72 ± 0.01
58418	2018.10.26	2	2.42 ± 0.02
58419	2018.10.27	5	1.91 ± 0.01
58422	2018.10.30	2	2.63 ± 0.03
58423	2018.10.31	2	3.15 ± 0.03
58424	2018.11.01	2	1.63 ± 0.01
58425	2018.11.02	3	2.16 ± 0.01
58426	2018.11.03	2	1.80 ± 0.01
58427	2018.11.04	2	1.72 ± 0.01
58428	2018.11.05	1	1.57 ± 0.01
58430	2018.11.07	5	1.87 ± 0.03
58431	2018.11.08	2	1.44 ± 0.01

Table A1: continued.

MJD epoch 1	yyyy.mm.dd 2	N_{obs} 3	R_{flux} , mJy, σ_R , mJy 4
58432	2018.11.09	2	1.50 ± 0.01
58433	2018.11.10	1	1.39 ± 0.01
58434	2018.11.11	1	2.04 ± 0.01
58435	2018.11.12	3	1.83 ± 0.01
58501	2019.01.17	4	2.40 ± 0.08
58502	2019.01.18	2	1.63 ± 0.01
58503	2019.01.19	2	2.20 ± 0.01
58504	2019.01.20	24	2.82 ± 0.05
58517	2019.02.02	4	3.10 ± 0.01
58518	2019.02.03	2	2.75 ± 0.01
58530	2019.02.15	10	2.30 ± 0.10
58531	2019.02.16	3	1.78 ± 0.01
58532	2019.02.17	3	2.16 ± 0.01
58533	2019.02.18	1	1.92 ± 0.01
58534	2019.02.19	1	1.90 ± 0.01
58549	2019.03.06	2	2.42 ± 0.04
58550	2019.03.07	2	2.60 ± 0.01
58568	2019.03.25	2	2.79 ± 0.01
58573	2019.03.30	2	2.56 ± 0.01
58578	2019.04.04	2	1.72 ± 0.01
58580	2019.04.06	2	2.33 ± 0.01
58582	2019.04.08	2	1.98 ± 0.01
58608	2019.05.04	2	3.15 ± 0.03
58609	2019.05.05	10	2.54 ± 0.02
58610	2019.05.06	9	2.45 ± 0.02
58611	2019.05.07	10	2.52 ± 0.01
58619	2019.05.15	2	1.43 ± 0.06
58620	2019.05.16	2	1.39 ± 0.01
58621	2019.05.17	1	1.15 ± 0.01
58639	2019.06.04	2	2.69 ± 0.01
58643	2019.06.08	2	2.94 ± 0.01
58648	2019.06.13	3	3.80 ± 0.03
58649	2019.06.14	4	3.75 ± 0.02
58651	2019.06.16	3	5.96 ± 0.01
58657	2019.06.22	1	3.65 ± 0.01
58727	2019.08.31	1	1.85 ± 0.01
58743	2019.09.16	2	4.86 ± 0.06
58744	2019.09.17	3	2.46 ± 0.06
58781	2019.10.24	3	0.97 ± 0.02
58782	2019.10.25	3	1.34 ± 0.01
58800	2019.11.12	3	2.73 ± 0.02
58801	2019.11.13	2	2.18 ± 0.01
58802	2019.11.15	2	2.39 ± 0.03
58804	2019.11.16	2	2.27 ± 0.05
58810	2019.11.22	1	2.33 ± 0.01
58812	2019.11.24	1	2.71 ± 0.01
58839	2019.12.21	1	1.22 ± 0.01
58841	2019.12.23	2	1.90 ± 0.01
58894	2020.02.14	2	2.96 ± 0.01
58905	2020.02.25	2	2.26 ± 0.01
58907	2020.02.27	2	1.91 ± 0.01
58915	2020.20.03	4	1.70 ± 0.05
58930	2020.20.03	5	2.24 ± 0.02
58931	2020.20.03	2	2.15 ± 0.01
58942	2020.04.02	3	3.47 ± 0.03
58958	2020.20.04	2	3.52 ± 0.03
58959	2020.20.04	3	4.36 ± 0.01
58966	2020.04.26	2	3.19 ± 0.03
58968	2020.04.28	2	1.74 ± 0.01
59162	2020.11.08	2	1.59 ± 0.01
59165	2020.11.11	4	0.91 ± 0.01
59166	2020.11.12	2	1.15 ± 0.01
59169	2020.11.15	2	2.50 ± 0.02
59190	2020.12.06	2	2.86 ± 0.01

Table A1: continued.

MJD epoch 1	yyyy.mm.dd 2	N_{obs} 3	R_{flux} , mJy, σ_R , mJy 4
59194	2020.12.10	3	1.80 ± 0.01
59195	2020.12.11	2	2.03 ± 0.02
59212	2020.12.27	4	2.96 ± 0.02
59213	2020.12.28	3	2.64 ± 0.05
59214	2020.12.29	2	3.20 ± 0.02
59215	2020.12.30	2	4.46 ± 0.01
59216	2021.01.01	6	3.38 ± 0.39
59217	2021.01.02	19	3.43 ± 0.06
59218	2021.01.03	33	4.02 ± 0.25
59219	2021.01.04	12	5.50 ± 0.65
59231	2021.01.16	5	2.34 ± 0.06
59234	2021.01.19	2	5.94 ± 0.02
59235	2021.01.20	21	5.25 ± 0.35
59236	2021.01.21	21	3.45 ± 0.40
59237	2021.01.22	27	3.50 ± 0.20
59238	2021.01.23	34	4.00 ± 0.30
59240	2021.01.25	1	4.13 ± 0.01
59245	2021.01.30	5	4.35 ± 0.18
59246	2021.01.31	12	4.10 ± 0.17
59247	2021.02.01	13	3.47 ± 0.08
59248	2021.02.02	13	3.57 ± 0.12
59264	2021.02.18	11	3.62 ± 0.06
59265	2021.02.19	20	5.05 ± 0.10
59266	2021.02.20	8	7.66 ± 0.12
59267	2021.02.21	5	6.91 ± 0.06
59270	2021.02.24	11	6.99 ± 0.14
59271	2021.02.25	6	6.21 ± 0.35
59273	2021.02.27	29	8.72 ± 0.52
59275	2021.03.01	23	4.29 ± 0.33
59276	2021.03.02	27	3.97 ± 0.10
59277	2021.03.03	26	3.90 ± 0.08
59278	2021.03.04	66	4.25 ± 0.25
59279	2021.03.05	5	2.59 ± 0.02
59281	2021.03.07	43	3.86 ± 0.54
59282	2021.03.08	34	4.09 ± 0.48
59283	2021.03.09	47	4.70 ± 0.16
59286	2021.03.12	27	4.32 ± 0.41
59287	2021.03.13	51	5.90 ± 0.40
59288	2021.03.14	48	6.03 ± 0.35
59289	2021.03.15	22	5.15 ± 0.15
59291	2021.03.17	4	5.39 ± 0.14
59292	2021.03.18	10	7.11 ± 0.58
59294	2021.03.19	7	6.39 ± 0.45
59294	2021.03.20	25	4.80 ± 0.90
59301	2021.03.27	29	6.71 ± 0.41
59302	2021.03.28	2	5.87 ± 0.07
59303	2021.03.29	25	4.00 ± 0.25
59305	2021.03.31	15	5.09 ± 0.45
59306	2021.04.01	12	4.84 ± 0.20
59307	2021.04.02	19	6.77 ± 0.41
59308	2021.04.03	3	6.12 ± 0.03
59312	2021.04.07	35	4.94 ± 0.21
59318	2021.04.13	8	2.73 ± 0.18
59319	2021.04.14	31	2.95 ± 0.15
59320	2021.04.15	3	4.77 ± 0.17
59321	2021.04.16	2	4.81 ± 0.01
59328	2021.04.23	4	1.44 ± 0.01
59332	2021.04.27	33	1.80 ± 0.25
59333	2021.04.28	22	1.40 ± 0.04
59335	2021.04.30	32	1.59 ± 0.10
59336	2021.05.01	19	1.42 ± 0.07
59337	2021.05.02	20	1.32 ± 0.04
59338	2021.05.03	14	1.19 ± 0.03
59340	2021.05.05	30	1.21 ± 0.02

Table A1: continued.

MJD epoch 1	yyyy.mm.dd 2	N_{obs} 3	R_{flux} , mJy, σ_R , mJy 4
59342	2021.05.07	19	1.57 ± 0.03
59347	2021.05.12	3	0.99 ± 0.01
59348	2021.05.13	21	1.00 ± 0.02
59349	2021.05.14	27	0.99 ± 0.03
59350	2021.05.15	22	0.95 ± 0.04
59351	2021.05.16	30	0.94 ± 0.03
59353	2021.05.18	9	0.78 ± 0.04
59354	2021.05.19	10	0.84 ± 0.03
59355	2021.05.20	3	0.83 ± 0.01
59365	2021.05.30	23	0.79 ± 0.03
59366	2021.05.31	7	0.77 ± 0.02
59369	2021.06.03	18	0.68 ± 0.01
59373	2021.06.07	14	0.83 ± 0.01
59374	2021.06.08	9	0.88 ± 0.02
59376	2021.06.10	3	1.21 ± 0.01
59377	2021.06.11	5	1.48 ± 0.02
59378	2021.06.12	5	1.24 ± 0.01
59379	2021.06.13	12	1.23 ± 0.01
59387	2021.06.21	3	1.82 ± 0.05
59388	2021.06.22	2	2.34 ± 0.01
59393	2021.06.27	3	1.09 ± 0.07
59398	2021.07.02	4	0.98 ± 0.03
59399	2021.07.03	3	0.79 ± 0.01
59401	2021.07.05	3	1.08 ± 0.01
59406	2021.07.10	2	0.98 ± 0.03
59407	2021.07.11	4	0.93 ± 0.01
59409	2021.07.13	4	1.07 ± 0.02
59412	2021.07.16	3	0.97 ± 0.02
59413	2021.07.17	3	0.93 ± 0.03
59414	2021.07.18	3	1.06 ± 0.03
59415	2021.07.19	6	1.25 ± 0.02
59416	2021.07.20	5	1.25 ± 0.05
59425	2021.07.29	4	1.29 ± 0.02
59427	2021.07.31	3	1.15 ± 0.01
59453	2021.08.26	3	2.83 ± 0.02
59454	2021.08.27	3	2.74 ± 0.05
59468	2021.09.10	3	2.91 ± 0.06
59478	2021.09.20	3	2.67 ± 0.04
59483	2021.09.25	3	1.93 ± 0.02
59490	2021.10.02	2	2.26 ± 0.09
59495	2021.10.07	3	2.60 ± 0.02
59496	2021.10.08	9	2.56 ± 0.07
59497	2021.10.09	11	2.66 ± 0.13
59498	2021.10.10	3	1.89 ± 0.05
59500	2021.10.12	9	2.11 ± 0.09
59504	2021.10.16	6	2.65 ± 0.07
59508	2021.10.20	10	2.00 ± 0.03
59509	2021.10.21	10	2.21 ± 0.02
59510	2021.10.22	7	2.34 ± 0.02
59511	2021.10.23	6	2.57 ± 0.03
59513	2021.10.25	4	4.82 ± 0.23
59514	2021.10.26	7	3.44 ± 0.04
59515	2021.10.27	9	2.73 ± 0.02
59516	2021.10.28	2	2.27 ± 0.01
59517	2021.10.29	7	2.52 ± 0.10
59518	2021.10.30	6	2.68 ± 0.02
59522	2021.11.03	9	2.40 ± 0.03
59523	2021.11.04	7	3.59 ± 0.04
59524	2021.11.05	9	2.97 ± 0.07
59525	2021.11.06	5	2.31 ± 0.02
59526	2021.11.07	21	2.18 ± 0.05
59527	2021.11.08	21	2.41 ± 0.07
59530	2021.11.11	20	2.28 ± 0.04
59531	2021.11.12	16	2.03 ± 0.02

Table A1: continued.

MJD epoch 1	yyyy.mm.dd 2	N_{obs} 3	R_{flux} , mJy, σ_R , mJy 4
59532	2021.11.13	20	1.97 ± 0.05
59535	2021.11.16	20	2.48 ± 0.07
59545	2021.11.26	16	2.16 ± 0.05
59555	2021.12.06	3	3.48 ± 0.03
59556	2021.12.07	15	3.13 ± 0.18
59559	2021.12.10	30	2.60 ± 0.15
59560	2021.12.11	19	1.63 ± 0.05
59561	2021.12.12	24	2.31 ± 0.08
59562	2021.12.13	7	2.58 ± 0.05
59564	2021.12.15	18	3.55 ± 0.46
59576	2021.12.27	10	1.36 ± 0.04
59578	2021.12.29	15	1.36 ± 0.09
59584	2022.01.04	2	0.84 ± 0.01
59586	2022.01.06	10	1.02 ± 0.01
59587	2022.01.07	19	1.25 ± 0.06
59589	2022.01.09	13	2.38 ± 0.13
59595	2022.01.15	17	1.15 ± 0.10
59596	2022.01.16	10	1.16 ± 0.02
59605	2022.01.25	16	1.62 ± 0.07
59608	2022.01.28	16	1.73 ± 0.04
59609	2022.01.29	11	1.55 ± 0.05
59614	2022.02.03	3	1.28 ± 0.02
59616	2022.02.05	12	1.80 ± 0.10
59617	2022.02.06	14	2.29 ± 0.06
59621	2022.02.10	10	1.88 ± 0.08
59622	2022.02.11	21	1.90 ± 0.10
59626	2022.02.15	26	1.55 ± 0.06
59630	2022.02.19	3	1.36 ± 0.02
59632	2022.02.21	16	1.74 ± 0.04
59633	2022.02.22	4	1.38 ± 0.01
59635	2022.02.24	4	2.86 ± 0.08
59637	2022.02.26	3	2.31 ± 0.03
59638	2022.02.27	4	2.35 ± 0.07
59639	2022.02.28	4	2.05 ± 0.14
59652	2022.03.13	3	3.43 ± 0.02
59653	2022.03.14	5	2.59 ± 0.07
59656	2022.03.17	1	3.19 ± 0.01
59659	2022.03.20	4	3.10 ± 0.07
59660	2022.03.21	6	4.33 ± 0.50
59661	2022.03.22	6	3.85 ± 0.27
59662	2022.03.23	19	5.78 ± 0.34
59663	2022.03.24	5	5.08 ± 0.15
59664	2022.03.25	2	3.09 ± 0.01
59665	2022.03.26	11	3.33 ± 0.10
59667	2022.03.28	19	3.30 ± 0.25
59668	2022.03.29	3	3.59 ± 0.05
59669	2022.03.30	31	4.40 ± 0.31
59674	2022.04.04	4	2.58 ± 0.05
59676	2022.04.06	4	1.54 ± 0.01
59677	2022.04.07	20	2.00 ± 0.06
59679	2022.04.09	32	3.20 ± 0.23
59681	2022.04.11	15	8.78 ± 0.27
59682	2022.04.12	1	5.29 ± 0.01
59685	2022.04.15	6	10.92 ± 0.31
59686	2022.04.16	35	7.17 ± 0.42
59690	2022.04.20	9	9.22 ± 0.41
59691	2022.04.21	25	14.40 ± 1.30
59692	2022.04.22	5	6.70 ± 0.15
59693	2022.04.23	37	6.40 ± 0.40
59694	2022.04.24	29	4.42 ± 0.18
59696	2022.04.26	3	6.03 ± 0.78
59697	2022.04.27	30	2.85 ± 0.15
59698	2022.04.28	3	1.77 ± 0.05
59699	2022.04.29	31	2.40 ± 0.30

Table A1: continued.

MJD epoch 1	yyyy.mm.dd 2	N_{obs} 3	R_{flux} , mJy, σ_R , mJy 4
59709	2022.05.09	2	8.24 ± 0.08
59711	2022.05.11	99	12.72 ± 2.59
59712	2022.05.12	119	13.32 ± 1.61
59713	2022.05.13	203	16.39 ± 1.58
59714	2022.05.14	32	6.55 ± 0.13
59715	2022.05.15	38	8.33 ± 0.41
59717	2022.05.17	141	1.90 ± 0.17
59718	2022.05.18	40	1.23 ± 0.04
59721	2022.05.21	7	1.28 ± 0.03
59722	2022.05.22	1	1.81 ± 0.01
59726	2022.05.26	3	2.79 ± 0.08
59727	2022.05.27	2	2.33 ± 0.01
59728	2022.05.28	112	6.57 ± 0.92
59729	2022.05.29	62	9.23 ± 0.36
59730	2022.05.30	209	13.37 ± 1.90
59731	2022.05.31	18	6.24 ± 0.45
59732	2022.06.01	26	5.25 ± 0.43
59733	2022.06.02	79	2.68 ± 0.09
59734	2022.06.03	84	2.55 ± 0.10
59736	2022.06.05	57	2.97 ± 0.16
59737	2022.06.06	48	8.01 ± 1.61
59738	2022.06.07	20	4.77 ± 0.52
59742	2022.06.11	22	2.11 ± 0.13
59744	2022.06.13	19	1.81 ± 0.08
59745	2022.06.14	10	1.98 ± 0.05
59748	2022.06.17	9	1.60 ± 0.04
59751	2022.06.20	10	2.06 ± 0.06
59758	2022.06.27	4	2.74 ± 0.04
59759	2022.06.28	4	3.22 ± 0.03
59764	2022.07.03	3	1.80 ± 0.01
59765	2022.07.04	4	1.80 ± 0.06
59766	2022.07.05	4	1.67 ± 0.03
59767	2022.07.06	4	1.67 ± 0.01
59768	2022.07.07	4	1.58 ± 0.03
59769	2022.07.08	3	1.83 ± 0.03
59770	2022.07.09	4	2.73 ± 0.08
59776	2022.07.15	4	4.58 ± 0.01
59782	2022.07.21	2	2.69 ± 0.01
59783	2022.07.22	8	3.24 ± 0.04
59784	2022.07.23	6	2.15 ± 0.02
59788	2022.07.27	3	2.23 ± 0.03
59791	2022.07.30	3	1.91 ± 0.05
59792	2022.07.31	4	2.35 ± 0.01
59797	2022.08.05	5	2.72 ± 0.05
59798	2022.08.06	10	2.78 ± 0.07
59799	2022.08.07	4	3.41 ± 0.02
59800	2022.08.08	4	3.15 ± 0.08
59805	2022.08.13	7	1.73 ± 0.07
59806	2022.08.14	4	2.97 ± 0.07
59812	2022.08.20	8	5.94 ± 0.07
59814	2022.08.22	4	6.87 ± 0.06
59815	2022.08.23	16	6.95 ± 0.13
59819	2022.08.27	9	2.77 ± 0.08
59820	2022.08.28	7	3.49 ± 0.07
59833	2022.09.10	5	3.72 ± 0.03
59848	2022.09.25	3	8.92 ± 0.07
59849	2022.09.26	11	10.09 ± 0.17
59860	2022.10.07	21	10.55 ± 0.12
59884	2022.10.31	6	2.43 ± 0.04
59889	2022.11.05	6	2.58 ± 0.02
59890	2022.11.06	6	5.67 ± 0.08
59896	2022.11.12	9	8.04 ± 0.08
59898	2022.11.14	9	8.98 ± 0.06
59899	2022.11.15	6	8.05 ± 0.06

Table A1: continued.

MJD epoch 1	yyyy.mm.dd 2	N_{obs} 3	R_{flux} , mJy, σ_R , mJy 4
59912	2022.11.28	9	3.77 ± 0.10
59914	2022.11.30	8	3.49 ± 0.03
59915	2022.12.01	22	4.29 ± 0.27
59924	2022.12.10	12	3.36 ± 0.19
59928	2022.12.14	8	1.23 ± 0.04
59930	2022.12.16	7	0.97 ± 0.02
59934	2022.12.20	10	0.75 ± 0.06
59935	2022.12.21	4	0.65 ± 0.04
59937	2022.12.23	8	0.78 ± 0.02
59938	2022.12.24	11	0.85 ± 0.01
59943	2022.12.29	2	1.04 ± 0.01
59944	2022.12.30	2	1.59 ± 0.01
59945	2022.12.31	3	1.10 ± 0.01
59946	2023.01.01	4	1.02 ± 0.03
59947	2023.01.02	6	1.20 ± 0.03
59955	2023.01.10	2	0.48 ± 0.01
59956	2023.01.11	2	0.53 ± 0.01
59957	2023.01.12	2	0.67 ± 0.01
59958	2023.01.13	2	0.99 ± 0.02
59959	2023.01.14	9	1.21 ± 0.01
59960	2023.01.15	7	0.83 ± 0.02
59961	2023.01.16	17	0.97 ± 0.01
59962	2023.01.17	13	0.49 ± 0.01
59963	2023.01.18	17	0.85 ± 0.05
59964	2023.01.19	10	1.17 ± 0.05
59965	2023.01.20	12	0.80 ± 0.02
59966	2023.01.21	12	1.25 ± 0.14
59968	2023.01.23	9	0.69 ± 0.02
59969	2023.01.24	8	0.97 ± 0.01
59970	2023.01.25	6	0.70 ± 0.01
59971	2023.01.26	12	0.66 ± 0.01
59972	2023.01.27	10	0.93 ± 0.01
59975	2023.01.30	14	1.08 ± 0.04
59985	2023.02.09	5	1.75 ± 0.01
59986	2023.02.10	5	2.00 ± 0.03
59987	2023.02.11	4	1.60 ± 0.02
60002	2023.02.26	8	1.45 ± 0.03
60006	2023.03.02	3	1.73 ± 0.01
60012	2023.03.08	9	2.96 ± 0.02
60013	2023.03.09	4	3.35 ± 0.03
60018	2023.03.14	3	3.12 ± 0.05
60030	2023.03.26	105	11.01 ± 1.02
60031	2023.03.27	78	9.95 ± 0.42
60035	2023.03.31	15	5.37 ± 0.15
60036	2023.04.01	28	6.64 ± 0.18
60038	2023.04.03	28	3.60 ± 0.25
60044	2023.04.09	18	6.10 ± 1.60
60045	2023.04.10	4	9.56 ± 0.04
60050	2023.04.15	15	10.87 ± 0.53
60051	2023.04.16	12	8.02 ± 0.25
60052	2023.04.17	11	3.05 ± 0.21
60056	2023.04.21	26	6.74 ± 0.48
60057	2023.04.22	13	5.14 ± 0.08
60058	2023.04.23	9	5.00 ± 0.10
60060	2023.04.25	24	5.31 ± 0.07
60061	2023.04.26	16	7.25 ± 0.25
60062	2023.04.27	15	8.50 ± 0.15
60065	2023.04.30	9	4.28 ± 0.06
60066	2023.05.01	10	3.70 ± 0.10
60068	2023.05.03	12	7.14 ± 0.13
60069	2023.05.04	82	11.00 ± 1.00
60070	2023.05.05	32	5.41 ± 0.10
60071	2023.05.06	18	6.91 ± 0.14
60074	2023.05.09	39	4.05 ± 0.55

Table A1: continued.

MJD epoch 1	yyyy.mm.dd 2	N_{obs} 3	R_{flux} , mJy, σ_R , mJy 4
60080	2023.05.15	39	7.25 ± 0.50
60082	2023.05.17	32	6.25 ± 0.15
60083	2023.05.18	17	6.00 ± 0.50
60084	2023.05.19	31	7.20 ± 0.60
60087	2023.05.22	7	5.60 ± 0.55
60089	2023.05.24	26	5.80 ± 0.18
60090	2023.05.25	18	5.33 ± 0.51
60091	2023.05.26	34	7.11 ± 0.16
60092	2023.05.27	32	5.36 ± 0.16
60094	2023.05.29	4	8.22 ± 0.09
60095	2023.05.30	70	15.31 ± 0.70
60096	2023.05.31	34	12.85 ± 0.56
60097	2023.06.01	133	11.90 ± 1.20
60098	2023.06.02	185	8.80 ± 0.70
60102	2023.06.06	53	3.65 ± 0.25
60103	2023.06.07	15	3.69 ± 0.04
60104	2023.06.08	24	5.68 ± 0.19
60108	2023.06.12	15	8.09 ± 0.13
60109	2023.06.13	18	10.59 ± 0.17
60110	2023.06.14	33	13.08 ± 0.47
60111	2023.06.15	8	12.50 ± 0.16
60112	2023.06.16	14	11.43 ± 0.12
60113	2023.06.17	16	7.55 ± 0.19
60114	2023.06.18	12	5.82 ± 0.04
60115	2023.06.19	17	5.98 ± 0.34
60117	2023.06.21	4	4.32 ± 0.19
60118	2023.06.22	3	3.42 ± 0.04
60119	2023.06.23	5	3.16 ± 0.03
60120	2023.06.24	10	2.70 ± 0.08
60121	2023.06.25	8	3.31 ± 0.06
60122	2023.06.26	7	3.32 ± 0.05
60123	2023.06.27	11	2.77 ± 0.07

Table A2: The RATAN-600 measurements in 1998–2023 and the RT-32 data in 2020–2023: epoch MJD (Col. 1), epoch yyyy.mm.dd (Col. 2), number of observations N_{obs} (Col. 3), the flux densities at 21.7/22.3, 11.2, 7.7/8.2/8.6 GHz, 4.7/5.1, 2.3, 0.96/1.1/1.2 GHz and their errors, Jy (Cols. 4–9); name of telescope (Col. 10). The number N_{obs} is indicated if information is available; for RT-32 the number of observations is given for two frequencies.

MJD epoch	yyyy.mm.dd	N_{obs}	S_{22}, σ	$S_{11.2}, \sigma$	S_8, σ	S_5, σ	$S_{2.3}, \sigma$	$S_{1.1}, \sigma$	Telescope
(Jy)									
51079	1998.09.23	–	0.26 ± 0.04	0.28 ± 0.01	0.31 ± 0.02	0.33 ± 0.01	0.40 ± 0.08	0.59 ± 0.15	RATAN-600
52248	2001.12.05	–	–	0.74 ± 0.02	0.78 ± 0.06	0.74 ± 0.02	0.75 ± 0.10	–	RATAN-600
52405	2002.05.11	–	0.60 ± 0.09	0.75 ± 0.12	0.63 ± 0.06	0.57 ± 0.18	–	–	RATAN-600
52580	2002.11.02	–	0.75 ± 0.05	0.67 ± 0.03	0.63 ± 0.06	0.50 ± 0.06	–	–	RATAN-600
52744	2003.04.15	–	0.58 ± 0.12	0.55 ± 0.02	0.51 ± 0.04	0.49 ± 0.07	–	–	RATAN-600
52803	2003.06.13	–	0.66 ± 0.08	0.55 ± 0.03	0.49 ± 0.02	0.36 ± 0.02	–	–	RATAN-600
52865	2003.08.14	–	0.69 ± 0.08	0.54 ± 0.05	0.50 ± 0.04	–	–	–	RATAN-600
52920	2003.10.08	–	–	0.61 ± 0.07	0.49 ± 0.08	0.48 ± 0.02	0.69 ± 0.12	–	RATAN-600
53475	2005.04.15	–	–	1.33 ± 0.04	1.06 ± 0.04	0.91 ± 0.09	–	–	RATAN-600
53603	2005.08.21	–	1.13 ± 0.16	1.35 ± 0.18	0.93 ± 0.06	1.23 ± 0.07	–	–	RATAN-600
53888	2006.06.02	–	1.12 ± 0.08	1.50 ± 0.03	1.14 ± 0.18	1.16 ± 0.08	–	–	RATAN-600
54014	2006.10.06	–	–	1.88 ± 0.06	1.59 ± 0.30	–	–	1.86 ± 0.43	RATAN-600
54198	2007.04.08	–	1.44 ± 0.07	1.83 ± 0.06	1.76 ± 0.18	1.47 ± 0.09	1.24 ± 0.17	2.41 ± 0.40	RATAN-600
54340	2007.08.28	–	1.48 ± 0.10	1.39 ± 0.04	1.39 ± 0.14	–	0.83 ± 0.19	–	RATAN-600
54710	2008.09.01	–	1.71 ± 0.06	2.14 ± 0.05	2.02 ± 0.14	1.68 ± 0.09	–	–	RATAN-600
55236	2010.02.09	–	1.02 ± 0.15	1.71 ± 0.08	1.66 ± 0.10	–	–	–	RATAN-600
55425	2010.08.17	–	1.01 ± 0.12	1.34 ± 0.06	1.50 ± 0.14	1.48 ± 0.22	–	–	RATAN-600
55575	2011.01.14	–	1.11 ± 0.17	1.13 ± 0.05	1.20 ± 0.04	1.38 ± 0.05	–	–	RATAN-600
55607	2011.02.15	–	1.30 ± 0.13	1.28 ± 0.07	1.18 ± 0.18	1.13 ± 0.05	–	–	RATAN-600
55666	2011.04.15	–	–	1.63 ± 0.07	1.57 ± 0.06	1.36 ± 0.06	–	–	RATAN-600
55845	2011.10.11	–	0.93 ± 0.23	1.46 ± 0.07	1.35 ± 0.12	1.53 ± 0.06	–	–	RATAN-600
55918	2011.12.23	–	1.05 ± 0.09	1.16 ± 0.04	1.23 ± 0.04	1.26 ± 0.06	–	–	RATAN-600
55966	2012.02.09	–	0.97 ± 0.05	1.16 ± 0.04	1.13 ± 0.16	1.09 ± 0.03	–	–	RATAN-600
56215	2012.10.15	–	1.35 ± 0.14	1.14 ± 0.05	0.91 ± 0.08	0.74 ± 0.09	–	–	RATAN-600
56246	2012.11.15	–	1.17 ± 0.22	1.18 ± 0.03	1.10 ± 0.14	0.80 ± 0.08	–	–	RATAN-600
56269	2012.12.08	–	1.42 ± 0.17	1.25 ± 0.05	1.27 ± 0.06	–	–	–	RATAN-600
56317	2013.01.25	–	1.08 ± 0.11	1.23 ± 0.02	1.24 ± 0.08	–	–	–	RATAN-600
56672	2014.01.15	–	1.76 ± 0.18	1.76 ± 0.09	1.80 ± 0.10	1.39 ± 0.03	–	–	RATAN-600
56703	2014.02.15	–	1.91 ± 0.27	1.55 ± 0.07	1.44 ± 0.18	1.15 ± 0.06	–	–	RATAN-600
57034	2015.01.11	4	1.33 ± 0.11	1.42 ± 0.08	–	1.52 ± 0.03	–	–	RATAN-600
57092	2015.03.10	5	1.62 ± 0.13	1.75 ± 0.07	–	1.49 ± 0.05	–	–	RATAN-600
57122	2015.04.09	4	1.29 ± 0.13	1.50 ± 0.07	–	1.30 ± 0.05	–	–	RATAN-600
57153	2015.05.10	4	1.14 ± 0.11	1.03 ± 0.06	–	1.08 ± 0.05	–	–	RATAN-600
57183	2015.06.09	4	0.90 ± 0.10	1.11 ± 0.08	–	1.11 ± 0.05	–	–	RATAN-600
57214	2015.07.10	5	0.94 ± 0.10	0.97 ± 0.06	–	1.11 ± 0.05	–	–	RATAN-600
57274	2015.09.08	2	1.15 ± 0.10	1.04 ± 0.08	–	0.85 ± 0.05	–	–	RATAN-600
57305	2015.10.09	3	1.25 ± 0.10	1.08 ± 0.08	–	0.87 ± 0.05	–	–	RATAN-600
57336	2015.11.09	3	1.36 ± 0.10	0.70 ± 0.05	–	0.67 ± 0.05	–	–	RATAN-600
57367	2015.12.10	4	1.91 ± 0.15	1.29 ± 0.06	–	0.81 ± 0.05	–	–	RATAN-600
57398	2016.01.10	5	2.19 ± 0.15	1.59 ± 0.07	–	0.97 ± 0.05	–	–	RATAN-600
57429	2016.02.10	5	1.93 ± 0.10	1.63 ± 0.07	–	1.01 ± 0.05	–	–	RATAN-600
57458	2016.03.10	6	2.07 ± 0.15	1.84 ± 0.06	–	1.15 ± 0.05	–	–	RATAN-600
57519	2016.05.10	3	1.41 ± 0.10	1.28 ± 0.07	–	1.01 ± 0.05	–	–	RATAN-600
57550	2016.06.10	4	1.48 ± 0.15	1.10 ± 0.07	–	1.14 ± 0.05	–	–	RATAN-600
57580	2016.07.10	2	1.14 ± 0.10	0.93 ± 0.06	–	0.98 ± 0.05	–	–	RATAN-600
57640	2016.09.08	3	1.26 ± 0.10	1.18 ± 0.07	–	0.91 ± 0.05	–	–	RATAN-600
57674	2016.10.12	3	1.19 ± 0.10	1.03 ± 0.06	–	0.88 ± 0.05	–	–	RATAN-600
57703	2016.11.10	6	0.91 ± 0.10	0.96 ± 0.06	–	0.97 ± 0.05	–	–	RATAN-600
57733	2016.12.10	6	0.87 ± 0.10	0.79 ± 0.06	–	0.90 ± 0.05	–	–	RATAN-600
57762	2017.01.08	6	0.83 ± 0.10	0.77 ± 0.06	–	0.69 ± 0.04	–	–	RATAN-600
57795	2017.02.10	5	1.33 ± 0.10	0.79 ± 0.07	–	0.67 ± 0.03	–	–	RATAN-600
57823	2017.03.10	6	1.28 ± 0.10	0.95 ± 0.03	–	0.74 ± 0.04	–	–	RATAN-600
57854	2017.04.10	5	1.27 ± 0.10	0.99 ± 0.06	–	0.70 ± 0.04	–	–	RATAN-600
57884	2017.05.10	5	1.22 ± 0.15	0.93 ± 0.06	–	0.71 ± 0.04	–	–	RATAN-600
57915	2017.06.10	5	0.89 ± 0.10	0.82 ± 0.06	–	0.89 ± 0.05	–	–	RATAN-600
57945	2017.07.10	3	–	0.84 ± 0.06	–	0.89 ± 0.05	–	–	RATAN-600
58909	2020.03.01	43/-	–	–	1.02 ± 0.06	–	–	–	RT-32
58916	2020.03.08	62/42	–	–	0.95 ± 0.04	0.93 ± 0.08	–	–	RT-32
58923	2020.03.15	-/88	–	–	–	0.93 ± 0.04	–	–	RT-32
58937	2020.03.29	67/86	–	–	1.22 ± 0.14	0.92 ± 0.03	–	–	RT-32

Table A2: continued.

MJD epoch 1	yyyy.mm.dd 2	N_{obs} 3	$S_{22.3}, \sigma$ 4	$S_{11.2}, \sigma$ 5	$S_{7.7/8.2}, \sigma$ 6	$S_{4.7}, \sigma$ 7	$S_{2.3}, \sigma$ 8	S_1, σ 9	Telescope 10
58944	2020.04.05	61/60	–	–	1.02 ± 0.08	0.97 ± 0.03	–	–	RT-32
58951	2020.04.12	63/82	–	–	1.01 ± 0.06	0.95 ± 0.02	–	–	RT-32
58958	2020.04.19	62/86	–	–	1.12 ± 0.06	0.95 ± 0.02	–	–	RT-32
58965	2020.04.26	62/44	–	–	1.15 ± 0.06	0.98 ± 0.02	–	–	RT-32
58972	2020.05.03	47/82	–	–	1.12 ± 0.06	0.94 ± 0.02	–	–	RT-32
58979	2020.05.10	-/82	–	–	–	0.99 ± 0.02	–	–	RT-32
58986	2020.05.17	48/-	–	–	1.15 ± 0.06	–	–	–	RT-32
58993	2020.05.24	44/88	–	–	1.07 ± 0.06	0.98 ± 0.07	–	–	RT-32
59000	2020.05.31	62/44	–	–	1.12 ± 0.06	1.01 ± 0.02	–	–	RT-32
59006	2020.06.06	64/20	–	–	1.11 ± 0.06	1.02 ± 0.11	–	–	RT-32
59013	2020.06.13	-/44	–	–	–	1.03 ± 0.04	–	–	RT-32
59024	2020.06.24	65/118	–	–	1.17 ± 0.04	1.01 ± 0.05	–	–	RT-32
59030	2020.06.30	68/112	–	–	1.28 ± 0.06	1.12 ± 0.04	–	–	RT-32
59035	2020.07.05	45/-	–	–	1.29 ± 0.08	–	–	–	RT-32
59036	2020.07.06	-/110	–	–	–	1.10 ± 0.04	–	–	RT-32
59041	2020.07.11	64/-	–	–	1.18 ± 0.08	–	–	–	RT-32
59042	2020.07.12	-/86	–	–	–	1.04 ± 0.03	–	–	RT-32
59048	2020.07.18	44/-	–	–	1.09 ± 0.10	–	–	–	RT-32
59049	2020.07.19	-/44	–	–	–	0.99 ± 0.02	–	–	RT-32
59070	2020.08.09	-/90	–	–	–	1.01 ± 0.02	–	–	RT-32
59077	2020.08.16	-/132	–	–	–	1.03 ± 0.03	–	–	RT-32
59097	2020.09.05	46/-	–	–	0.88 ± 0.12	–	–	–	RT-32
59098	2020.09.06	-/92	–	–	–	0.96 ± 0.03	–	–	RT-32
59112	2020.09.20	43/86	–	–	0.92 ± 0.06	0.93 ± 0.04	–	–	RT-32
59126	2020.10.04	44/-	–	–	0.89 ± 0.04	–	–	–	RT-32
59140	2020.10.18	62/90	–	–	0.88 ± 0.04	0.81 ± 0.02	–	–	RT-32
59161	2020.11.08	46/89	–	–	0.89 ± 0.04	0.81 ± 0.02	–	–	RT-32
59168	2020.11.15	46/82	–	–	0.88 ± 0.06	0.72 ± 0.09	–	–	RT-32
59175	2020.11.22	44/-	–	–	0.89 ± 0.06	–	–	–	RT-32
59189	2020.12.06	36/-	–	–	0.79 ± 0.04	–	–	–	RT-32
59196	2020.12.13	45/88	–	–	0.93 ± 0.06	0.74 ± 0.04	–	–	RT-32
59203	2020.12.20	45/84	–	–	0.80 ± 0.08	0.72 ± 0.02	–	–	RT-32
59217	2021.01.03	30/82	–	–	0.88 ± 0.04	0.73 ± 0.03	–	–	RT-32
59224	2021.01.10	42/90	–	–	0.76 ± 0.06	0.70 ± 0.08	–	–	RT-32
59230	2021.01.16	43/84	–	–	0.91 ± 0.06	0.69 ± 0.03	–	–	RT-32
59237	2021.01.23	-/86	–	–	–	0.71 ± 0.03	–	–	RT-32
59244	2021.01.30	-/84	–	–	–	0.79 ± 0.02	–	–	RT-32
59251	2021.02.06	133/-	–	–	0.88 ± 0.10	–	–	–	RT-32
59254	2021.02.08	3	2.04 ± 0.17	1.13 ± 0.10	–	0.74 ± 0.04	–	–	RATAN-600
59259	2021.02.14	87/-	–	–	1.10 ± 0.08	–	–	–	RT-32
59266	2021.02.21	86/90	–	–	1.25 ± 0.06	0.93 ± 0.03	–	–	RT-32
59282	2021.03.08	2	1.96 ± 0.19	1.39 ± 0.10	–	0.82 ± 0.05	–	–	RATAN-600
59293	2021.03.20	45/90	–	–	1.14 ± 0.06	0.93 ± 0.02	–	–	RT-32
59300	2021.03.27	42/86	–	–	1.21 ± 0.08	0.88 ± 0.02	–	–	RT-32
59307	2021.04.03	46/-	–	–	1.29 ± 0.06	–	–	–	RT-32
59312	2021.04.07	2	–	1.22 ± 0.10	–	0.82 ± 0.05	–	–	RATAN-600
59321	2021.04.17	44/-	–	–	1.25 ± 0.06	–	–	–	RT-32
59322	2021.04.18	-/88	–	–	–	0.98 ± 0.02	–	–	RT-32
59328	2021.04.24	21/-	–	–	1.10 ± 0.14	–	–	–	RT-32
59342	2021.05.08	45/-	–	–	0.97 ± 0.04	–	–	–	RT-32
59343	2021.05.08	2	1.47 ± 0.16	1.15 ± 0.10	–	0.75 ± 0.04	–	–	RATAN-600
59349	2021.05.15	91/-	–	–	0.94 ± 0.08	–	–	–	RT-32
59356	2021.05.22	44/84	–	–	0.80 ± 0.04	0.79 ± 0.02	–	–	RT-32
59375	2021.06.09	1	–	0.71 ± 0.10	–	0.63 ± 0.04	–	–	RATAN-600
59384	2021.06.19	41/-	–	–	0.65 ± 0.04	–	–	–	RT-32
59399	2021.07.04	60/88	–	–	0.62 ± 0.04	0.59 ± 0.03	–	–	RT-32
59405	2021.07.10	79/84	–	–	0.59 ± 0.04	0.55 ± 0.02	–	–	RT-32
59410	2021.07.14	12	1.25 ± 0.14	1.03 ± 0.10	–	0.89 ± 0.03	–	–	RATAN-600
59412	2021.07.17	94/-	–	–	0.54 ± 0.04	–	–	–	RT-32
59419	2021.07.24	-/78	–	–	–	0.53 ± 0.05	–	–	RT-32
59438	2021.08.11	10	1.17 ± 0.10	1.02 ± 0.10	–	0.81 ± 0.05	–	–	RATAN-600
59474	2021.09.16	14	1.30 ± 0.10	1.37 ± 0.10	–	1.15 ± 0.05	–	–	RATAN-600
59495	2021.10.07	25	1.45 ± 0.10	1.28 ± 0.10	–	1.05 ± 0.05	–	–	RATAN-600
59556	2021.12.07	3	0.86 ± 0.10	0.88 ± 0.10	–	0.69 ± 0.02	–	–	RATAN-600

Table A2: continued.

MJD epoch 1	yyyy.mm.dd 2	N_{obs} 3	$S_{22.3}, \sigma$ 4	$S_{11.2}, \sigma$ 5	$S_{7.7/8.2}, \sigma$ 6	$S_{4.7}, \sigma$ 7	$S_{2.3}, \sigma$ 8	S_1, σ 9	Telescope 10
59588	2022.01.08	2	0.98 ± 0.10	0.91 ± 0.10	–	0.62 ± 0.04	–	–	RATAN-600
59619	2022.02.08	3	1.14 ± 0.10	1.11 ± 0.10	–	0.74 ± 0.04	–	–	RATAN-600
59647	2022.03.08	2	1.58 ± 0.10	1.51 ± 0.10	–	0.79 ± 0.05	–	–	RATAN-600
59678	2022.04.08	3	1.81 ± 0.10	1.36 ± 0.10	–	0.86 ± 0.05	–	–	RATAN-600
59709	2022.05.09	2	1.85 ± 0.10	1.52 ± 0.20	–	0.79 ± 0.05	–	–	RATAN-600
59723	2022.05.23	2	1.89 ± 0.10	1.46 ± 0.10	–	0.84 ± 0.05	–	–	RATAN-600
59848	2022.09.25	5	2.27 ± 0.18	2.54 ± 0.30	–	2.24 ± 0.05	–	–	RATAN-600
59891	2022.11.07	3	1.31 ± 0.10	1.64 ± 0.20	–	1.59 ± 0.05	–	–	RATAN-600
59922	2022.12.08	3	1.24 ± 0.15	1.48 ± 0.10	–	1.55 ± 0.05	–	–	RATAN-600
59953	2023.01.08	2	0.85 ± 0.10	1.44 ± 0.10	–	1.40 ± 0.05	–	–	RATAN-600
59985	2023.02.09	1	–	0.73 ± 0.10	–	1.04 ± 0.05	–	–	RATAN-600
60012	2023.03.08	2	1.92 ± 0.15	1.12 ± 0.10	–	0.86 ± 0.05	–	–	RATAN-600
60043	2023.04.08	2	1.63 ± 0.16	1.57 ± 0.20	–	1.06 ± 0.05	–	–	RATAN-600
60074	2023.05.09	1	1.36 ± 0.14	1.81 ± 0.20	–	0.86 ± 0.05	–	–	RATAN-600
60104	2023.06.08	2	–	1.68 ± 0.06	–	0.97 ± 0.06	–	–	RATAN-600
60105	2023.06.10	32/-	–	–	1.39 ± 0.16	–	–	–	RT-32
60106	2023.06.11	20/-	–	–	1.35 ± 0.12	–	–	–	RT-32
60119	2023.06.18	29/-	–	–	1.38 ± 0.08	–	–	–	RT-32

Table A3: The RT-22 measurements in 2009–2023: epoch MJD (Col. 1), epoch yyyy.mm.dd (Col. 2), the flux densities at 36.8 GHz and their errors, Jy (Col. 3).

MJD epoch 1	yyyy.mm.dd 2	$S_{36.8}, \sigma$ 3
55196	2009.12.30	1.79 ± 0.18
55198	2010.01.01	1.59 ± 0.22
55199	2010.01.02	1.54 ± 0.23
55200	2010.01.03	1.39 ± 0.21
55202	2010.01.05	1.33 ± 0.12
55204	2010.01.07	0.99 ± 0.13
55205	2010.01.08	1.14 ± 0.12
55207	2010.01.10	1.74 ± 0.11
55208	2010.01.11	1.64 ± 0.10
55209	2010.01.12	1.49 ± 0.10
55215	2010.01.18	1.34 ± 0.10
55217	2010.01.20	1.29 ± 0.11
55218	2010.01.21	1.52 ± 0.14
55219	2010.01.22	1.39 ± 0.13
55220	2010.01.23	1.24 ± 0.08
55225	2010.01.28	1.48 ± 0.07
55228	2010.01.31	1.53 ± 0.05
55231	2010.02.03	1.51 ± 0.05
55234	2010.02.06	1.50 ± 0.18
55237	2010.02.09	1.47 ± 0.04
55238	2010.02.10	1.42 ± 0.04
55239	2010.02.11	1.36 ± 0.05
55240	2010.02.12	1.44 ± 0.06
55243	2010.02.15	1.33 ± 0.07
55247	2010.02.19	1.04 ± 0.06
55249	2010.02.21	0.95 ± 0.07
55250	2010.02.22	1.43 ± 0.07
55260	2010.03.04	1.20 ± 0.16
55261	2010.03.05	1.26 ± 0.14
55262	2010.03.06	1.51 ± 0.11
55266	2010.03.10	1.40 ± 0.09
55267	2010.03.11	0.97 ± 0.19
55270	2010.03.14	1.05 ± 0.15
55281	2010.03.25	0.94 ± 0.10
55284	2010.03.28	1.04 ± 0.14
55288	2010.04.01	0.95 ± 0.10
55289	2010.04.02	0.76 ± 0.15
55291	2010.04.04	0.65 ± 0.13
55293	2010.04.06	0.97 ± 0.12
55298	2010.04.11	1.10 ± 0.10
55308	2010.04.21	1.58 ± 0.10
55311	2010.04.24	1.18 ± 0.10
55313	2010.04.26	1.58 ± 0.08
55315	2010.04.28	1.16 ± 0.13
55333	2010.05.16	1.62 ± 0.17
55334	2010.05.17	1.55 ± 0.10
55339	2010.05.22	1.58 ± 0.07
55342	2010.05.25	1.52 ± 0.05
55343	2010.05.26	1.44 ± 0.05
55345	2010.05.28	1.48 ± 0.18
55358	2010.06.10	1.56 ± 0.04
55370	2010.06.22	1.46 ± 0.04
55371	2010.06.23	0.98 ± 0.05
55372	2010.06.24	1.27 ± 0.06
55373	2010.06.25	1.06 ± 0.07
55375	2010.06.27	1.35 ± 0.06
55378	2010.06.30	1.14 ± 0.07
55381	2010.07.03	1.29 ± 0.16
55384	2010.07.06	1.31 ± 0.13
55387	2010.07.09	1.55 ± 0.11
55392	2010.07.14	1.14 ± 0.09
55393	2010.07.15	1.34 ± 0.11

Table A3: continued.

MJD epoch 1	yyyy.mm.dd 2	$S_{36.8}, \sigma$ 3
55398	2010.07.20	1.17 ± 0.07
55401	2010.07.23	1.18 ± 0.07
55404	2010.07.26	1.21 ± 0.09
55414	2010.08.05	0.55 ± 0.10
55417	2010.08.08	1.25 ± 0.13
55421	2010.08.12	1.23 ± 0.11
55423	2010.08.14	0.95 ± 0.08
55426	2010.08.17	1.19 ± 0.07
55435	2010.08.26	0.43 ± 0.05
55437	2010.08.28	0.67 ± 0.04
55448	2010.09.08	0.74 ± 0.06
55450	2010.09.10	1.17 ± 0.07
55452	2010.09.12	0.52 ± 0.06
55455	2010.09.15	0.60 ± 0.07
55461	2010.09.21	0.97 ± 0.09
55465	2010.09.25	0.85 ± 0.10
55469	2010.09.29	0.69 ± 0.08
55472	2010.10.02	0.96 ± 0.07
55480	2010.10.10	1.26 ± 0.09
55483	2010.10.13	1.39 ± 0.10
55484	2010.10.14	1.01 ± 0.07
55485	2010.10.15	1.26 ± 0.15
55488	2010.10.18	1.04 ± 0.10
55489	2010.10.19	1.23 ± 0.14
55491	2010.10.21	0.95 ± 0.08
55493	2010.10.23	1.28 ± 0.13
55496	2010.10.26	1.35 ± 0.12
55499	2010.10.29	1.16 ± 0.11
55500	2010.10.30	1.02 ± 0.10
55507	2010.11.06	1.05 ± 0.10
55508	2010.11.07	1.19 ± 0.10
55513	2010.11.12	1.21 ± 0.11
55517	2010.11.16	1.11 ± 0.14
55518	2010.11.17	0.83 ± 0.13
55523	2010.11.22	1.24 ± 0.17
55524	2010.11.23	1.05 ± 0.10
55525	2010.11.24	1.44 ± 0.07
55527	2010.11.26	1.18 ± 0.05
55528	2010.11.27	1.34 ± 0.05
55530	2010.11.29	1.35 ± 0.18
55537	2010.12.06	0.92 ± 0.04
55538	2010.12.07	1.27 ± 0.04
55539	2010.12.08	1.11 ± 0.05
55546	2010.12.15	1.26 ± 0.05
55548	2010.12.17	1.33 ± 0.06
55553	2010.12.22	1.63 ± 0.07
55557	2010.12.26	1.25 ± 0.07
55558	2010.12.27	1.55 ± 0.16
55563	2011.01.01	1.44 ± 0.08
55564	2011.01.02	1.11 ± 0.09
55565	2011.01.03	1.01 ± 0.10
55567	2011.01.05	1.12 ± 0.11
55568	2011.01.06	1.11 ± 0.09
55570	2011.01.08	1.25 ± 0.08
55571	2011.01.09	0.94 ± 0.07
55574	2011.01.12	0.74 ± 0.09
55578	2011.01.16	0.69 ± 0.10
55581	2011.01.19	1.06 ± 0.08
55588	2011.01.26	0.95 ± 0.09
55594	2011.02.01	1.17 ± 0.15
55596	2011.02.03	0.94 ± 0.13
55598	2011.02.05	1.04 ± 0.12
55600	2011.02.07	1.18 ± 0.11
55602	2011.02.09	1.22 ± 0.10

Table A3: continued.

MJD epoch 1	yyyy.mm.dd 2	$S_{36.8}, \sigma$ 3
55605	2011.02.12	1.16 ± 0.07
55609	2011.02.16	1.04 ± 0.11
55612	2011.02.19	0.84 ± 0.14
55616	2011.02.23	0.67 ± 0.13
55618	2011.02.25	0.64 ± 0.17
55619	2011.02.26	0.69 ± 0.10
55625	2011.03.04	0.74 ± 0.07
55626	2011.03.05	0.73 ± 0.05
55627	2011.03.06	0.76 ± 0.05
55631	2011.03.10	0.79 ± 0.18
55633	2011.03.12	0.84 ± 0.04
55634	2011.03.13	0.59 ± 0.04
55638	2011.03.17	0.63 ± 0.05
55646	2011.03.25	0.79 ± 0.06
55648	2011.03.27	0.96 ± 0.07
55650	2011.03.29	1.05 ± 0.06
55654	2011.04.02	1.14 ± 0.07
55660	2011.04.08	1.22 ± 0.07
55662	2011.04.10	1.24 ± 0.16
55663	2011.04.11	1.43 ± 0.14
55665	2011.04.13	1.52 ± 0.11
55666	2011.04.14	1.84 ± 0.13
55667	2011.04.15	1.46 ± 0.13
55669	2011.04.17	1.62 ± 0.06
55672	2011.04.20	1.74 ± 0.09
55675	2011.04.23	1.65 ± 0.08
55681	2011.04.29	1.74 ± 0.17
55688	2011.05.06	1.84 ± 0.09
55708	2011.05.26	1.54 ± 0.14
55710	2011.05.28	1.47 ± 0.19
55718	2011.06.05	1.43 ± 0.15
55721	2011.06.08	1.45 ± 0.10
55727	2011.06.14	1.34 ± 0.14
55738	2011.06.25	1.32 ± 0.07
55743	2011.06.30	1.12 ± 0.12
55746	2011.07.03	1.24 ± 0.11
55747	2011.07.04	0.94 ± 0.10
55748	2011.07.05	1.33 ± 0.10
55749	2011.07.06	1.29 ± 0.10
55753	2011.07.10	1.27 ± 0.11
55756	2011.07.13	1.24 ± 0.14
55759	2011.07.16	1.26 ± 0.13
55759	2011.07.16	1.28 ± 0.17
55766	2011.07.23	1.19 ± 0.10
55768	2011.07.25	1.22 ± 0.07
55769	2011.07.26	1.34 ± 0.05
55771	2011.07.28	1.44 ± 0.05
55775	2011.08.01	1.46 ± 0.18
55778	2011.08.04	1.36 ± 0.03
55779	2011.08.05	1.25 ± 0.05
55782	2011.08.08	1.44 ± 0.06
55784	2011.08.10	1.48 ± 0.07
55785	2011.08.11	1.47 ± 0.06
55788	2011.08.14	1.62 ± 0.07
55789	2011.08.15	1.46 ± 0.07
55791	2011.08.17	1.39 ± 0.16
55793	2011.08.19	0.99 ± 0.14
55794	2011.08.20	1.03 ± 0.11
55796	2011.08.22	1.50 ± 0.13
55798	2011.08.24	1.39 ± 0.10
55799	2011.08.25	1.53 ± 0.11
55810	2011.09.05	1.53 ± 0.08
55812	2011.09.07	1.69 ± 0.16
55813	2011.09.08	1.49 ± 0.14

Table A3: continued.

MJD epoch 1	yyyy.mm.dd 2	$S_{36.8}, \sigma$ 3
55817	2011.09.12	1.43 ± 0.11
55818	2011.09.13	1.29 ± 0.15
55820	2011.09.15	1.39 ± 0.09
55821	2011.09.16	1.29 ± 0.07
55834	2011.09.29	1.28 ± 0.12
55841	2011.10.06	1.34 ± 0.16
55845	2011.10.10	1.37 ± 0.18
55847	2011.10.12	1.19 ± 0.08
55848	2011.10.13	1.38 ± 0.12
55849	2011.10.14	1.09 ± 0.13
55850	2011.10.15	1.16 ± 0.12
55851	2011.10.16	1.43 ± 0.15
55852	2011.10.17	1.38 ± 0.07
55855	2011.10.20	1.39 ± 0.19
55858	2011.10.23	1.06 ± 0.20
55862	2011.10.27	1.29 ± 0.09
55865	2011.10.30	1.47 ± 0.21
55869	2011.11.03	1.26 ± 0.19
55873	2011.11.07	1.27 ± 0.13
55880	2011.11.14	1.24 ± 0.10
55883	2011.11.17	1.16 ± 0.08
55888	2011.11.22	1.16 ± 0.07
55889	2011.11.23	1.14 ± 0.19
55890	2011.11.24	1.18 ± 0.14
55894	2011.11.28	1.14 ± 0.10
55896	2011.11.30	1.09 ± 0.13
55897	2011.12.01	1.06 ± 0.12
55918	2011.12.22	1.05 ± 0.13
55923	2011.12.27	1.04 ± 0.10
55932	2012.01.05	0.99 ± 0.15
55946	2012.01.19	0.94 ± 0.13
55949	2012.01.22	0.92 ± 0.19
55950	2012.01.23	0.94 ± 0.17
55953	2012.01.26	1.15 ± 0.11
55957	2012.01.30	1.15 ± 0.16
55959	2012.02.01	1.12 ± 0.12
55965	2012.02.07	1.11 ± 0.10
55968	2012.02.10	1.04 ± 0.17
55971	2012.02.13	1.02 ± 0.14
55975	2012.02.17	1.05 ± 0.10
55978	2012.02.20	1.01 ± 0.11
55985	2012.02.27	1.02 ± 0.07
55988	2012.03.01	0.92 ± 0.11
55996	2012.03.09	1.04 ± 0.09
55997	2012.03.10	0.98 ± 0.18
56004	2012.03.17	1.05 ± 0.08
56006	2012.03.19	1.04 ± 0.12
56013	2012.03.26	0.98 ± 0.13
56025	2012.04.07	0.98 ± 0.12
56027	2012.04.09	0.99 ± 0.15
56033	2012.04.15	1.03 ± 0.07
56044	2012.04.26	1.07 ± 0.19
56082	2012.06.03	1.19 ± 0.20
56108	2012.06.29	1.16 ± 0.09
56112	2012.07.03	0.70 ± 0.21
56147	2012.08.07	0.87 ± 0.19
56153	2012.08.13	0.63 ± 0.13
56156	2012.08.16	0.59 ± 0.10
56166	2012.08.26	0.89 ± 0.09
56170	2012.08.30	0.87 ± 0.11
56173	2012.09.02	0.88 ± 0.07
56178	2012.09.07	0.55 ± 0.08
56181	2012.09.10	0.91 ± 0.11
56183	2012.09.12	0.91 ± 0.13

Table A3: continued.

MJD epoch 1	yyyy.mm.dd 2	$S_{36.8}, \sigma$ 3
56186	2012.09.15	0.84 ± 0.15
56192	2012.09.21	0.96 ± 0.13
56198	2012.09.27	0.98 ± 0.10
56200	2012.09.29	0.78 ± 0.13
56202	2012.10.01	1.03 ± 0.12
56209	2012.10.08	1.09 ± 0.10
56210	2012.10.09	1.10 ± 0.14
56215	2012.10.14	1.12 ± 0.19
56219	2012.10.18	1.14 ± 0.16
56221	2012.10.20	0.86 ± 0.15
56222	2012.10.21	1.15 ± 0.13
56226	2012.10.25	1.14 ± 0.14
56227	2012.10.26	1.16 ± 0.19
56228	2012.10.27	1.14 ± 0.11
56231	2012.10.30	1.13 ± 0.13
56235	2012.11.03	1.12 ± 0.15
56246	2012.11.14	1.06 ± 0.16
56254	2012.11.22	1.15 ± 0.14
56255	2012.11.23	1.15 ± 0.15
56256	2012.11.24	1.15 ± 0.15
56259	2012.11.27	1.23 ± 0.13
56267	2012.12.05	1.21 ± 0.12
56271	2012.12.09	1.22 ± 0.11
56279	2012.12.17	1.22 ± 0.10
56294	2013.01.01	1.15 ± 0.10
56301	2013.01.08	1.05 ± 0.10
56314	2013.01.21	1.09 ± 0.11
56316	2013.01.23	1.11 ± 0.14
56319	2013.01.26	0.96 ± 0.13
56323	2013.01.30	1.15 ± 0.17
56328	2013.02.04	1.46 ± 0.10
56331	2013.02.07	1.17 ± 0.07
56343	2013.02.19	1.21 ± 0.05
56349	2013.02.25	1.22 ± 0.05
56352	2013.02.28	1.17 ± 0.18
56356	2013.03.04	1.24 ± 0.04
56364	2013.03.12	1.23 ± 0.04
56369	2013.03.17	1.32 ± 0.05
56370	2013.03.18	1.06 ± 0.06
56373	2013.03.21	1.31 ± 0.07
56375	2013.03.23	1.27 ± 0.06
56384	2013.04.01	1.19 ± 0.07
56390	2013.04.07	1.14 ± 0.07
56399	2013.04.16	1.25 ± 0.16
56403	2013.04.20	1.24 ± 0.14
56406	2013.04.23	1.20 ± 0.11
56412	2013.04.29	1.16 ± 0.13
56427	2013.05.14	1.14 ± 0.13
56431	2013.05.18	1.18 ± 0.07
56450	2013.06.06	1.11 ± 0.11
56454	2013.06.10	1.03 ± 0.12
56471	2013.06.27	0.99 ± 0.16
56473	2013.06.29	0.94 ± 0.18
56495	2013.07.21	1.03 ± 0.08
56511	2013.08.06	1.06 ± 0.12
56517	2013.08.12	1.13 ± 0.13
56523	2013.08.18	1.11 ± 0.12
56535	2013.08.30	1.17 ± 0.15
56536	2013.08.31	1.14 ± 0.07
56539	2013.09.03	1.20 ± 0.19
56548	2013.09.12	1.17 ± 0.20
56551	2013.09.15	1.04 ± 0.09
56554	2013.09.18	1.22 ± 0.17
56559	2013.09.23	1.23 ± 0.13

Table A3: continued.

MJD epoch 1	yyyy.mm.dd 2	$S_{36.8}, \sigma$ 3
56562	2013.09.26	1.27 ± 0.10
56569	2013.10.03	1.34 ± 0.09
56571	2013.10.05	1.38 ± 0.11
56572	2013.10.06	1.42 ± 0.07
56574	2013.10.08	1.47 ± 0.19
56580	2013.10.14	1.69 ± 0.16
56583	2013.10.17	1.64 ± 0.11
56587	2013.10.21	1.66 ± 0.12
56594	2013.10.28	1.71 ± 0.13
56596	2013.10.30	1.71 ± 0.15
56601	2013.11.04	1.63 ± 0.13
56611	2013.11.14	1.73 ± 0.11
56613	2013.11.16	1.79 ± 0.12
56615	2013.11.18	1.73 ± 0.13
56618	2013.11.21	1.83 ± 0.15
56626	2013.11.29	1.79 ± 0.16
56630	2013.12.03	1.70 ± 0.12
56638	2013.12.11	1.67 ± 0.11
56643	2013.12.16	1.61 ± 0.11
56647	2013.12.20	1.66 ± 0.13
56658	2013.12.31	1.63 ± 0.11
56662	2014.01.04	1.65 ± 0.12
56666	2014.01.08	1.58 ± 0.13
56670	2014.01.12	1.59 ± 0.08
56671	2014.01.13	1.74 ± 0.10
56675	2014.01.17	1.69 ± 0.14
56680	2014.01.22	1.44 ± 0.16
56681	2014.01.23	1.34 ± 0.20
56682	2014.01.24	1.21 ± 0.07
56684	2014.01.26	1.57 ± 0.15
56689	2014.01.31	1.44 ± 0.23
56690	2014.02.01	1.31 ± 0.20
56692	2014.02.03	1.29 ± 0.26
56693	2014.02.04	1.32 ± 0.23
56694	2014.02.05	1.33 ± 0.14
56695	2014.02.06	1.19 ± 0.11
56699	2014.02.10	0.94 ± 0.17
56702	2014.02.13	0.84 ± 0.16
56708	2014.02.19	0.68 ± 0.11
56715	2014.02.26	0.75 ± 0.06
56719	2014.03.02	0.88 ± 0.13
56725	2014.03.08	0.94 ± 0.17
56726	2014.03.09	1.04 ± 0.10
56733	2014.03.16	1.14 ± 0.12
56736	2014.03.19	1.21 ± 0.12
56739	2014.03.22	1.04 ± 0.16
56740	2014.03.23	0.84 ± 0.18
56746	2014.03.29	0.69 ± 0.10
56750	2014.04.02	0.91 ± 0.11
56751	2014.04.03	1.16 ± 0.09
56752	2014.04.04	1.18 ± 0.15
56760	2014.04.12	1.20 ± 0.09
56761	2014.04.13	1.07 ± 0.07
56762	2014.04.14	1.26 ± 0.09
56766	2014.04.18	1.24 ± 0.13
56769	2014.04.21	1.18 ± 0.14
56769	2014.04.21	1.16 ± 0.10
56778	2014.04.30	1.06 ± 0.06
56784	2014.05.06	1.01 ± 0.15
56786	2014.05.08	0.99 ± 0.15
56787	2014.05.09	1.05 ± 0.16
56795	2014.05.17	1.29 ± 0.12
56798	2014.05.20	1.45 ± 0.07
56807	2014.05.29	1.59 ± 0.10

Table A3: continued.

MJD epoch 1	yyyy.mm.dd 2	$S_{36.8}, \sigma$ 3
56817	2014.06.08	1.53 ± 0.15
56818	2014.06.09	1.29 ± 0.07
56832	2014.06.23	1.18 ± 0.11
56842	2014.07.03	1.14 ± 0.12
56844	2014.07.05	1.06 ± 0.12
56852	2014.07.13	1.14 ± 0.12
56856	2014.07.17	1.53 ± 0.09
56860	2014.07.21	1.44 ± 0.15
56864	2014.07.25	1.35 ± 0.07
56867	2014.07.28	1.22 ± 0.16
56871	2014.08.01	1.17 ± 0.09
56881	2014.08.11	1.23 ± 0.21
56890	2014.08.20	1.27 ± 0.19
56900	2014.08.30	1.30 ± 0.13
56901	2014.08.31	1.34 ± 0.10
56902	2014.09.01	1.43 ± 0.09
56928	2014.09.27	1.36 ± 0.11
56932	2014.10.01	1.33 ± 0.07
56940	2014.10.09	1.46 ± 0.09
56943	2014.10.12	1.47 ± 0.10
56944	2014.10.13	1.45 ± 0.27
56948	2014.10.17	1.54 ± 0.11
56951	2014.10.20	1.64 ± 0.14
56954	2014.10.23	1.55 ± 0.11
56955	2014.10.24	1.53 ± 0.30
56958	2014.10.27	1.42 ± 0.09
56962	2014.10.31	1.44 ± 0.12
56967	2014.11.05	1.48 ± 0.13
56968	2014.11.06	1.39 ± 0.12
56969	2014.11.07	1.35 ± 0.10
56971	2014.11.09	1.24 ± 0.16
56977	2014.11.15	1.19 ± 0.15
56978	2014.11.16	1.07 ± 0.07
56981	2014.11.19	1.29 ± 0.10
56983	2014.11.21	1.46 ± 0.10
56988	2014.11.26	1.24 ± 0.12
56989	2014.11.27	1.12 ± 0.20
56990	2014.11.28	1.11 ± 0.12
56992	2014.11.30	1.12 ± 0.13
56995	2014.12.03	1.13 ± 0.27
57004	2014.12.12	1.14 ± 0.19
57019	2014.12.27	1.19 ± 0.11
57020	2014.12.28	1.09 ± 0.13
57021	2014.12.29	1.04 ± 0.13
57022	2014.12.30	1.01 ± 0.12
57026	2015.01.03	0.96 ± 0.13
57026	2015.01.03	0.95 ± 0.15
57027	2015.01.04	0.94 ± 0.08
57031	2015.01.08	1.04 ± 0.16
57032	2015.01.09	1.18 ± 0.13
57036	2015.01.13	1.24 ± 0.17
57047	2015.01.24	1.34 ± 0.11
57051	2015.01.28	1.47 ± 0.06
57052	2015.01.29	1.51 ± 0.13
57056	2015.02.02	1.55 ± 0.07
57058	2015.02.04	1.44 ± 0.17
57060	2015.02.06	1.25 ± 0.07
57061	2015.02.07	1.50 ± 0.09
57062	2015.02.08	1.39 ± 0.15
57063	2015.02.09	1.20 ± 0.06
57064	2015.02.10	1.25 ± 0.09
57065	2015.02.11	1.35 ± 0.10
57067	2015.02.13	1.59 ± 0.08
57068	2015.02.14	1.62 ± 0.10

Table A3: continued.

MJD epoch 1	yyyy.mm.dd 2	$S_{36.8}, \sigma$ 3
57070	2015.02.16	1.80 ± 0.05
57073	2015.02.19	1.77 ± 0.10
57074	2015.02.20	1.70 ± 0.11
57075	2015.02.21	1.57 ± 0.08
57077	2015.02.23	1.52 ± 0.07
57078	2015.02.24	1.29 ± 0.12
57079	2015.02.25	1.16 ± 0.10
57080	2015.02.26	1.14 ± 0.13
57085	2015.03.03	1.16 ± 0.15
57086	2015.03.04	1.24 ± 0.06
57087	2015.03.05	1.30 ± 0.10
57089	2015.03.07	1.18 ± 0.10
57090	2015.03.08	0.90 ± 0.06
57091	2015.03.09	1.05 ± 0.09
57092	2015.03.10	1.48 ± 0.11
57093	2015.03.11	1.62 ± 0.09
57094	2015.03.12	1.27 ± 0.06
57097	2015.03.15	1.40 ± 0.10
57102	2015.03.20	1.22 ± 0.09
57111	2015.03.29	0.88 ± 0.10
57113	2015.03.31	0.72 ± 0.10
57115	2015.04.02	0.79 ± 0.11
57116	2015.04.03	0.84 ± 0.07
57128	2015.04.15	1.03 ± 0.15
57129	2015.04.16	1.14 ± 0.08
57132	2015.04.19	0.87 ± 0.08
57134	2015.04.21	0.77 ± 0.12
57146	2015.05.03	0.72 ± 0.05
57157	2015.05.14	1.01 ± 0.07
57165	2015.05.22	1.00 ± 0.07
57166	2015.05.23	0.95 ± 0.09
57178	2015.06.04	1.03 ± 0.09
57179	2015.06.05	1.07 ± 0.10
57185	2015.06.11	0.75 ± 0.11
57199	2015.06.25	0.47 ± 0.07
57205	2015.07.01	0.80 ± 0.06
57213	2015.07.09	1.02 ± 0.10
57216	2015.07.12	1.12 ± 0.09
57222	2015.07.18	1.29 ± 0.08
57226	2015.07.22	1.33 ± 0.09
57235	2015.07.31	1.05 ± 0.10
57241	2015.08.06	1.06 ± 0.11
57257	2015.08.22	1.18 ± 0.09
57259	2015.08.24	1.31 ± 0.15
57260	2015.08.25	1.38 ± 0.11
57261	2015.08.26	1.52 ± 0.07
57269	2015.09.03	1.41 ± 0.11
57274	2015.09.08	1.32 ± 0.12
57282	2015.09.16	1.18 ± 0.13
57294	2015.09.28	0.93 ± 0.08
57304	2015.10.08	1.01 ± 0.11
57305	2015.10.09	1.12 ± 0.09
57308	2015.10.12	1.17 ± 0.09
57329	2015.11.02	1.53 ± 0.08
57336	2015.11.09	1.65 ± 0.10
57346	2015.11.19	1.51 ± 0.08
57355	2015.11.28	1.46 ± 0.08
57363	2015.12.06	1.51 ± 0.07
57368	2015.12.11	1.65 ± 0.12
57371	2015.12.14	1.65 ± 0.10
57386	2015.12.29	1.93 ± 0.13
57390	2016.01.02	1.91 ± 0.11
57398	2016.01.10	1.99 ± 0.15
57401	2016.01.13	1.94 ± 0.11

Table A3: continued.

MJD epoch 1	yyyy.mm.dd 2	$S_{36.8}, \sigma$ 3
57411	2016.01.23	1.78 ± 0.11
57417	2016.01.29	1.81 ± 0.12
57423	2016.02.04	1.87 ± 0.09
57428	2016.02.09	2.26 ± 0.12
57434	2016.02.15	2.05 ± 0.10
57453	2016.03.05	2.04 ± 0.11
57455	2016.03.07	1.99 ± 0.15
57457	2016.03.09	1.94 ± 0.16
57461	2016.03.13	1.96 ± 0.10
57480	2016.04.01	1.69 ± 0.08
57493	2016.04.14	1.17 ± 0.07
57494	2016.04.15	1.17 ± 0.05
57500	2016.04.21	0.96 ± 0.04
57511	2016.05.02	0.89 ± 0.10
57525	2016.05.16	0.78 ± 0.04
57530	2016.05.21	0.73 ± 0.03
57534	2016.05.25	0.78 ± 0.13
57543	2016.06.03	0.84 ± 0.15
57550	2016.06.10	1.54 ± 0.10
57553	2016.06.13	1.52 ± 0.13
57560	2016.06.20	1.48 ± 0.15
57571	2016.07.01	1.44 ± 0.11
57574	2016.07.04	1.34 ± 0.10
57579	2016.07.09	1.16 ± 0.12
57600	2016.07.30	1.10 ± 0.17
57603	2016.08.02	1.13 ± 0.13
57604	2016.08.03	1.16 ± 0.08
57608	2016.08.07	1.24 ± 0.12
57612	2016.08.11	1.13 ± 0.13
57626	2016.08.25	1.28 ± 0.15
57645	2016.09.13	1.29 ± 0.19
57649	2016.09.17	1.18 ± 0.13
57660	2016.09.28	1.21 ± 0.11
57665	2016.10.03	1.24 ± 0.15
57669	2016.10.07	1.21 ± 0.09
57676	2016.10.14	1.08 ± 0.13
57679	2016.10.17	1.06 ± 0.11
57684	2016.10.22	1.01 ± 0.15
57688	2016.10.26	0.98 ± 0.09
57719	2016.11.26	0.88 ± 0.11
57725	2016.12.02	0.86 ± 0.19
57729	2016.12.06	0.87 ± 0.09
57733	2016.12.10	0.81 ± 0.08
57736	2016.12.13	0.84 ± 0.07
57741	2016.12.18	0.87 ± 0.10
57744	2016.12.21	0.87 ± 0.09
57754	2016.12.31	0.85 ± 0.07
57756	2017.01.02	0.99 ± 0.09
57772	2017.01.18	1.14 ± 0.11
57774	2017.01.20	1.24 ± 0.15
57782	2017.01.28	1.29 ± 0.16
57789	2017.02.04	1.34 ± 0.11
57796	2017.02.11	1.39 ± 0.15
57800	2017.02.15	1.34 ± 0.13
57802	2017.02.17	1.29 ± 0.11
57808	2017.02.23	1.27 ± 0.10
57846	2017.04.02	1.24 ± 0.15
57851	2017.04.07	1.21 ± 0.16
57862	2017.04.18	1.26 ± 0.11
57864	2017.04.20	1.26 ± 0.15
57871	2017.04.27	1.24 ± 0.13
57878	2017.05.04	1.18 ± 0.15
57886	2017.05.12	1.06 ± 0.10
57897	2017.05.23	0.97 ± 0.13

Table A3: continued.

MJD epoch 1	yyyy.mm.dd 2	$S_{36.8}, \sigma$ 3
57905	2017.05.31	0.93 ± 0.15
57935	2017.06.30	0.77 ± 0.11
57939	2017.07.04	0.73 ± 0.10
57968	2017.08.02	0.76 ± 0.12
57977	2017.08.11	0.88 ± 0.17
57982	2017.08.16	0.78 ± 0.13
57990	2017.08.24	0.68 ± 0.08
57993	2017.08.27	0.75 ± 0.12
57998	2017.09.01	0.78 ± 0.13
58004	2017.09.07	0.81 ± 0.15
58011	2017.09.14	0.79 ± 0.19
58026	2017.09.29	0.83 ± 0.13
58030	2017.10.03	0.88 ± 0.15
58039	2017.10.12	0.93 ± 0.16
58048	2017.10.21	0.82 ± 0.15
58050	2017.10.23	0.81 ± 0.13
58051	2017.10.24	0.87 ± 0.15
58054	2017.10.27	0.88 ± 0.13
58059	2017.11.01	0.76 ± 0.11
58061	2017.11.03	0.76 ± 0.15
58065	2017.11.07	0.76 ± 0.09
58069	2017.11.11	0.78 ± 0.11
58071	2017.11.13	0.79 ± 0.15
58087	2017.11.29	0.68 ± 0.13
58096	2017.12.08	0.67 ± 0.12
58110	2017.12.22	0.63 ± 0.11
58114	2017.12.26	0.62 ± 0.10
58120	2018.01.01	0.63 ± 0.10
58123	2018.01.04	0.62 ± 0.10
58136	2018.01.17	0.62 ± 0.11
58141	2018.01.22	0.64 ± 0.14
58144	2018.01.25	0.66 ± 0.13
58158	2018.02.08	0.68 ± 0.17
58197	2018.03.19	0.73 ± 0.03
58198	2018.03.20	0.70 ± 0.05
58199	2018.03.21	0.74 ± 0.08
58200	2018.03.22	0.70 ± 0.07
58211	2018.04.02	0.72 ± 0.08
58221	2018.04.12	0.72 ± 0.10
58229	2018.04.20	0.67 ± 0.14
58232	2018.04.23	0.60 ± 0.19
58236	2018.04.27	0.54 ± 0.04
58277	2018.06.07	0.48 ± 0.06
58279	2018.06.09	0.45 ± 0.02
58308	2018.07.08	0.56 ± 0.07
58313	2018.07.13	0.58 ± 0.09
58390	2018.09.28	0.60 ± 0.03
58391	2018.09.29	0.63 ± 0.06
58395	2018.10.03	0.63 ± 0.03
58404	2018.10.12	0.60 ± 0.03
58409	2018.10.17	0.63 ± 0.06
58417	2018.10.25	0.62 ± 0.17
58420	2018.10.28	0.63 ± 0.13
58423	2018.10.31	0.61 ± 0.08
58433	2018.11.10	0.58 ± 0.12
58446	2018.11.23	0.55 ± 0.13
58449	2018.11.26	0.54 ± 0.15
58454	2018.12.01	0.56 ± 0.10
58456	2018.12.03	0.58 ± 0.09
58464	2018.12.11	0.56 ± 0.07
58476	2018.12.23	0.59 ± 0.09
58478	2018.12.25	0.56 ± 0.10
58481	2018.12.28	0.63 ± 0.11
58484	2018.12.31	0.64 ± 0.08

Table A3: continued.

MJD epoch 1	yyyy.mm.dd 2	$S_{36.8}, \sigma$ 3
58492	2019.01.08	0.64 ± 0.10
58499	2019.01.15	0.71 ± 0.13
58512	2019.01.28	0.75 ± 0.14
58543	2019.02.28	1.03 ± 0.09
58549	2019.03.06	1.06 ± 0.11
58562	2019.03.19	1.14 ± 0.13
58569	2019.03.26	1.12 ± 0.14
58591	2019.04.17	1.22 ± 0.09
58594	2019.04.20	1.29 ± 0.11
58600	2019.04.26	1.43 ± 0.07
58609	2019.05.05	1.34 ± 0.12
58630	2019.05.26	1.27 ± 0.17
58636	2019.06.01	1.25 ± 0.13
58644	2019.06.09	1.33 ± 0.08
58646	2019.06.11	1.33 ± 0.12
58653	2019.06.18	1.38 ± 0.13
58667	2019.07.02	1.34 ± 0.15
58681	2019.07.16	1.42 ± 0.10
58683	2019.07.18	1.52 ± 0.13
58686	2019.07.21	1.28 ± 0.15
58692	2019.07.27	0.94 ± 0.11
58693	2019.07.28	1.19 ± 0.10
58700	2019.08.04	1.44 ± 0.12
58701	2019.08.05	1.73 ± 0.17
58709	2019.08.13	1.59 ± 0.13
58711	2019.08.15	1.54 ± 0.08
58719	2019.08.23	1.58 ± 0.12
58721	2019.08.25	1.90 ± 0.10
58722	2019.08.26	1.74 ± 0.19
58736	2019.09.09	1.04 ± 0.13
58738	2019.09.11	1.24 ± 0.15
58739	2019.09.12	1.27 ± 0.12
58742	2019.09.15	1.27 ± 0.10
58743	2019.09.16	1.30 ± 0.13
58744	2019.09.17	1.27 ± 0.09
58757	2019.09.30	1.24 ± 0.07
58758	2019.10.01	1.27 ± 0.16
58759	2019.10.02	1.26 ± 0.12
58760	2019.10.03	1.28 ± 0.17
58761	2019.10.04	1.29 ± 0.13
58762	2019.10.05	1.27 ± 0.08
58766	2019.10.09	1.33 ± 0.12
58768	2019.10.11	1.32 ± 0.13
58769	2019.10.12	1.32 ± 0.15
58770	2019.10.13	1.30 ± 0.11
58771	2019.10.14	1.28 ± 0.07
58773	2019.10.16	1.30 ± 0.13
58774	2019.10.17	1.30 ± 0.15
58776	2019.10.19	1.28 ± 0.07
58777	2019.10.20	1.27 ± 0.10
58778	2019.10.21	1.26 ± 0.07
58781	2019.10.24	1.27 ± 0.12
58782	2019.10.25	1.26 ± 0.13
58785	2019.10.28	1.25 ± 0.15
58786	2019.10.29	1.25 ± 0.19
58787	2019.10.30	1.24 ± 0.13
58788	2019.10.31	1.25 ± 0.15
58790	2019.11.02	1.26 ± 0.16
58791	2019.11.03	1.22 ± 0.15
58792	2019.11.04	1.23 ± 0.13
58796	2019.11.08	1.44 ± 0.15
58799	2019.11.11	1.24 ± 0.13
58806	2019.11.18	1.35 ± 0.07
58813	2019.11.25	1.44 ± 0.15

Table A3: continued.

MJD epoch 1	yyyy.mm.dd 2	$S_{36.8}, \sigma$ 3
58817	2019.11.29	1.51 ± 0.16
58820	2019.12.02	1.58 ± 0.10
58823	2019.12.05	1.73 ± 0.06
58831	2019.12.13	1.73 ± 0.08
58835	2019.12.17	1.58 ± 0.07
58840	2019.12.22	1.70 ± 0.13
58843	2019.12.25	1.54 ± 0.16
58844	2019.12.26	1.44 ± 0.12
58846	2019.12.28	1.41 ± 0.17
58851	2020.01.02	1.49 ± 0.13
58852	2020.01.03	1.73 ± 0.08
58853	2020.01.04	1.52 ± 0.12
58856	2020.01.07	1.22 ± 0.13
58870	2020.01.21	1.14 ± 0.15
58898	2020.02.18	1.09 ± 0.13
58904	2020.02.24	1.16 ± 0.11
58907	2020.02.27	1.05 ± 0.09
58942	2020.04.02	1.09 ± 0.06
58946	2020.04.06	1.54 ± 0.18
58950	2020.04.10	1.89 ± 0.08
58969	2020.04.29	1.97 ± 0.10
58971	2020.05.01	1.84 ± 0.14
58976	2020.05.06	1.75 ± 0.11
58998	2020.05.28	1.99 ± 0.13
59010	2020.06.09	2.13 ± 0.16
59012	2020.06.11	2.05 ± 0.11
59027	2020.06.26	2.02 ± 0.15
59040	2020.07.09	1.44 ± 0.14
59084	2020.08.22	0.79 ± 0.03
59092	2020.08.30	0.77 ± 0.03
59103	2020.09.10	0.89 ± 0.15
59121	2020.09.28	1.04 ± 0.09
59143	2020.10.20	1.24 ± 0.13
59165	2020.11.11	1.19 ± 0.19
59183	2020.11.29	1.25 ± 0.11
59201	2020.12.17	1.48 ± 0.19
59217	2021.01.02	1.90 ± 0.16
59222	2021.01.07	2.29 ± 0.12
59226	2021.01.11	2.44 ± 0.17
59231	2021.01.16	2.39 ± 0.20
59243	2021.01.28	2.34 ± 0.15
59254	2021.02.08	2.14 ± 0.16
59281	2021.03.07	2.04 ± 0.13
59283	2021.03.09	1.94 ± 0.18
59288	2021.03.14	1.89 ± 0.20
59290	2021.03.16	1.86 ± 0.21
59319	2021.04.14	1.74 ± 0.13
59356	2021.05.21	1.39 ± 0.15
59360	2021.05.25	1.34 ± 0.13
59362	2021.05.27	1.29 ± 0.10
59366	2021.05.31	1.14 ± 0.07
59381	2021.06.15	1.24 ± 0.14
59414	2021.07.18	1.29 ± 0.15
59427	2021.07.31	1.24 ± 0.16
59473	2021.09.15	1.34 ± 0.10
59512	2021.10.24	0.88 ± 0.04
59524	2021.11.05	0.95 ± 0.09
59531	2021.11.12	0.80 ± 0.02
59532	2021.11.13	0.78 ± 0.02
59533	2021.11.14	0.79 ± 0.03
59560	2021.12.11	1.04 ± 0.11
59615	2022.02.04	1.22 ± 0.05
59618	2022.02.07	1.27 ± 0.06
59642	2022.03.03	1.79 ± 0.08

Table A3: continued.

MJD epoch 1	yyyy.mm.dd 2	$S_{36.8}, \sigma$ 3
59661	2022.03.22	1.81 ± 0.09
59667	2022.03.28	1.94 ± 0.09
59681	2022.04.11	2.14 ± 0.10
59702	2022.05.02	1.94 ± 0.12
59706	2022.05.06	1.89 ± 0.16
59717	2022.05.17	2.04 ± 0.14
59732	2022.06.01	3.04 ± 0.15
59762	2022.07.01	4.00 ± 0.19
59766	2022.07.05	4.09 ± 0.21
59775	2022.07.14	3.22 ± 0.16
59784	2022.07.23	3.50 ± 0.17
59801	2022.08.09	3.28 ± 0.16
59802	2022.08.10	3.16 ± 0.15
59805	2022.08.13	3.81 ± 0.19
59816	2022.08.24	3.14 ± 0.23
59832	2022.09.09	3.00 ± 0.15
59842	2022.09.19	2.24 ± 0.20
59850	2022.09.27	2.75 ± 0.13
59858	2022.10.05	3.15 ± 0.23
59860	2022.10.07	3.68 ± 0.11
59865	2022.10.12	4.65 ± 0.17
59872	2022.10.19	4.53 ± 0.22
59876	2022.10.23	3.09 ± 0.15
59879	2022.10.26	2.79 ± 0.13
59883	2022.10.30	2.37 ± 0.12
59886	2022.11.02	2.34 ± 0.09
59894	2022.11.10	2.07 ± 0.10
59895	2022.11.11	2.16 ± 0.10
59896	2022.11.12	2.39 ± 0.11
59904	2022.11.20	2.90 ± 0.14
59911	2022.11.27	2.64 ± 0.13
59913	2022.11.29	2.14 ± 0.17
59917	2022.12.03	2.05 ± 0.10
59921	2022.12.07	1.62 ± 0.07
59929	2022.12.15	1.21 ± 0.05
59942	2022.12.28	1.03 ± 0.05
59958	2023.01.13	1.00 ± 0.18
59976	2023.01.31	0.98 ± 0.04
59984	2023.02.08	1.03 ± 0.04
59987	2023.02.11	1.08 ± 0.05
59990	2023.02.14	1.31 ± 0.06
59992	2023.02.16	1.39 ± 0.07
59994	2023.02.18	1.32 ± 0.06
60003	2023.02.27	1.54 ± 0.07
60004	2023.02.28	1.49 ± 0.07
60007	2023.03.03	1.61 ± 0.16
60014	2023.03.10	1.92 ± 0.14
60021	2023.03.17	2.29 ± 0.11
60031	2023.03.27	2.42 ± 0.13
60053	2023.04.18	2.81 ± 0.13
60057	2023.04.22	2.91 ± 0.14

This paper has been typeset from a \TeX/L\TeX file prepared by the author.